Investigation of the XUV Emission from the Interaction of Intense Femtosecond Laser Pulses with Solid Targets

Rainer Hörlein

SIGILL. UNIVERSITAT. LUDOVIC. MAXIM.

München 2008

Investigation of the XUV Emission from the Interaction of Intense Femtosecond Laser Pulses with Solid Targets

Rainer Hörlein

Dissertation
an der Fakultät für Physik
der Ludwig–Maximilians–Universität
München

vorgelegt von
Rainer Hörlein
aus Seattle, USA

München, den 19. Nov. 2008

Erstgutachter: Prof. Dr. Ferenc Krausz

Zweitgutachter: Prof. Dr. Dietrich Habs

Tag der mündlichen Prüfung: 28. Jan. 2009

Abstract

The generation of coherent high-order harmonics from the interaction of ultra-intense femtosecond laser pulses with solid density plasmas holds the promise for table-top sources of intense extreme ultraviolet (XUV) and soft x-ray (SXR) radiation. Furthermore, they give rise to the prospect of combining the attosecond pulse duration of conventional gas-harmonic sources with the photon flux currently only available from large-scale free-electron laser or synchrotron facilities.

In this thesis a series of experiments studying various aspects of harmonic generation from such a plasma source are presented and the emitted XUV-radiation is characterized spectrally, spatially and temporally. The measurements probe the dynamics of the plasma surface on a sub-laser-cycle time scale and help to increase our understanding of the harmonic generation process. It is shown that, at moderate intensities and laser contrast, the emitted harmonics are indeed phase-locked but chirped and emitted as a train of XUV-bursts of attosecond duration. Measurements with very high contrast relativistically intense driving pulses reveal the generation of harmonics up to the relativistic cutoff in a diffraction-limited beam with constant divergence observed for all wavelength. This implies that the harmonics are generated on a curved surface and travel through a focus after the target possibly opening a route towards extreme intensities in the process. In addition it is found that a target roughness on the scale of the wavelength of the highest generated harmonic does not adversely affect the harmonic beam quality implying that the generation of diffraction-limited keV-harmonic beams should be possible. In a third set of experiments the first demonstration of harmonic generation from solid targets using an 8 fs driving laser opens a route towards the generation of ultra-intense single-as pulses and gives conclusive evidence for the unequal spacing of the harmonic emission.

Based on these results the development of ultra-intense sources of single as-pulses from the interaction of intense laser pulses with solid surfaces could advance at a fast pace making XUV-pump XUV-probe type investigations of nonlinear processes with attosecond time resolution feasible in the near future.

Zusammenfassung

Die Erzeugung von kohärenten hohen Harmonischen aus der Wechselwirkung von extrem intensiven und ultrakurzen Laserpulsen mit Festkörperoberflächen verspricht den Bau von kompakten Strahlungsquellen im extremen Ultraviolett (XUV) und weichen Röntgenbereich (SXR). Eine solche Quelle würde über einzigartige Eigenschaften verfügen, da sie eine Pulsdauer im Attosekundenbereich wie bei konventionellen Gasharmonischen Quellen mit den hohen Photonenflüssen, wie sie derzeit nur an Synchrotrons oder Freie Elektronen Lasern (FEL) erreicht werden, kombinieren könnte.

In dieser Arbeit wird eine Reihe von Aspekten der Harmonischenerzeugung an Oberflächen untersucht und die erzeugte XUV-Strahlung spektral, räumlich und zeitlich charakterisiert. Die Messungen geben Einblick in die Dynamik der Plasma-Oberfläche auf der Zeitskala der Oszillation des treibenden Laser Feldes und helfen so unser Verständnis des Mechanismus der Harmonischenerzeugung zu vertiefen. Experimente bei moderaten Intensitäten und Laserkontrast zeigen, dass die erzeugten Harmonischen in der Tat kohärent und daher als Zug von Attosekunden-Pulsen abgestrahlt werden. Messungen mit sehr hohem Pulskontrast und relativistischen Intensitäten zeigen die Emission von Harmonischen bis zur theoretisch vorhergesagten Maximalenergie in einem beugungsbegrenzten Strahl mit konstanter Divergenz. Dies impliziert, dass die Strahlung auf einer gekrümmten Oberfläche erzeugt wird und anschließend durch einen Fokus propagiert in dem, im Prinzip, Intensitäten Größenordnungen höher als jene im Laserfokus erzeugt werden könnten. Außerdem zeigen die Messungen, dass eine Oberflächenrauhigkeit im Bereich der Wellenlänge der erzeugten Harmonischen deren Strahlprofil nicht beeinflusst. Somit sollte die Erzeugung beugungsbegrenzter Strahlung mit Energien im keV-Bereich möglich sein. In einem dritten Experiment wird die Erzeugung von Harmonischen von Oberflächen mit einem 8 fs Laser demonstriert. Die Messung stellt einen entscheidenden Schritt auf dem Weg zur Erzeugung von ultraintensiven einzelnen Attosekunden-Pulsen dar.

Auf der Grundlage dieser Ergebnisse sollte die Entwicklung von ultraintensiven Quellen für die Erzeugung von einzelnen Attosekunden-Pulsen von Oberflächen schnell voranschreiten und in naher Zukunft erste XUV-Anregungs XUV-Abfrage Experimente von nichtlinearen Prozessen auf der Attosekunden Zeitskala ermöglichen.

Contents

Chapter 1

Introduction

The desire to visualize and understand the most fundamental processes in nature has always been the driving force behind basic research. It has lead to the development of a wealth of new methods advancing high precision measurements in many fields of physics. Sparked by the invention of the laser [1] and the rapid technological advance over the past four decades experiments probing fundamental processes in matter with ever higher temporal resolution have become possible. This development has culminated in the production of laser pulses approaching the duration of a single optical cycle of few femtoseconds (1 fs=10^{-15} s) duration [2–4] which can be used to resolve, for example, the formation and rupture of chemical bonds in real time [5]. However, these chemical reactions are still not the fastest processes in atoms and molecules. The dynamics of electron wave packets evolve on an attosecond (1 as=10^{-18} s) time-scale and are therefore faster than a single oscillation of the electric field of conventional laser systems (τ_L=2.67 fs). To overcome the resolution barrier imposed by the duration of a single laser cycle and enter the regime of *Attoscience* in which electron dynamics in atoms and molecules can be observed in real time coherent broad-band radiation sources in the extreme-ultraviolet (XUV) or soft x-ray (SXR) wavelength range are necessary. Only radiation from such sources can be used to synthesize pulses short enough to achieve as-resolution. The prospect of generating such pulses has motivated the investigation of harmonic generation from solid density plasmas (SHHG) presented in this thesis.

Up to now the only sources of attosecond pulses capable of probing inner atomic dynamics are based on the nonlinear interaction of moderately intense laser pulses with noble gases [6–8]. In this scheme an electron is removed from the atom by the strong field of the laser, accelerated in the vacuum and then re-collides with the atomic core emitting a high energy photon [9]. Using this technique coherent radiation at high harmonics of the driving laser frequency is generated. From these spectra isolated as-pulses with durations as short as 80 attoseconds have been synthesized [10–12] and also applied to probe, for example, the ionization dynamics of noble gases in strong fields [13] or the emission of electrons from solid surfaces [14] in real time. While this method is very successful and has lead to a whole series of ground-breaking discoveries it suffers from one fundamental limit: Owing to the fact that excessive ionization of the gas target has to be prevented in this generation process the driving laser intensity that can be used for harmonic generation is limited. Despite several attempts to improve the conversion efficiency [15–18] this imposes severe limitations on the maximum energy of the generated as-pulses rendering XUV-pump, XUV-probe type experiments studying nonlinear processes, [19–24] experiments addressing single molecule imaging [25] or the real-time observation of laser-plasma dynamics [26–28] impossible with such an XUV source [29].

To overcome this limitation a completely different mechanism for the generation of coherent high harmonic radiation is necessary which does not suffer from this limitation. The generation of high harmonics from the interaction of a relativistically intense laser pulse with a solid-density target has been identified as a promising candidate to achieve this goal. The main advantage of this laser-plasma based approach lies in the fact that it relies on the reflection of the incident laser field off the electron surface of the strongly ionized target and thus does not suffer from the limitation imposed on gas harmonics. On the contrary: The harmonic generation efficiency and the width of the generated harmonic spectrum increases strongly with increasing laser intensity making this process highly scalable [30] and offering the potential of combining the high photon fluxes currently only available at large-scale facilities like free-electron lasers [31] with the attosecond time resolution of laser-based sources. In fact, beyond the generation of intense as-pulses for the study of atoms and molecules the predicted scalability of the generation process may even offer the possibility of reaching intensities much higher than those of the driving laser [32] and exceeding the Schwinger-Limit [33] at which the production of electron-positron pairs from vacuum is predicted.

Recent theoretical studies have clarified that two distinct mechanisms are responsible for the generation of high harmonics from solid targets. At sub-relativistic intensity Coherent Wake Emission (CWE) [34, 35] dominates while in the limit of relativistic intensities the harmonics are generated off a Relativistic Oscillating Mirror (ROM) [30, 36, 37]. The CWE process exhibits a target density dependent spectral cutoff as observed in the first solid harmonic experiments while in ROM the cutoff is target independent and scales with the laser intensity. It is important to note that, while many recent experiments have been conducted with CWE harmonics as they are easier to generate, a competitive as-pulse source will be based on ROM as much shorter pulses with superior phase-properties are achievable with this method [30, 38]. A sketch of such a possible single as-pulse source is shown in figure 1.1. Note that aside from the target and the

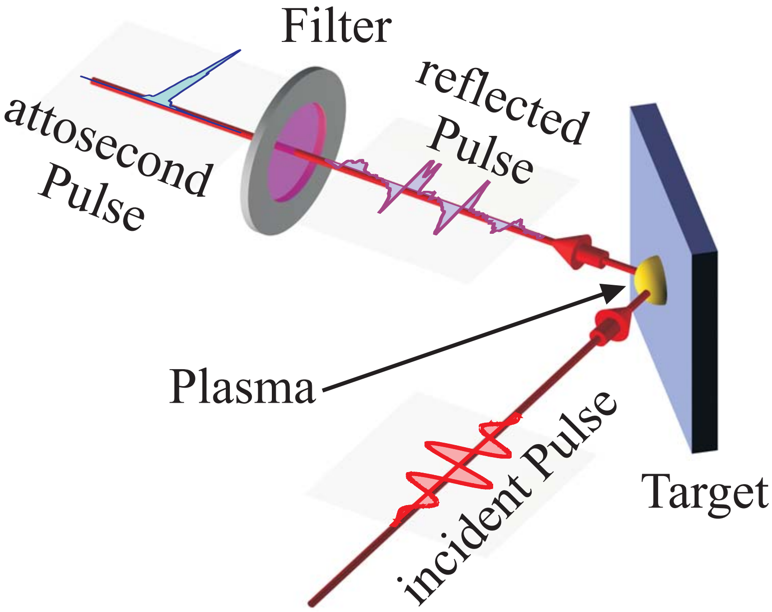

Figure 1.1: Generation of a single as-pulse using a few-cycle driving laser and a suitable filter. The incident laser pulse rapidly ionizes the target and generates high harmonics of its fundamental frequency. The selection of a suitable part of the harmonic spectrum with a filter will lead to the generation of an attosecond pulse. (Figure from [36])

driving laser pulse the only necessary component is a suitable filter to select the desired spectral range from the emitted spectrum.

While the recognition of surface harmonics as a possible source of as-pulses is rather new the first experimental observation of harmonic generation from solid-density targets dates back to the late 1970s. Interestingly enough this was more than ten years prior to the work by T. Hänsch et al. [39] pointing out the possibility of synthesizing as-pulses from a train of harmonics and the proposal to use harmonics generated from noble gases for this purpose by Gy. Farkas and Cs. Toth [40]. At that time experiments conducted with high energy nanosecond CO_2 lasers revealed spectra extending up to the 46^{th} harmonic order of the fundamental 10.6 μm wavelength driver [41–44]. In contrast to the newer fs-sources however the harmonics in those experiments where emitted isotropically and no beaming was observed.

After this work it took roughly 10 years until the topic was revisited and theoretical studies predicted harmonic generation from the interaction of relativistic laser pulses with solid targets [45–48] for the first time. On the experimental side the first observations of harmonics using a femtosecond Titanium:Sapphire (Ti:Sa) laser were reported almost simultaneously by S. Kohlweyer et. al. [49] and D. von der Linde et. al. [50] followed by a whole series of other publications using similar laser systems [51–55]. Note that, despite the fact that this is not stated explicitly, all harmonics observed in these experiments where most likely the result of CWE and not ROM. The emission of ROM harmonics was observed unambiguously for the first time at the Vulcan laser facility in the UK by P. Norreys et al. [56]. Only recently newer experiments have demonstrated that the harmonic emission from a solid target is beamed in the direction of the specular reflection under high-contrast conditions [52, 57, 58], have shown the transition from CWE to ROM harmonics [57, 59], addressed the issue of harmonic coherence [60] and have confirmed the theoretically predicted harmonic power-law scaling [61] and spectral cutoff [58] in the ultra-relativistic regime [30].

The work presented in this thesis aims at advancing the understanding of surface harmonic generation and is driven by the vision of an ultra-intense single as-pulse source suitable for the experimental study of processes on the attosecond time-scale. It consists of a set of experiments conducted with different laser sources addressing various aspects of the interaction of intense femtosecond laser pulses with solid density targets. This thesis describes a compilation of experimental results obtained using three different driving lasers and aiming at the characterization of various aspects of the harmonic generation mechanism all of which are of great relevance for the envisioned as-pulse source depicted in figure 1.1. The measurements include (a) a campaign investigating the possibility of generating harmonics with a few-cycle driver laser, (b) a series of measurements addressing the temporal characteristics of the emitted harmonic radiation and (c) an experiment aiming at the generation of high-quality harmonic beams of relativistic harmonics using a high contrast driver source.

The experiments demonstrate that (a) surface harmonics can be generated using few-cycle driver pulses [62] opening the route toward the efficient generation of single as-pulses, (b) they prove that the harmonics produced on a solid target are indeed phase-locked and thus emitted as a train of as-pulses as predicted by theory [63] and (c) they verify that, provided the contrast of the driving laser is good enough, the harmonics are emitted in a near diffraction-limited cone off a curved (dented) target surface [64]. Note that this also implies that the harmonics travel through a focus in front of the target which may allow the generation of extreme intensities [32] when proper pre-shaping of the target is implemented [65, 66]. Furthermore the experiments also allow conclusions about the sub-cycle dynamics of the electrons in the harmonic generation process and thus the chirp of the emitted harmonics [62, 67] and they point out a route towards scaling plasma mirrors to the relativistic regime and the application of such mirrors as spatial filters and efficient frequency doublers for future laser systems [68].

Having addressed several key issues of harmonic generation from overdense plasmas and answered a series of fundamental questions in this thesis the challenge for the future will now be to combine the different beam properties and methods demonstrated separately in one experiment in order to generate a single ultra-intense burst of well beamed relativistic harmonics. This will open the way for a whole series of experiments not feasible with current as-sources owing to their limited pulse energy and greatly advance the field of *Attoscience*.

1.1 Outline of this Thesis

At this point a brief overview of this thesis shall be given. As has been mentioned before the work presented here focuses on the characterization of high harmonics generated in the interaction of ultra-intense laser pulses with solid targets. Most of the work presented in this thesis was conducted in close collaboration with my colleague Yutaka Nomura. However, his PhD thesis [69] focuses on the XUV-autocorrelation and thus temporal characterization of a train of harmonics produced with the ATLAS system while my work consists of a series of experiments in which harmonics generated using different laser sources are studied and the properties of the emitted coherent XUV-beams are investigated. The two PhD theses are complementary to each other with a common objective: The assessment of the appropriateness of the process for the generation of intense as-pulses.

- Before the experimental results are presented *Chapter 2* introduces the most important properties of intense laser pulses and discusses their interaction with solid-density targets. Special emphasis is given to the introduction of the two dominant mechanisms that have been identified to contribute to the generation of high harmonics from solid density targets, the Relativistic Oscillating Mirror (ROM) and Coherent Wake Emission (CWE).

- *Chapter 3* gives an overview of the two laser systems at the MPQ that have been used for the experiments described in chapters 4 and 6 of this thesis. The setup and basic concept of the Titanium:Sapphire ATLAS laser and the OPCPA-based LWS10 system are described and the most important laser parameters like pulse duration, pulse energy, the focusability of the beam and the laser contrast are characterized under the conditions under which the experiments where conducted.

- In *Chapter 4* two methods for the temporal characterization of surface harmonics are presented: The XUV-autocorrelation and a temporal coherence measurement. While the autocorrelation proves that the emitted harmonics are indeed phase-locked as predicted by theory the coherence measurement in combination with the

AC-results allows the extraction of information about the sub-cycle dynamics of the electrons involved in the harmonic generation process. A comparison of the results of these measurements also allows interesting conclusions about the dynamics of the harmonic generation mechanism itself. Two publications have also resulted directly from the work presented in this chapter [63, 67].

- The results presented in *Chapter 5* where obtained at the Rutherford Appleton Laboratory. In these experiments very high contrast laser pulses where generated using a plasma mirror. Under these conditions ROM harmonics up to the theoretically predicted relativistic cutoff where observed. Furthermore the divergence of the emitted harmonics and the influence of target roughness was investigated. In addition the fundamental and second harmonic emanating from the target were characterized showing that the high intensity interaction of a laser pulse on a solid target may be a route to spatial filtering and second harmonic generation in future high-power lasers. The results are also presented in two publications [64, 68].

- The last experimental chapter, *Chapter 6*, presents results obtained with the 8 fs LWS10 system demonstrating, for the first time, harmonic generation with a few-cycle driver pulse. The experiments are an important step towards the generation of single as-pulses for applications, but beyond this they also allow unique insight into the dynamics of the harmonic generation process itself. The findings from this chapter are also summarized in [62].

- *Chapter 7* summarizes the results presented in the previous chapters and gives an outlook to the future. Especially the prospect of the generation of single ultra-intense attosecond pulses for applications is discussed. Two papers written in the course of my PhD-work also address the improvement of current-day harmonic sources for future applications in attosecond and high-field physics [66, 70].

Chapter 2

Generation of High Harmonics from Solid Surfaces

To facilitate the discussion of the experimental results presented in this thesis this chapter will introduce some theoretical background on the interaction of intense laser pulses with solids and discuss the mechanisms leading to the generation of high harmonics from solid density plasmas. While the first section is intended to give a general overview over the most important properties of intense laser pulses and their interaction with solid-density targets the second section focuses in more detail on two distinct mechanisms leading to harmonic generation: the Relativistic Oscillating Mirror (ROM) [30, 36, 37] and Coherent Wake Emission (CWE) [34, 35, 60].

2.1 Relativistic Laser Solid Interactions

The aim of this section is to introduce important quantities and processes relevant for the interaction of intense laser pulses with solid density targets, that will be used and referred to often in this thesis. By no means this discussion is meant to be complete instead the focus is laid only on the most important points. More detailed discussions can be found in many plasma physics and electrodynamics textbooks (for example [71–73]).

All equations in this chapter are, in contrast to most textbooks, given in SI-units since this thesis focuses on experimental results which are naturally given in these units.

2.1.1 Relativistic Laser Pulses

Electromagnetic phenomena both in vacuum and in media are described by Maxwells equations. The electric and magnetic fields ($\vec{E}$ and $\vec{B}$) of electromagnetic waves can thus be derived directly from them. They can be written using a vector potential $\vec{A}$ and a scalar potential Φ:

$$\vec{B} = \nabla \times \vec{A} \tag{2.1}$$

$$\vec{E} = -\frac{\partial}{\partial t}\vec{A} - \nabla\Phi. \tag{2.2}$$

Using equations 2.1 and 2.2 the wave equation for the vector potential can be derived [72]. Using the Lorenz Gauge

$$\nabla\vec{A} + \frac{1}{c^2}\frac{\partial}{\partial t}\phi = 0, \tag{2.3}$$

the vector potential $\vec{A}$ is given by

$$-\nabla^2\vec{A} + \frac{1}{c^2}\frac{\partial^2}{\partial t^2}\vec{A} = \frac{1}{c^2\epsilon_0}\vec{j}, \tag{2.4}$$

where c is the speed of light in vacuum, ϵ_0 is the electric constant and $\vec{j}$ is a current density. Assuming the propagation in vacuum with no free charges, electrostatic fields or currents i.e. $\vec{j} = 0$, equation 2.4 has the solution

$$\vec{A} = \hat{y}A_0\cos(\omega t - kx + \phi). \tag{2.5}$$

This is a linearly polarized plane wave with frequency ω and wave number k propagating in the $\hat{x}$ direction with phase ϕ. Note that the polarization has been arbitrarily chosen to be linear and in the $\hat{y}$ direction. Any other infinite plane wave with elliptical polarization would also be a solution to equation 2.4.

For this solution for $\vec{A}$ the Lorenz Gauge and the initial conditions immediately also give the scalar potential Φ to be $\Phi = 0$. Using these results it is now possible to calculate $\vec{E}$ and $\vec{B}$ from equations 2.1 and 2.2 respectively yielding

$$\vec{B} = \hat{z}B_0\sin(\omega t - kx + \phi), \tag{2.6}$$

$$\vec{E} = \hat{y}E_0\sin(\omega t - kx + \phi). \tag{2.7}$$

This is the infinite plane electromagnetic wave. The relation between the amplitudes E_0, B_0 and A_0 can also be obtained from equations 2.1 and 2.2. It is:

$$A_0\omega = E_0 = cB_0. \tag{2.8}$$

While these considerations are of general nature and valid for all wavelength the discussion will be restricted to the optical and near infrared (0.5 to 1 μm) range in the following discussions, this being the typical wavelengths of the laser systems used for the experiments described in this thesis.

In high intensity laser physics the amplitude of the laser pulses is normally not given in terms of the peak electric or magnetic field but in the form of a normalized vector potential a_0. This dimensionless quantity is calculated from the vector potential A_0 using the following equation:

$$a_0 = \frac{eA_0}{m_\mathrm{e}c} = \frac{eE_0}{m_\mathrm{e}c\omega} \tag{2.9}$$

Here e and m_e are the charge and mass of an electron, c is the speed of light and equation 2.8 was used to express A_0 in terms of E_0.

In experimental physics it is more common to express a_0 in terms of the laser wavelength and its focused intensity. The intensity can be calculated from the electric field using the relation $I_\mathrm{L} = c\epsilon_0 E_0^2/2$ which is derived, for example, in [72, 74]. Including the values of all the physical constants in equation 2.9 we get the formula

$$a_0^2 = I_\mathrm{L}[Wcm^{-2}]\ \lambda^2[\mu m^2]/1.37\ 10^{18}, \tag{2.10}$$

into which the intensity and the wavelength have to be entered in units of $[W\ cm^{-2}]$ and $[\mu m]$ respectively. Depending on the value of a_0 laser pulses are called sub-relativistic ($a_0 \ll 1$), relativistic ($a_0 \approx 1$) or ultra-relativistic ($a_0 \gg 1$). In the experiments presented in the later chapters of this thesis average intensities as high as $a_0 = 3$, i.e. well in the relativistic regime, were achieved.

To understand the difference between non-relativistic and relativistic intensities intuitively it is very instructive to consider the influence of such fields on a single electron. The relativistic equation of motion of a single electron in an electromagnetic field is given by

$$\frac{\partial \vec{p}}{\partial t} = \frac{\partial}{\partial t}(\gamma m_\mathrm{e}\vec{v}) = -e(\vec{E} + \vec{v} \times \vec{B}), \tag{2.11}$$

where $\vec{p}$ is the relativistic momentum of the electron, $\vec{v}$ is the velocity of the electron and $\gamma = \sqrt{1 - v^2/c^2}^{\,-1}$ is the relativistic gamma factor. Two forces are found to govern the motion of the electron in the electromagnetic wave, one pointing in the direction of the electric field and a second one in the $\vec{v} \times \vec{B}$, corresponding to the laser propagation direction. If we now consider the relative amplitudes of the two forces (using equation 2.8) we see that the $\vec{v} \times \vec{B}$ force is a factor v/c smaller than the force resulting from the electric field. The peak electron velocity as a result of the oscillation in the electric field can easily be calculated (neglecting the $\vec{v} \times \vec{B}$ term) by substituting equation 2.7 into equation 2.11 and expressed in terms of the normalized vector potential via equation 2.9. It is

$$v_\mathrm{max} = \frac{eE_0}{\gamma m_\mathrm{e}\omega} = \frac{a_0}{\gamma}c. \tag{2.12}$$

From this equation it becomes obvious why pulses with $a_0 \ll 1$ are called non-relativistic while those with $a_0 \gg 1$ are called ultra-relativistic. For $a_0 \ll 1$ the maximum electron velocity is much smaller than c and thus the electron only oscillates in the plane of the electric field. At $a_0 = 1$ the oscillation velocity becomes relativistic (close to c) and for $a_0 \gg 1$ the velocity is very close to c. In these cases the $\vec{v} \times \vec{B}$ component becomes comparable to the $\vec{E}$ component in the force on the electron and the electron is accelerated in the direction of the laser field.

2.1.2 Properties of Laser generated Solid Density Plasmas

In the types of experiments conducted for this thesis the laser pulse does not interact with a single electron as discussed in the previous section but rather with a solid density target. The laser rapidly ionizes the atoms at the surface and then interacts with the high density plasma. The ionization process and the subsequent interaction of the laser with the dense plasma will be discussed in the following paragraphs.

Even though the energy of a single near infrared (NIR) photon is only $\approx 1.3\ eV$, i.e. much lower than the binding energy of electrons in atoms, high intensity lasers can very efficiently ionize gases and solids. Two mechanisms have been identified to give rise to ionization in strong fields. At moderate intensities multi-photon ionization is the dominant process. One electron in an atom absorbs multiple laser photons and thus gains the necessary energy to be freed from the atom. For very high intensities the electric field can modify the binding potential of an atom so strongly that the electrons can tunnel through the remaining potential barrier or is even freed by suppression of the barrier below the binding potential. These processes are known as tunnel- and barrier-suppression ionization. A useful parameter for determining in which ionization regime a laser is is the Keldysh parameter [71, 75]. It relates the laser intensity to the binding energy of the electrons in an atom and is defined as

$$\gamma_{\mathrm{K}} = \frac{4\pi}{\lambda_{\mathrm{L}}} \sqrt{\frac{\epsilon_0 m_{\mathrm{e}} c^3}{e^2} \frac{E_{\mathrm{Ion}}}{I_{\mathrm{L}}}}, \tag{2.13}$$

where E_{Ion} is the binding energy of an electron in an atom. For $\gamma_K > 1$ multi-photon ionization is dominant while for $\gamma_{\mathrm{K}} < 1$ the laser is in the tunnel ionization regime. In all experiments presented in the later chapters the Keldysh parameter was well below one. For this reason the discussion of the ionization mechanisms will be restricted to tunnel and barrier suppression ionization.

Figure 2.1 illustrates the influence of a strong electric field on the binding potential of an atom. The strong external field distorts the Coulomb potential (figure 2.1 (a)) so strongly that the binding potential for large x is lower than the binding energy of the

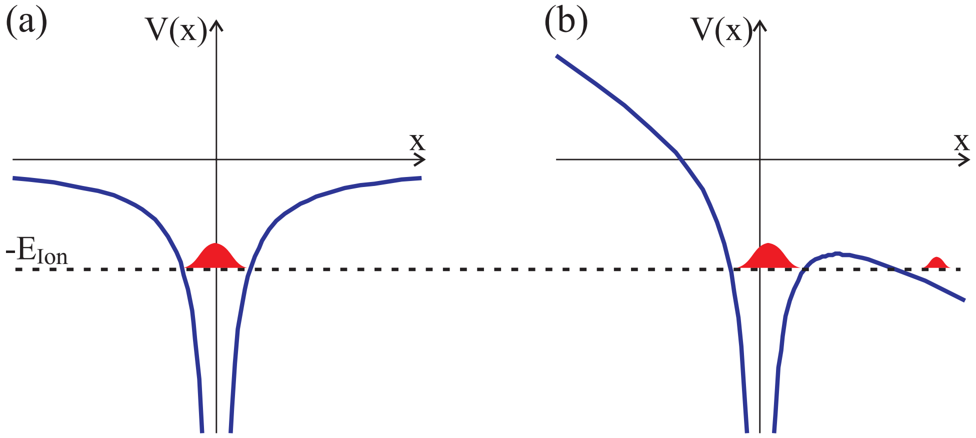

Figure 2.1: Figure (a) shows an undistorted Coulomb potential with a bound electron wave packet. In (b) the binding potential is distorted by a strong electric field. The Coulomb barrier is suppressed and the electron can tunnel out of the potential with a finite probability.

electron. The electron can then quantum-mechanically tunnel through this barrier. This has been studied in detail theoretically by Keldysh [75] and has recently been observed in real time in an experiment [13].

For still higher intensities the binding potential can even be distorted so strongly that the barrier actually drops below the binding energy of the electron, thus freeing it completely. This is known as barrier suppression ionization (BSI). In fact, for typical laser intensities on the order of $10^{19}\ W\ cm^{-2}$ this is the dominant ionization mechanisms. In reference [71] the necessary intensity for BS ionization of, for example, O^{6+} is given as $4 \times 10^{16}\ W\ cm^{-2}$. This means that even the leading edge of our laser pulses with peak intensities as high as $10^{19}\ W\ cm^{-2}$ can strongly ionize our targets.

In the case of the solid targets the real ionization dynamics are naturally more complicated since free ions and electrons will influence the barrier suppression. Furthermore, once enough electrons are freed, other ionization mechanisms like collisional ionization become important [71, 76]. Nonetheless the simple barrier suppression model gives valuable insight into the ionization dynamics in solids.

Once the laser pulse has ionized the target with its leading edge it does not propagate in vacuum or an insulator anymore but in a plasma. To find out how this influences the propagation of the electromagnetic wave it is instructive to revisit equation 2.4. Unlike in the case discussed in the previous section, the propagation in vacuum, the current density $\vec{j}$ is nonzero in a plasma. $\vec{j}$ can be calculated from the velocity of the free electrons in the plasma using

$$\vec{j} = en_{\mathrm{e}}\vec{v}. \tag{2.14}$$

To calculate the electron velocity we consider their equation of motion. Two forces govern the motion of the electrons: the electric field of the driving laser and collisions or drag inside the plasma (in this case we have neglected forces originating from the magnetic field). Note that even though the electrons are mobile the plasma stays quasi-neutral, i.e. there is no charge separation and thus no restoring force of the ions acting on the electrons. The equation of motion thus is

$$m_\mathrm{e}\frac{\partial\vec{v}}{\partial t} = -e\vec{E} - \nu m_\mathrm{e}\vec{v}, \tag{2.15}$$

where ν is a measure of the damping of the electron motion, the collision frequency. Using equation 2.7 we can solve equation 2.15 and calculate $\vec{v}$:

$$\vec{v} = \frac{e}{m(\imath\omega + \nu)}\vec{E}. \tag{2.16}$$

Considering that $\vec{E} = \imath\omega\vec{A}$ (which can be calculated from equations 2.2 and 2.5) and inserting equation 2.16 into equation 2.14 we can now rewrite the equation for the vector potential 2.4 in the following way:

$$(-c^2k^2 + \omega^2)\vec{A} = \frac{n_\mathrm{e}e^2}{\epsilon_0 m_\mathrm{e}(1 + \imath\nu/\omega)}\vec{A}. \tag{2.17}$$

The right hand side of this equation can be simplified by introducing the plasma frequency ω_p which is a function of the electron density of the plasma.

$$\omega_\mathrm{p} = \sqrt{\frac{n_\mathrm{e}e^2}{\epsilon_0 m_\mathrm{e}}} \tag{2.18}$$

In an intuitive way ω_p can be understood as the resonance frequency of a group of electrons with density n_e oscillating around fixed ions with the same charge density.

From equation 2.17 one can obtain the dispersion relation for an electromagnetic wave in a plasma. In the case of a colisionless plasma, i.e. for $\nu = 0$ it is:

$$\omega^2 = \omega_\mathrm{p}^2 + k^2c^2. \tag{2.19}$$

Using this we can calculate the index of refraction of a plasma $n(\omega)$ and derive its frequency dependence.

$$n(\omega) = \frac{ck}{\omega} = \sqrt{1 - \frac{\omega_\mathrm{p}^2}{\omega^2}} \tag{2.20}$$

Several interesting properties of a plasma can be obtained from equation 2.20. As long as the laser frequency ω is larger than the plasma frequency the index of refraction is real and smaller than one. The plasma is transparent. For $\omega < \omega_\mathrm{p}$ the the index of refraction becomes imaginary. The plasma is not transparent anymore but reflects the incident electromagnetic wave. To find the electron densities at which this transition between transmission and reflection occurs one can define the critical electron density $n_\mathrm{e,crit}$ at which $\omega_\mathrm{p} = \omega$. Using equations 2.20 and 2.18 the critical density is given to be

$$n_\mathrm{e,crit} = \frac{\epsilon_0 m_\mathrm{e} \omega^2}{e^2}. \tag{2.21}$$

Considering the central wavelength of $\approx 800\ nm$ of a Titanium:Sapphire laser equation 2.21 gives a critical density of $n_\mathrm{e,crit} = 1.75 \times 10^{21}\ cm^{-3}$. This value is approximately 200 to 400 times lower than the solid density of the typical targets used for the experiments described in this thesis, thus we expect that our solid density plasmas reflect a sizable amount of the incident laser radiation. In fact this reflection off the critical density surface is in essence one of the origins for high harmonic radiation from solid targets that will be discussed in the next section of this chapter and is the key working principle of a plasma mirror [77–79]. The plasma mirror is discussed in more detail in Appendix A of this thesis.

Finally it is important to point out that even a plasma with a density many times higher than the critical density does not fully reflect the incident electromagnetic wave. As soon as the target is ionized the plasma begins to expand into the vacuum and the main part of the incident laser thus interacts with a density gradient instead of a step-like profile. Amongst other effects this interaction can give rise to absorption of considerable amounts of the laser energy. Two mechanisms shall be named explicitly here since they are relevant for the generation of high harmonics. Both of these mechanisms rely on a p-polarized laser pulse incident onto the target under an angle such that one part of the electric field of the pulse is perpendicular to the target surface. One is called resonance absorption and describes the excitation of plasma waves at the critical density surface (and possibly densities corresponding to harmonics of the fundamental laser frequency) [80]. The second is Brunel heating which describes the acceleration of hot electrons in the electric field perpendicular to the target surface which are hurled back into the target in the next half-cycle when the field reverses and excite plasma waves in their wake [81]. Especially the second process is of great importance for harmonic generation as will be discussed in section 2.2.2 of this thesis.

2.2 Harmonic Generation from Solid Surfaces

Building on the discussion of high intensity laser pulses and their interaction with solid density plasmas in the previous sections it is now possible to consider the generation of high harmonics from solid density plasma surfaces in more detail.

Two distinct mechanisms have been identified to give rise to harmonic radiation in the interaction of high intensity laser pulses with solid targets: The Relativistic Oscillating Mirror (ROM) and Coherent Wake Emission (CWE). While ROM is based on the reflection of the incident laser pulse from the critical density surface of the target oscillating at velocities close to the speed of light, CWE harmonics originate from plasma waves excited in the plasma density gradient by Brunel electrons and their subsequent mode conversion to electromagnetic waves. As one may already guess from the different generation mechanisms the harmonics generated via the two processes have very different properties which shall be discussed in the following sections. Most notably the laser intensity range in which they are generated is different. While CWE dominates for sub-relativistic intensities with $a_0 < 1$ (see equation 2.10) ROM is only efficient for relativistic laser pulses and completely takes over for $a_0 \gg 1$.

2.2.1 Harmonics in the Relativistic Regime

Let us now look at the generation of harmonics in the relativistic regime in more detail. As has been stated above the harmonic generation in this case is the result of a Doppler upshift of the fundamental laser frequency when the incident wave is reflected coherently off the critical density surface oscillating in the relativistic laser field itself. For a mirror moving with a constant velocity close to the speed of light this problem has already been discussed by Einstein as early as 1905 [82]. In the case of the oscillating mirror the problem becomes a little more complicated since the velocity of the mirror is now a periodic function of time which is not known a priori.

The generation of harmonics in the relativistic regime has been studied theoretically using analytical models as well as Particle In Cell (PIC) simulation by a number of groups around the world in the past 15 years [30, 32, 36–38, 45–48, 65, 83–88]. The work of T. Baeva, S. Gordienko and S. Pukhov [30, 32, 37, 83, 84] and especially the theory of relativistic spikes [30] shall be named explicitly in this context because it has led to a number of important insights in the recent past.

The simpler oscillating mirror model introduced by Bulanov et al. [45] and discussed in detail by G. Tsakiris et al. [36] shall be introduced in the following paragraphs since, despite its simplicity, it is capable of nicely describing many key features of harmonics generated from oscillating surfaces. The principle of the model is depicted schematically in figure 2.2.

The electric field passing the position of the observer at time t hits the oscillating

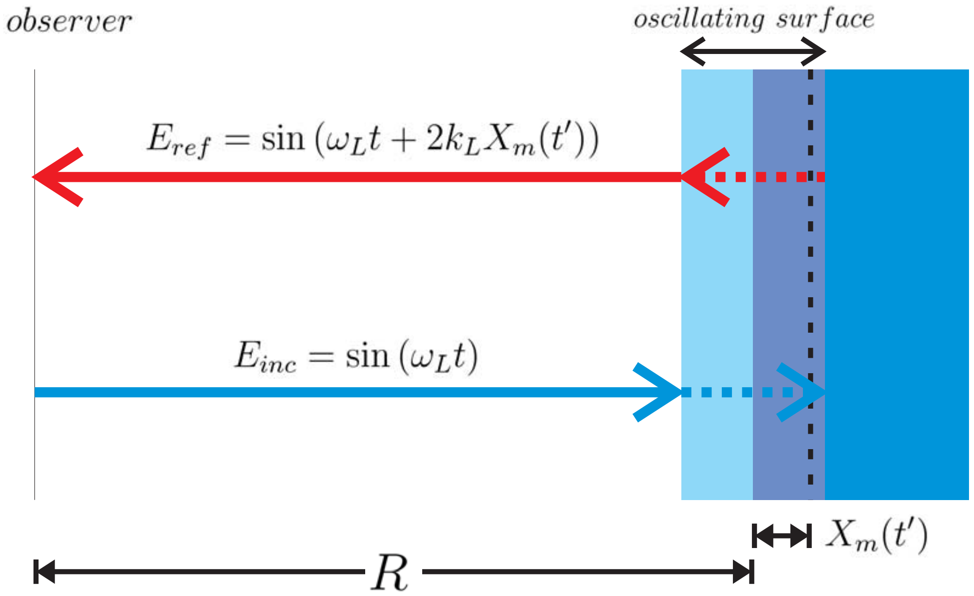

Figure 2.2: Schematic drawing showing the basic idea of the oscillating mirror model. From the point of view of an external observer the incident laser field is reflected off the electron surface oscillating around an immobile ion background. The reflected wave picks up phase distortions depending on the exact mirror position at the time of reflection. The observer sees a distorted waveform rich in harmonic content.

mirror at a later time t' given by

$$t' = t + \frac{R + X_\mathrm{m}(t')}{c}. \tag{2.22}$$

In this equation R is the constant distance from the observer to the immobile ion surface and $X_\mathrm{m}(t')$ is the time dependent position of the oscillating electron density surface (see figure 2.2). Since this function is generally not known and very difficult to calculate exactly because of the delicate interplay of forces of the incident laser field and the restoring force of the immobile ions we have to make an assumption at this point. For the sake of simplicity we will consider normal incidence of the laser onto the target and neglect the restoring force of the background ions. The only force acting on the electrons is thus the ponderomotive $\vec{v} \times \vec{B}$ force from equation 2.11 which is proportional to $\sin(2\omega_\mathrm{L} t)$. $X_\mathrm{m}(t')$ thus becomes

$$X_\mathrm{m}(t') = A_\mathrm{m}(t) \sin(2\omega_\mathrm{L} t' + \phi_\mathrm{m}), \tag{2.23}$$

where ϕ_m is a phase shift between the driving force and the response of the electron surface and $A_\mathrm{m}(t)$ is the time dependent amplitude of the surface oscillation. The amplitude of the oscillation can be calculated from the normalized vector potential of the driving laser following the derivation in [36] and taking into account that the relation between the maximum gamma-factor of the surface $\gamma_{\max}$ and a_0 is given by $\gamma_{\max} = \sqrt{1+a_0^2}$ [89]. Thus the amplitude of the oscillation is

$$A_{\mathrm{m}}(t) = \frac{\lambda_{\mathrm{L}}}{4\pi}\frac{a_0(t)}{\sqrt{1+a_0(t)^2}}. \tag{2.24}$$

This choice of surface motion may seem somewhat arbitrary and one may ask whether we can expect useful results from this approximation but fortunately it has been shown by Baeva et al. [30] that the most important features of the harmonic spectrum, i.e. its power dependence and the cutoff, are actually independent of the exact surface motion. We can thus expect even our simple approximation to reproduce the key features of the harmonic spectrum correctly.

By inserting equations 2.23 and 2.24 into equation 2.22 and setting $R = 0$ (which we can do since R is independent of time and only introduces a constant and thus irrelevant phase shift) we obtain a transcendental function for t' as a function of t which can be evaluated numerically. From this we can calculate the motion of the mirror as seen by the observer (This is equivalent to the relativistic Doppler shift for non-uniform motion).

Using $X_{\mathrm{m}}(t)$ we can also calculate the distorted electric field in the reference frame of the observer. For an incident sine wave and in the limit of a slowly varying envelope function, i. e. when the envelope $E_0(t) \approx E_0(t')$,

$$E_{\mathrm{inc}} = E_0(t)\sin(\omega_{\mathrm{L}}t), \tag{2.25}$$

it becomes

$$E_{\mathrm{ref}} = E_0(t)\sin(\omega_{\mathrm{L}}t + 2k_{\mathrm{L}}X_{\mathrm{m}}(t')). \tag{2.26}$$

This is the incident sine wave with a phase shift proportional to twice the distance $X_{\mathrm{m}}(t')$. E_{ref} will now contain all the harmonics generated in the reflection from the oscillating surface.

Figure 2.3 shows the results of the calculations sketched above. It can be seen immediately from panel (a) that, from the point of view of the observer (red curve), the surface executes an anharmonic periodic oscillation. The forward motion of the mirror only consumes a small fraction of the oscillation cycle indicating that it moves toward the observer with very high velocity while the backwards motion is much slower. This becomes even clearer when taking the derivative of the surface motion, i.e. when calculating the velocity of the surface as a function of time. This is depicted in figure 2.3 (b). The forward velocity of the mirror is sharply peaked in time. In fact the spikes can be seen to get shorter and higher as the laser intensity increases. These velocity spikes are responsible for the generation of high harmonics because they lead to a strong Doppler

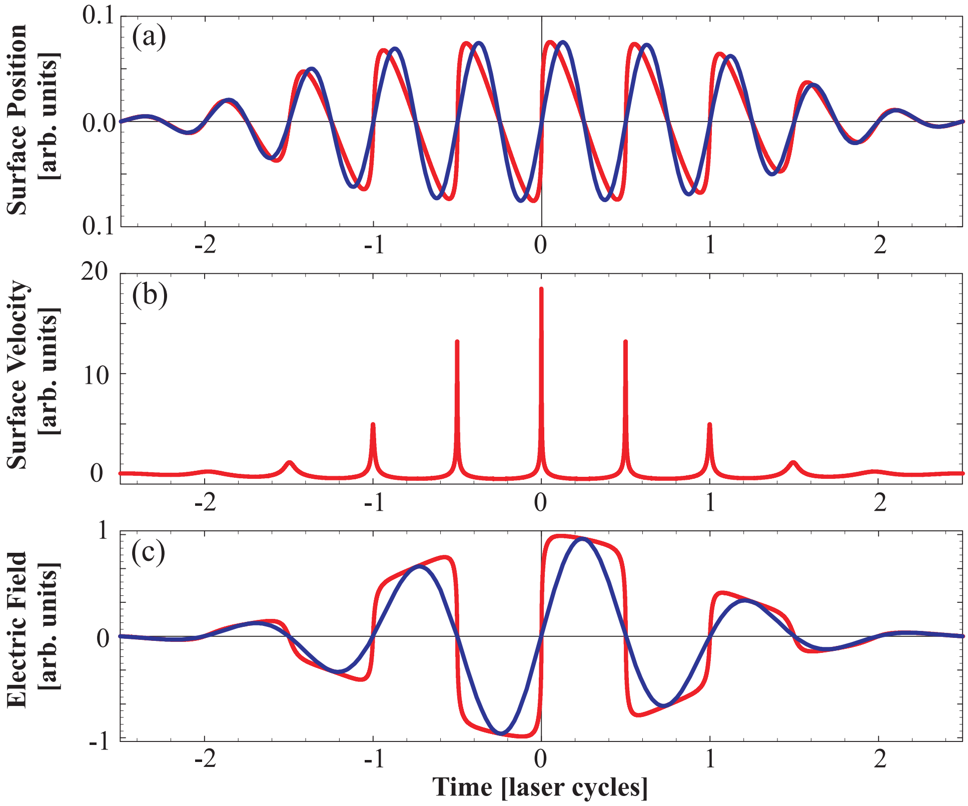

Figure 2.3: Results of a mirror model calculation assuming a two-cycle laser pulse with a peak intensity of $a_0 = 3$ and the surface motion given in equation 2.23 with $\phi_{\mathrm{m}} = 0$. Panel (a) shows the position of the mirror surface X_{m} as a function of time in the observers frame of reference (red) and in the reference frame of the mirror (blue). The mirror clearly executes an anharmonic motion in the observers frame of reference. This finding is supported by panel (b) showing the velocity of the mirror surface as a function of time. Sharp velocity spikes can be observed when the mirror moves toward the observer. In (c) the incident (blue) and reflected (red) electric field (equations 2.25 and 2.26) are shown. The almost step-like shape of the reflected field suggests rich harmonic content.

up-shift of the frequency of the incident radiation. They also essentially correspond to the *relativistic spikes* discussed in the more sophisticated analytical theory developed by T. Baeva et al. [30].

To analyze the harmonic content of the reflected pulse it is most convenient to calculate the reflected electric field in an observers frame of reference. The incident (blue) and reflected (red) fields are depicted in figure 2.3 (c). While the incident field is sinusoidal the reflected field is almost step-like in shape, i.e. the electric field exhibits strong jumps at the instances when the surface moves toward the observer with maximum velocity.

Figure 2.4 shows the power spectra of reflected pulses for different laser intensities

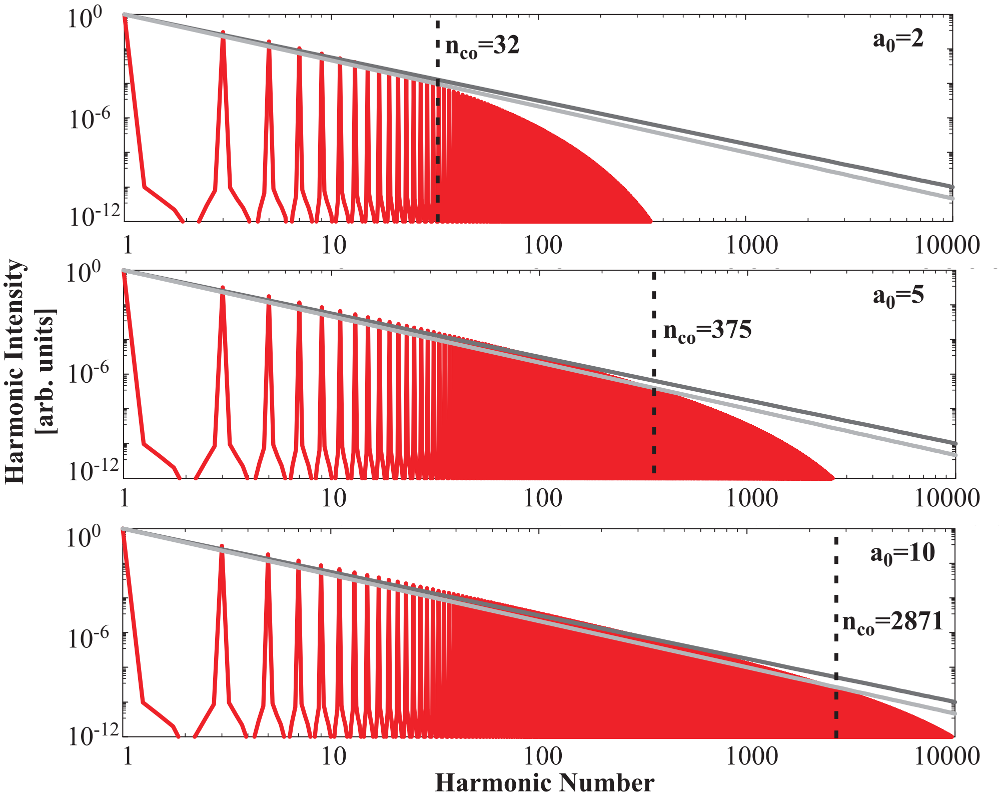

Figure 2.4: Harmonic spectra for three different laser intensities. The gray lines correspond to power law roll-offs of $\omega^{-5/2}$ (dark gray) and $\omega^{-8/3}$ (light gray). The cut-off was calculated from the laser intensity using the theoretical prediction $q_{\text{co}} \approx \sqrt{8}\gamma_{\text{max}}^3$. For comparison the cutoff predicted in [37] is indicated by the light gray dashed line. Good agreement of the simple model with the theoretical predictions can be observed.

(note that in this case infinitely long driving pulses where assumed). The spectra all exhibit the same features. Only odd harmonics are observed owing to the $2\omega_{\text{L}}$ periodicity of the assumed surface motion and all spectra show a slow power-law roll-off up to a certain cutoff and then decay exponentially for higher harmonics. If one assumes a driving force periodic with ω_{L} rather than $2\omega_{\text{L}}$ the spectra show the same features except that all harmonics are observed as one would expect from the periodicity of the driving force.

The power-law decay and the cutoff observed with this simple model calculation match remarkably well to the theoretical predictions in [30] and have recently been verified in a set of experiments [58, 61]. The theoretical $\omega^{-8/3}$ roll-off and the $\omega^{-5/2}$ decay predicted earlier [37] are shown in figure 2.4 in light and dark gray respectively. Both predictions are found to be very close to the calculated spectra.

The cutoff shown in figure 2.4 is also calculated from the predictions in [30]. The cutoff harmonic is given by the theory to be

$$q_{\mathrm{co}} \approx \sqrt{8}\gamma_{\mathrm{max}}^3, \tag{2.27}$$

where γ_{max} is the maximum gamma-factor of the surface moving toward the incident electromagnetic wave. Note that this functional dependence of q_{co} on γ_{max} is different from all earlier theories which predict $q_{\mathrm{co}} \propto \gamma_{\mathrm{max}}^2$ and an exponential decay beyond this point. Nonetheless the γ_{max}^3 scaling is quoted here since it matches the calculations from the mirror model better and, much more importantly, has been confirmed in recent experiments [58, 61]. It is important to not however that the gamma squared cutoff is not completely wrong either. As is pointed out in [30] it indeed indicates the end of the power-law spectrum. The exponential decay, however, does not start before γ_{max}^3. In the intermediate region the spectrum decays a little bit faster than the power-law but much less than exponential.

Even though the γ_{max}^3 scaling seems to contradict the predictions by Einstein for the relativistic Doppler shift [82] of an electromagnetic wave reflected from a moving mirror it can be understood intuitively. The key lies in the fact that Einstein only considers a mirror moving at a constant velocity close to the speed of light in the direction of the observer. In this case he derives a frequency upshift by a factor $4\gamma_{\mathrm{max}}^2$. In the case of the oscillating mirror the picture is quite different. The moments in time when the velocity of the mirror is maximum is confined to a very small time window within each oscillation cycle of the surface. In fact it can be shown that the temporal width of these velocity spikes scales as $\Delta t \propto \gamma_{\mathrm{max}}^{-1}$ [30]. Considering Heisenbergs uncertainty principle, i.e. $\Delta t \Delta\omega = const$ immediately shows that the frequency spectrum is broadened by an extra factor γ_{max} owing to the temporal confinement of the emission. Together with the 4 γ_{max}^2 frequency shift predicted for the moving mirror this gives a total up-shift proportional to γ_{max}^3.

In conclusion this discussion shows that the relativistic oscillating mirror harmonics show some very interesting properties:

- Their generation is independent of the target material as long as a sufficiently smooth plasma surface is formed. The influence of surface roughness on the harmonic generation is studied experimentally in Chapter 5 of this thesis.

- The roll-off of the harmonic power spectrum is universal, i.e. independent of the exact surface motion, and the highest harmonic that can be generated depends only on the focused intensity of the driving laser. Moreover the scaling of the cutoff harmonic and the conversion efficiency is so favorable that, assuming the harmonics can be focused to a near diffraction limited spot, intensities much higher than those of the driving laser could, in principle, be achieved [32] pushing the frontier of high-field science toward the Schwinger limit [33] where the generation of electron-positron hole pairs from vacuum is predicted to occur.

- The generated harmonics are fully coherent and the phase relation between the highest harmonics is predicted to be linear [30]. This means that the oscillating mirror mechanism should generate attosecond pulses of fourier limited duration that carry negligible chirp. This prediction is also supported by PIC simulations [38].

2.2.2 Coherent Wake Emission

In contrast to the ROM harmonics which are generated at the surface of the target coherent wake emission (CWE) is a bulk process, i.e. the harmonics are generated inside the overdense bulk plasma. While the fact that harmonics can be generated inside an overdense plasma gradient is known since the late 1970s [41–44] it was only recently that u. Teubner et al. and F. Quéré and coworkers clarified the generation process for femtosecond pulses [34, 54].

They attribute the generation of harmonics inside the bulk plasma to bunches of hot electrons (Brunel electrons [81]) which are first pulled out of the plasma by the component of the laser electric field perpendicular to the target surface to be hurled back inside when the field reverses. The hot electrons propagate through the density gradient and excite plasma waves in their wake. These plasma waves can, under certain conditions, undergo linear mode conversion and radiate electromagnetic waves. This process is essentially inverse resonance absorption and is described for example in [90]. It is important to note that CWE harmonics can only be generated in plasmas that have a finite scale-length. If the density profile is step-like it cannot generate any harmonics [35] because plasma waves with frequencies corresponding to the harmonics cannot be excited. Under very high contrast interactions this can lead to the suppression of the emission of lower order CWE harmonics [91].

The indirect generation of harmonics via hot electrons and plasma waves results in several unique properties of the generated harmonics which distinguish them clearly from the ROM harmonics introduced in the previous section. Most importantly the CWE harmonics can be generated at sub-relativistic intensities ($a_0 \ll 1$) as low as $1 \times 10^{16} W\ cm^{-2}$ [34]. This in fact makes the conclusions of some earlier experimental publications, especially [52], seem rather questionable as they attribute their measured harmonics to the ROM mechanism despite having used non-relativistic laser pulses not taking into account that the properties of the two types of harmonics are completely different. In fact, harmonics as high as the ones reported in [52] should not be generated at all for their experimental conditions. Most probably the supposed harmonics are in reality incoherent atomic emission lines.

Besides the intensity necessary for the generation there are two more interesting differences between CWE and ROM. The highest generated harmonic for CWE does not depend on the laser intensity but rather on the properties of the target material and there are two kinds of chirp on the emitted harmonics. Both effects, the cutoff and the chirp, can be understood when looking at the harmonic generation mechanism in a little more detail.

Let us consider the cutoff first. As has been mentioned above the harmonics are generated via mode conversion of plasma waves excited by hot electrons in the pre-plasma gradient of the target. The wavelength of the generated harmonic is thus directly related to the frequency of the excited plasma wave which, in turn, is a function of the local electron density. This means that each harmonic is generated at a different depth within the density gradient and that the highest generated harmonic q_{co} can be calculated from the maximum electron density of the target and the laser wavelength (with its corresponding critical density n_{c}). It is:

$$q_{\mathrm{co}} \approx \sqrt{\frac{n_{\mathrm{max}}}{n_{\mathrm{c}}}}. \tag{2.28}$$

For typically used target materials q_{co} lies between 14 for low-density plastics like polymethylmetacrylate (PMMA) and 20 for BK7-glass or fused silica. In principle higher cutoff harmonics should be achievable from high-density lead glass or metal targets. The dependence of the spectral cutoff on the target density for CWE harmonics has been shown in several publications [57, 63, 70].

The fact that the harmonics are generated indirectly via Brunel electrons exciting plasma waves inside the target leads to two different kinds of chirp, a harmonic chirp inside each harmonic and an atto-chirp between the harmonics. The harmonic chirp originates from the fact that the Brunel electrons spend different amounts of time in the vacuum before they are injected into the plasma gradient depending on the instantaneous laser intensity. This leads to the emission of unequally spaced attosecond pulses as has been shown in detailed PIC simulations by F. Quéré et al. [35] and will also be discussed in Chapter 6. Experimentally this unequal spacing is observed as a broadening of the individual harmonics that can be at least partially compensated by properly chirping the incident laser pulse to minimize the unequal spacing [34, 35, 60]. The influence of this effect on the temporal coherence of CWE harmonics and on the harmonic spectra generated with intense few-cycle lasers is discussed in detail in chapters 4 and 6 of this thesis and the publications resulting from these measurements [62, 67].

In contrast to the harmonic-chirp the atto-chirp, i.e. the chirp between the individual harmonics, originates from the fact that the wavelength of the generated harmonic relies

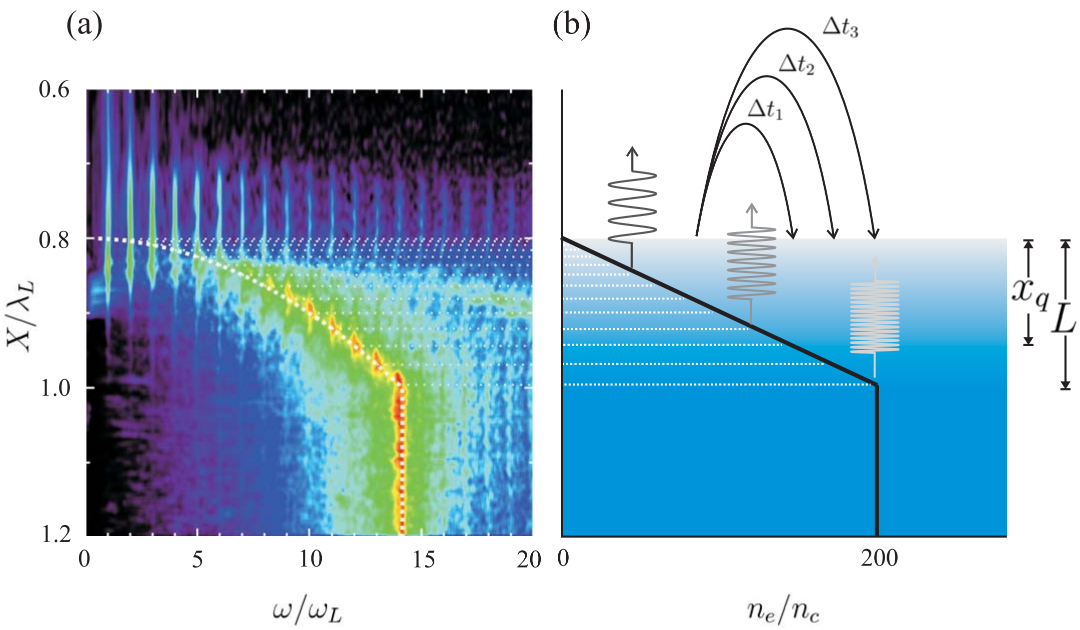

Figure 2.5: Figure illustrating the basic features of CWE harmonics. Panel (a) shows the nonlinear currents inside a target with a maximum density $n_{\mathrm{max}} = 200n_{\mathrm{c}}$ and a linear density ramp of length $L = 0.2\lambda_{\mathrm{L}}$ irradiated with a peak laser intensity of $a_0 = 1.5$ as obtained from a PIC simulation (Simulation courtesy of S. Rykovanov). Different frequency currents are seen to be resonant at different depth inside the density ramp corresponding to those positions where the local plasma frequency $\omega_{\mathrm{p}} = q\omega_{\mathrm{L}}$. The harmonic cutoff predicted by equation 2.28 is also visible. In (b) the two origins of chirp in CWE harmonics are shown schematically. While the fact that harmonics are generated at different depth inside the target leads to a chirping of the individual attosecond pulses the different excursion times of the electrons as a function of the driving laser intensity leads to unequal spacing of the individual as-pulses.

on the local electron density. Higher harmonics are generated further inside the density gradient and thus have to travel a longer distance to the target surface than the lower orders. This effect is depicted in figure 2.5 both schematically (b) and in the results of a PIC simulation (a). The simulation shows the currents inside a plasma gradient of length $L = 0.2\lambda_{\mathrm{L}}$ as a function of position and frequency. Higher frequency currents are resonant deeper inside the target where the density is higher. At the same time the simulation also nicely shows the cutoff for the generation of plasma harmonics. The highest resonant frequency is 14 ω_{L} which corresponds to the peak density of $n_{\mathrm{max}} = 200n_{\mathrm{c}}$ used in the simulation (see equation 2.28).

The attosecond-pulses generated by the superposition of the individual CWE harmonics will carry a chirp depending on the scale-length of the preplasma density gradient and the velocity of the Brunel electrons causing the excitation of the plasma oscillations. To quantify this chirp and help in interpreting the results of our direct XUV-autocorrelation of the generated attosecond pulses ([63] and chapter 4) we have developed a simple model for the atto-chirp which shall be discussed in the following.

The starting point for the model is a linear density gradient of length L over which the electron density in the target rises from zero to n_{max} (see figure 2.5). The density as a function of position x can then be written as

$$n_{\mathrm{e}}(x) = \frac{x}{L} n_{\mathrm{max}}. \tag{2.29}$$

Considering that the relation between the local electron density and plasma frequency is $\omega_{\mathrm{p}} \propto n_{\mathrm{e}}^2$ (see equation 2.18) it is possible to calculate the position $x(q)$ inside the gradient at which the individual harmonics are generated:

$$x(q) = L \frac{n_{\mathrm{c}}}{n_{\mathrm{max}}} q^2 \tag{2.30}$$

Note that this parabolic behavior with harmonic number is also nicely reproduced by the PIC simulation shown in figure 2.5.

To calculate the relative phase between the individual harmonics from the position at which they are generated two things have to be taken into account: the time it takes for the Brunel electrons to travel to the point in the gradient where the harmonic of interest is generated and the additional phase shift originating from the time it takes for each harmonic to propagate out of the gradient. In general terms the phase accumulated by the q-th harmonic is

$$\phi(q) = 2\pi \frac{L}{\lambda_{\mathrm{L}}} \frac{n_{\mathrm{c}}}{n_{\mathrm{max}}} q^3 \left[\frac{c}{v_{\mathrm{e}} \cos\left(\Theta_{\mathrm{in,e}}\right)} + \frac{c}{v_{\mathrm{ph}} \cos\left(\Theta_{\mathrm{out,ph}}\right)} \right], \tag{2.31}$$

where the first term in the round brackets accounts for the electron propagation into (v_{e} is the electron velocity and $\Theta_{\mathrm{in,e}}$ the angle of incidence (AOI) of the electrons onto the target) and the second for the propagation of the harmonics out of the gradient (with v_{ph} being the local speed of light inside the plasma and $\Theta_{\mathrm{out,ph}}$ the angle under which the harmonics are emitted).

While the photon term can be evaluated using the index of refraction of the plasma (equation 2.20) and only results in a correction factor in the case of a linear density ramp (for the detailed calculation see [69]), the main problem is the treatment of the electron term. Since v_{e} and $\Theta_{\mathrm{in,e}}$ are generally unknown parameters and difficult to calculate a reasonable assumption has to be made. While this is not easy for the general case two limits can be treated. For laser intensities of $a_0 \ll 1$ the electron propagates roughly in

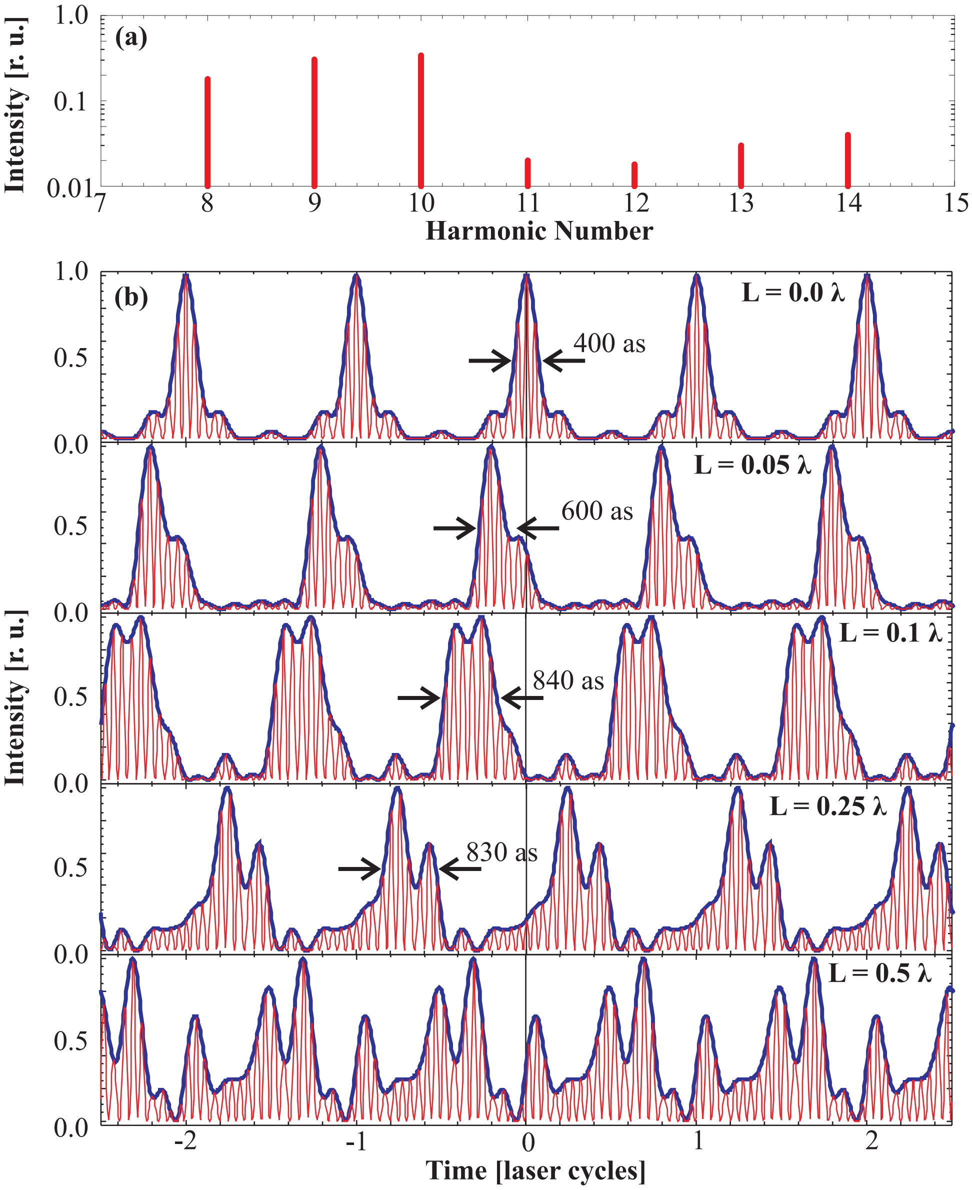

Figure 2.6: Calculation of chirped attosecond pulse trains. (a) Shows the power-spectrum used in the calculations. It is derived assuming the transmission of equal intensity harmonics through a 150 nm indium filter. (b) Depicts the pulse trains resulting from fourier transforming the spectrum (a) with a relative phase between the harmonics given by equation 2.32 for different pre-plasma scale-lengths.

the direction of the electric field of the incident laser and its velocity can be estimated using equation 2.12. In the relativistic limit, i.e. for $a_0 > 1$, we can assume $v_\mathrm{e} \approx c$. For the relativistic case and an angle of incidence of 45 degrees, which is close to the experimental conditions in our autocorrelation measurements ([63, 69] and chapter 4), equation 2.31

reduces to

$$\phi(q) = 2\pi \frac{L}{\lambda_{\mathrm{L}}} \frac{n_{\mathrm{c}}}{n_{\mathrm{max}}} q^3 (\sqrt{2} + \frac{2}{3}\sqrt{2}). \tag{2.32}$$

Here the factor of $\sqrt{2}$ simply originates from the angle of incidence and the 2/3 results from the propagation of the harmonics inside the density gradient.

To get a feeling of how this phase relation between the harmonics influences the generated attosecond pulses the results of a model calculation are shown in figure 2.6. The parameters where chosen to be close to typical experimental conditions in our setup. Assuming that all harmonics up to the CWE cutoff are generated with equal intensity on a PMMA target with a peak density of $n_{\mathrm{max}} = 200\ n_{\mathrm{c}}$, the harmonic comb is filtered with a 150 nm indium filter just like in our measurements (the transmission data of the filter is taken from [92, 93]). The resulting harmonic power spectrum used in the calculation is shown in figure 2.6 (a). The spectrum is then fourier transformed to the time domain assuming the phase relation between the harmonics given by equation 2.32 for different scale-lengths L. The resulting pulse trains are shown in the various plots of figure 2.6 (b). The duration of the individual attosecond pulses in the train is also indicated in the figure. Note that for the longest scale-length quoting a full width at half maximum (FWHM) pulse duration does not make much sense. An interesting evolution of the attosecond pulse duration with the scale length can be observed. With increasing chirp the pulse duration rapidly rises from approximately 400 as to values around 850 as and stays there over a wide range of scale length. For values of L approaching λ the pulses are distorted so severely that it becomes difficult to identify individual wagons in the train.

Even though this model can, owing to its simplicity and the assumptions made, only give a qualitative picture of the influence of chirp on the attosecond pulses generated via the CWE mechanism it is remarkable how well it seems to reproduce the measured results. For reasonable values of the preplasma scale length 0.05λ and 0.25λ the pulse duration deduced from the model is, to within the experimental accuracy, close to the measured value of roughly 900 as [63, 69]. It is also interesting to note that corrections in the electron velocity and AOI toward more realistic values will only change the magnitude of the chirp slightly. It does not have any influence on the functional behavior of the phase with q. One possibility to increase the precision of the model could be to extract the electron velocity and AOI from a PIC simulation and enter those values into equation 2.31 [94].

In conclusion the overview over CWE harmonics given in this section shows that they have unique properties with which they can be distinguished from ROM harmonics.

- The highest achievable harmonic is determined by the maximum density of the target material and not by the laser intensity. This limits the spectral range to harmonics around the 20^{th} order of an 800 nm laser for commonly used BK7-glass targets. Slightly higher harmonics should be achievable with very high density targets. Even though these cutoffs are much lower than for ROM harmonics a distinct cutoff in the harmonic spectrum can be helpful for some applications [63, 70].

- There is no universal spectral roll-off. The relative intensities of the individual harmonics are determined by the shape of the preplasma gradient [91].
- The generated attosecond-pulses are unequally spaced in time and inherently chirped owing to the fact that the harmonics are generated indirectly via Brunel electrons at different depths within the density gradient.

Chapter 3

Laser Systems

Achieving the ultra-high-intensity electro-magnetic fields necessary for the generation of high harmonics from solid surfaces is a key requirement in the study and eventual application of this radiation source. For this reason the laser systems used to generate the harmonics investigated in this thesis shall be described in more detail in this chapter. The focus is laid on the two systems at the MPQ, the ATLAS laser used for the experiments described in chapter 4, and the LWS10 system with which the experiments in chapter 6 where conducted. The ASTRA laser at the Rutherford Appleton Laboratory, results from which are presented in chapter 5, is similar to the ATLAS laser in its concept and beam parameters and shall not be discussed here. Details on the ASTRA laser can be found, for example, in [95].

In order to generate very high power pulses with moderate-size table-top laser systems it is necessary to amplify pulses with a few to a few tens of femtoseconds duration. Only in this case will pulse energies of a few hundreds of millijoules be sufficient to achieve focused intensities exceeding the relativistic limit (see section 2.1.1). Furthermore the short pulses lead to a short burst of XUV radiation which is desirable when the generated harmonics are to be applied to probe ultra-fast processes.

However, when amplifying fs-duration pulses to the mJ-level the damage threshold of the optics in the amplifier chain becomes a serious issue. In fact, the beam diameters would have to be so large to keep the intensities on the amplifier crystals low that amplification beyond a few mJ would be impossible. To overcome this limitation the concept of chirped pulse amplification (CPA) was invented and successfully implemented for the first time D. Strickland and G. Mourou [96]. In CPA the broad-band weak femtosecond seed pulse is first stretched in time then amplified and finally recompressed (figure 3.1) taking advantage of the fact that the intensity in the stretched pulse is much lower than it is in the unstreched one. Stretching and compression of the pulses is achieved using optical setups with dispersive elements (for example gratings or prisms) in which different

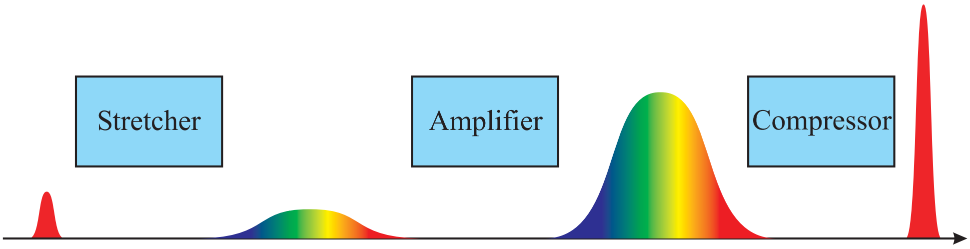

Figure 3.1: Illustration of the Chirped Pulse Amplification (CPA) scheme. A weak seed pulse is stretched in time, amplified and then recompressed to prevent damage to the optics in the amplifier chain.

spectral components of the incident pulse travel different distances resulting in an elongation of the pulse. The stretching and compression schemes implemented in the laser systems described in this chapter will be discussed in more detail in the sections 4.1.1 for ATLAS and 4.2.1 for LWS10.

To amplify the stretched fs-pulses a broad-band gain medium is required. In practically all conventional sub-100-fs high-power lasers the material of choice is Titanium-doped Sapphire (Ti:Sa). This material offers the broadest gain window of all known solid-state laser materials [97] and simultaneously has the good heat conduction necessary for high repetition rate operation. In addition Ti:Sa can be pumped using frequency-doubled Neodymium:YAG ns-lasers which are readily available. The concept of laser amplification is schematically shown in figure 3.2 (a). The pump photons excite the material to an intermediate state which quickly decays to the upper laser level. In Ti:Sa this upper laser level has a very long life time while the lower laser level decays quickly to the ground state. This leads to population inversion, i.e. a larger population of the upper laser level than the lower one. Subsequently, when a seed photon of the correct wavelength passes through the pumped crystal, the process of stimulated emission of a coherent photon is more probable than the absorption of the seed photon leading to an amplification of the seed beam. More details on the process of laser amplification can be found in many textbooks, for example in [74, 97–99].

Using Ti:Sa amplifier crystals multi-TW peak power laser systems with pulse durations as short as 20 fs with a central wavelength around 800 nm and 10 Hz repetition rate can be realized [100] and a whole group of systems with pulse durations on the order of 40 fs exist around the world including the ATLAS laser that shall be described in more detail in the following section. The lower pulse duration limit and the central wavelength are defined by the properties of the gain material while the heat deposition from the decay to the upper and from the lower laser level limits the repetition rate of such a laser system.

When amplification of even shorter pulses and/or pulses with different central wavelengths is desired a different amplification process is required. Optical parametric amplifi-

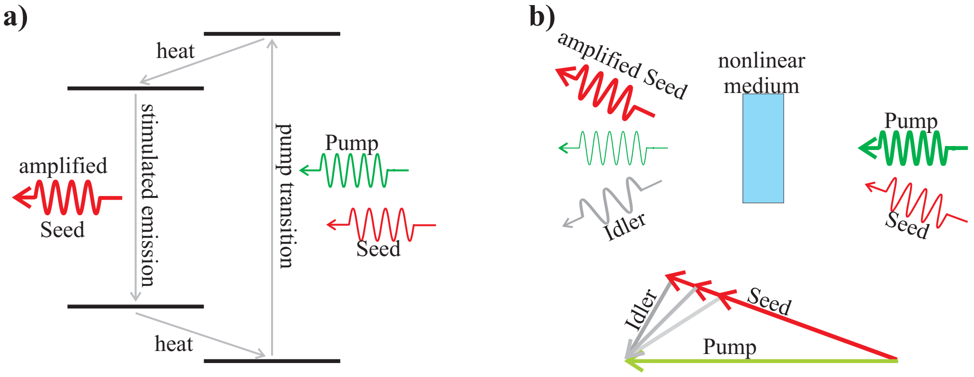

Figure 3.2: Schematic drawings of the two amplification processes used in the ATLAS and LWS10 systems. (a) Shows classical LASER amplification (Light Amplification through Stimulated Emission of Radiation) in a four-level system and (b) sketches amplification through the NOPA-process (Noncollinear Optical Parametric Amplification) in a nonlinear crystal.

cation (OPA) in a nonlinear crystal (for example beta barium borate (BBO) or potassium dihydrogen phosphate (KDP) [101]) offers the opportunity for such broad-band amplification. OPA is a third-order nonlinear process in which a weak seed pulse and a strong pump pulse mix in a process which amplifies the seed and depletes the pump. At the same time the idler wave at the difference frequency between pump and seed is generated to satisfy the condition of energy conservation. This is shown schematically in figure 3.2 (b). In OPA the amplification bandwidth is not determined by the gain-bandwidth of the crystal but rather by the phase-matching condition. OPA only works efficiently when the pump and the seed wave are in phase inside the nonlinear crystal. Thus the gain window and bandwidth can be engineered by the choice of the proper materials, crystal thicknesses and by introducing an angle between the pump and seed beams (noncollinear optical parametric amplification (NOPA)). Aside from this there is another important difference between OPA and laser amplification: In OPA the energy from the pump pulse is directly transferred to the seed pulse and not stored in the amplifying medium like in a laser. This requires exact synchronization between the seed and pump beams making the implementation of OPA in large systems technologically challenging but offers the great advantage that negligible amounts of heat are deposited in the OPA-crystals. This offers the possibility to build high repetition-rate high-power amplifiers. More detailed discussions of OPA can be found, for example, in [102]. Using this technique pulses with spectra spanning several hundred nanometers in bandwidth have been amplified at different central wavelengths ranging from the visible to the infrared and large petawatt-class systems based on OPA are currently under construction [103]. The main amplifiers of the LWS10 system are also based on NOPA and will be described in more detail in section

3.2.

3.1 ATLAS Upgrade

In this section the upgraded Advanced Titanium:sapphire LASer (ATLAS) will be described in more detail. The system is based on the original ATLAS 10 laser installed at the MPQ in 1996 [104] but has been completely reconstructed and upgraded in 2005 to bring it to the state-of-the-art in Ti:Sa technology. In fact, the work on this upgrade has consumed a large portion of the first year of my PhD-work and was the prerequisite for a whole series of experiments and subsequent publications in the field of high-field science [63, 67, 70, 105–109].

The description of the laser will be divided into two parts, where the first one (section 3.1.1) focuses on the setup of the laser while the second part (section 3.1.2) gives an overview over typical operating parameters of the laser during experimental runs.

3.1.1 Laser Setup

As has been mentioned before the ATLAS laser is based on conventional Ti:Sa technology. A series of four amplifiers is used to amplify the nJ-level pulses from a broad-band Femtolasers Rainbow oscillator [110] to the joule-level. An overview over the laser setup is given in figure 3.3. The main focus during the reconstruction of the ATLAS laser was laid on decreasing the pulse duration while maintaining a high ns- and ps-contrast of the laser because the contrast, i.e. the ratio between the intensity of the peak of the laser pulse and its wings, is of critical importance for high-intensity laser-solid interaction experiments. If the contrast is not sufficient the wings of the laser pulse will ionize the solid target long before the main pulse arrives leading to the interaction of the pulse peak with a long-scale preplasma rather than a sharp density gradient.

The main source of unwanted ns-background and thus limited ns-contrast is amplified spontaneous emission (ASE) from the amplifier crystals [97]. Especially the regenerative amplifier seriously reduces the laser contrast when it is seeded with very weak pulses because ASE can be further amplified when it is trapped in the laser cavity. For this reason a 10 Hz 8-pass Ti:Sa preamplifier was constructed in front of the stretcher to boost the seed energy for the regenerative amplifier. This lead to an improvement of the ns-contrast of the laser by more than one order of magnitude. After pre-amplification the pulses are stretched to a duration of 350 ps and a pulse picker is used to select pulses at 10 Hz from the pulse train generated by the oscillator. The timing of the pulse picker is adjusted such that the highest energy pulses from the pre-amplifier are transmitted for further amplification while the weaker ones are rejected. The transmitted pulses are

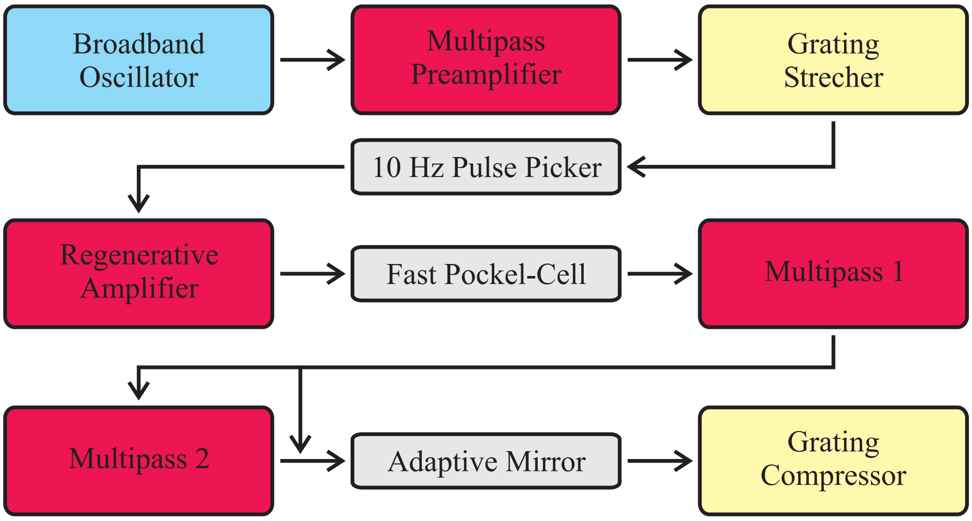

Figure 3.3: Overview of the main components of the ATLAS 25 TW Titanium:sapphire laser system. The beam is amplified in a chain of four consecutive Ti:Sa-amplifiers and stretched and compressed using gold gratings.

then injected into a regenerative amplifier [111] and trapped in the amplifier cavity for 12 round-trips using a Pockels-cell (PC) [97]. In the regen, a schematic of which is shown in figure 3.4, the pulses are amplified from the μJ-level to approximately 18 mJ and at the same time their beam profile is cleaned owing to the fact that only light in the lowest-order spatial mode of the cavity is efficiently trapped and amplified.

Owing to the properties of the regenerative amplifier the main pulse switched out of the cavity after amplification is preceded by a series of prepulses originating from leakage from the cavity on earlier round-trips. The prepulses are spaced at multiples of 11 ns, corresponding to the cavity round-trip time, with the one leaving the cavity one round-trip before the main pulse being the strongest. In order to suppress these prepulses and the generated ASE pedestal the beam passes through two Pockels-cells after amplification in the regen. A slow PC with 5 ns switching time and a fast PC with a rise-time of approximately 200 ps are used. Each cell has a blocking-ratio better than 100:1 such that all the prepulses leaking from the regen are suppressed by four orders of magnitude. Furthermore the ASE pedestal is suppressed by two orders of magnitude up to 200 ps before the main pulse.

Since the preservation of the good contrast achieved using the pre-amplifier and the two Pockels-cells after the regen is a key concern in the subsequent amplification of the laser pulses to the Joule-level and the use of further Pockels-cells is not feasible owing to the large beam diameters after further amplification the last two amplifiers of the ATLAS system are set up in a multi-pass or bow-tie geometry to minimize ASE. In such a setup the beam is not trapped inside a cavity using a polarization rotating device and a set

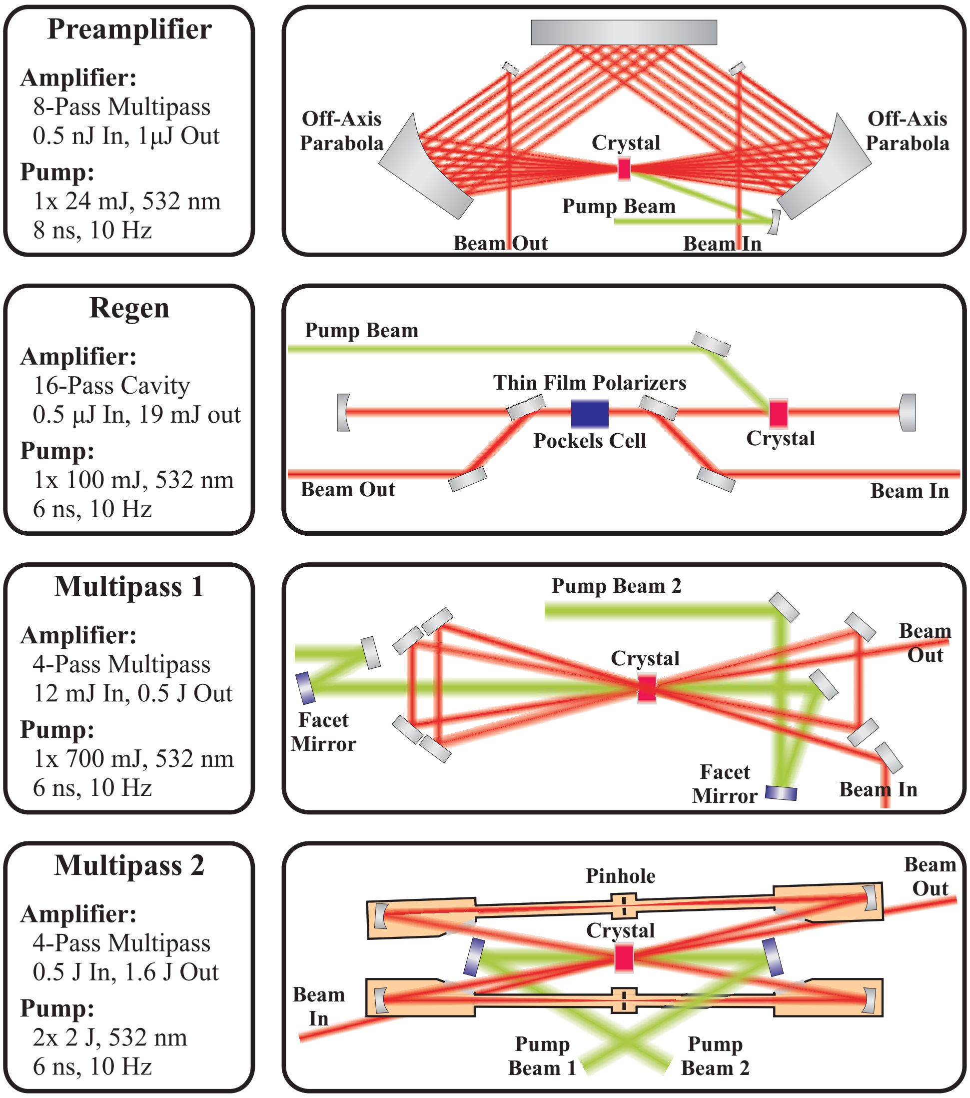

Figure 3.4: Setup and operating parameters of the four Ti:Sa amplifiers in the ATLAS laser chain used to amplify the nJ-level pulses from the oscillator to the Joule-level required for high-intensity laser-matter-interaction experiments.

of polarizers but rather simply directed obliquely through the amplifying crystal several times using a set of mirrors. Figure 3.4 shows detailed sketches of the two multi-pass amplifiers of the ATLAS laser. While this geometry prevents the generation of pre-pulses owing to the absence of polarizers in the beam from which energy could leak from the amplifier the lack of a cavity makes the conservation of a uniform beam-profile during the passes through the gain medium more difficult. For this reason it is of critical importance that the energy distribution in the pump-beam is as homogeneous as possible to prevent the generation of hot-spots in the amplified beam.

To achieve a homogeneous pump-beam profile a set of integrating mirrors [112] is used.

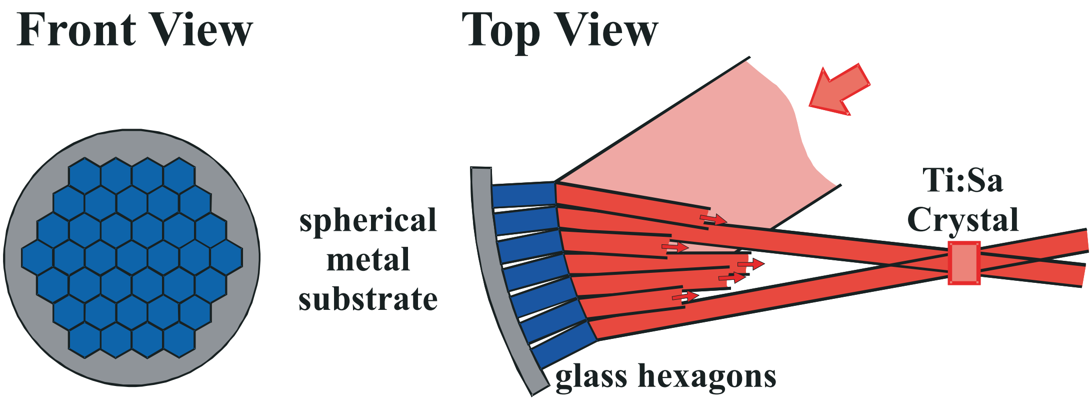

Figure 3.5: Sketch of the honeycomb-mirror used to homogenize the pump beams of the ATLAS laser. Each mirror consists of a set of planar hexagonal mirrors mounted on a curved substrate. (Figure taken from [104]).

They consist of a set of hexagonal plane mirrors mounted in a honeycomb geometry on a spherical metal substrate (see figure 3.5). The amplifier crystal is placed in the focus of the mirror substrate where the reflections from each individual plane mirror overlap. The result of this is a reduction of the pump-beam to the desired diameter without a reduction in size of individual hot-spots. This results in a pump profile with irradiance fluctuations as low as two percent for the ATLAS pump lasers [104].

For further improvement of the beam profile spatial filters [97] are used after each pass through the amplifier in the second multipass. In the spatial filter the beam is focused and subsequently recollimated using a set of spherical mirrors. A ceramic aperture is placed in the focus to reject those components of the beam with high spatial frequencies located in the wings of the focal distribution and transmit only the lower-order ones focused close to the axis. This results in a more homogeneous beam profile without hot-spots.

Depending on the pulse energy desired for the particular experiment the stretched and amplified laser beam can either be extracted with an energy of approximately 520 mJ after the first multipass or amplified to around 1.5 J using all amplifiers. Since the focusability of the amplified beam is of key concern when high focused intensities are desired for an experiment and wavefront distortions cannot be avoided during the passage of the beam through the amplifier chain the ATLAS laser is equipped with a Shack-Hartmann wavefront-sensor and a deformable mirror [113]. The sensor and the mirror are connected through a feedback-loop to optimize the wavefront of the amplified beam before it is transported to the compressor. While the focusability of the ATLAS beam is rather poor without the adaptive mirror its use allows the generation of a high-quality focus even with short focal-length optics. A detailed analysis of the ATLAS focus will be presented in the following section.

After the correction of the wavefront the beam is transferred to the vacuum compres-

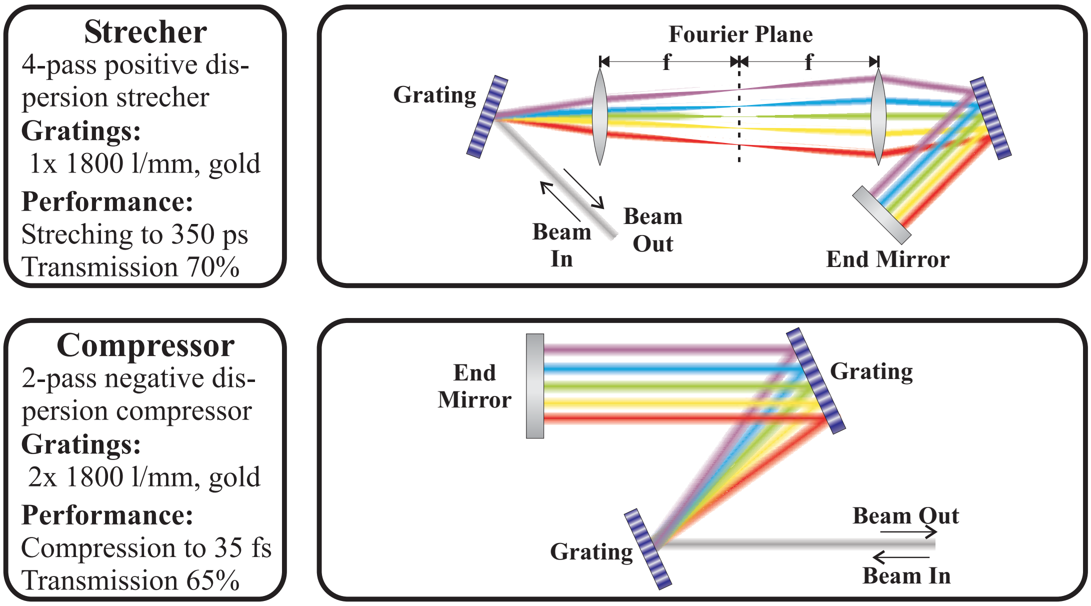

Figure 3.6: Schematic drawings of the ATLAS positive-dispersion stretcher and matching negative-dispersion compressor. Both setups are based on gold-coated 1800 l/mm reflection gratings. In addition a Dazzler is used to help in compensating higher-order dispersion for optimal compression.

sor of the ATLAS system. The negative-dispersion compressor consists of two parallel large-area (200 mm and 300 mm diameter) 1800 l/mm gold-coated holographic reflection gratings and a roof-top end mirror. It recompresses the laser beam from 350 ps down to approximately 40 fs. It is matched to the stretcher which uses a grating with the same specifications and the same angle of incidence [114] and has a transmission of roughly 60 to 70 percent resulting in compressed pulse energies of up to 1 J. Schematics of the stretcher and the compressor are shown in figure 3.6. Note that in practice the stretcher is set up with only one grating and a folding mirror in the fourier-plane of the lens. Furthermore the lens is replaced by a spherical mirror in the ATLAS system. Nevertheless the operating principle of the stretcher stays the same and the unfolded version is shown in figure 3.6 for clarity. Recently a DAZZLER [115] has been included in the laser chain to assist in compensating higher-order dispersion in the system and achieve even shorter pulses.

While the ATLAS laser system is a very versatile and reliable tool for high-field physics experiments several improvements are planned for the near future to make it even more useful. In a first step the output energy of the system will be doubled by adding extra pump-power to the last amplifier. In a second step it is planned to replace the front-end up to the regenerative amplifier with a new more broad-band system to decrease the pulse duration to approximately 20 fs. In parallel a plasma mirror is under construction to further improve the contrast of the compressed laser beam. For details on plasma mirrors see Appendix A.

3.1.2 Operating Parameters

To ensure optimal operation of the ATLAS system during experiments a whole set of beam parameters are routinely monitored. In the following an overview over the most important characteristics of the ATLAS pulses will be given.

As has been mentioned above the uncompressed pulse energy of the ATLAS laser is roughly 520 mJ after the first multipass and 1.5 J after the final amplifier. Depending on the energy necessary for the respective experiment the beam can be compressed either after the first or after both multipass amplifiers. Typical pulse energies after compression are 350 mJ and 900 mJ respectively. The shot-to-shot energy fluctuations are approximately 5 percent RMS.

To ensure that the amplified pulses are indeed compressed to the shortest possible pulse-duration they are characterized regularly using a GRENOULLIE device [116] based on the frequency resolved optical gating (FROG) technique [116]. Figure 3.7 shows the result of such a measurement. From the raw FROG-image (a) the pulse duration (b) as

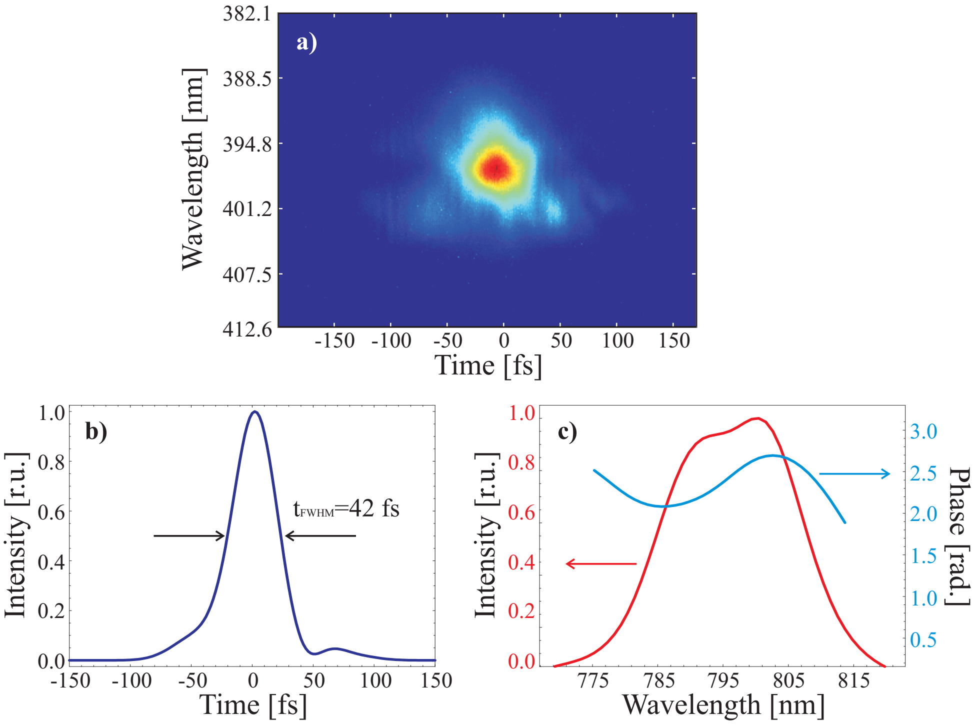

Figure 3.7: Temporal characterization of the ATLAS laser pulses with the FROG technique. The subplots show (a) the raw FROG image, the reconstructed temporal structure of the pulse (b) and its spectrum and spectral phase (c).

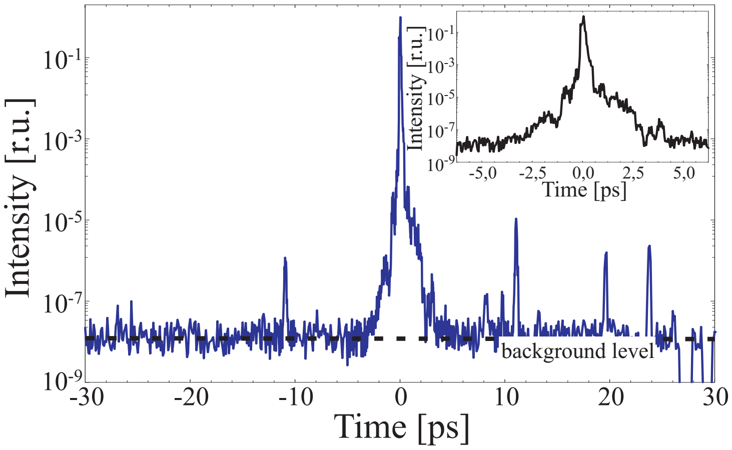

Figure 3.8: Third-order scanning autocorrelation of the ATLAS laser output for measurement of the ps-contrast. The inlay shows a more detailed view of the region close to the peak of the pulse. The maximum measurable contrast is limited to 1:10^8 by the dynamic range of the correlator.

well as the spectrum and the spectral phase (c) of the pulse can be reconstructed. From the spectral phase it is clearly visible that there is some residual higher-order phase distortion on the beam. Nevertheless the 24 nm bandwidth spectrum of the pulse is compressed to a duration of 42 fs. Note that this measurement was conducted before the DAZZLER was installed on the laser for optimized compensation of higher-order dispersion. With the DAZZLER pulse durations as short as 33 fs have been achieved [117].

While the GRENOULLIE can be used to determine the pulse duration accurately it is not capable of analyzing the pulse structure in a time window larger than ±250 fs. However, the knowledge of the ps-contrast of the laser pulses is of great importance for high-intensity laser–solid interaction experiments as early ionization caused by pre-pulses leads to fast expansion of the target surface resulting in an interaction of the main laser pulse with a long scale-length pre-plasma rather than a sharp interface. To characterize the ps-contrast of the ATLAS laser a custom-built third-order scanning autocorrelator (AC) [118, 119] was used. A typical AC-trace is shown in figure 3.8. On the leading edge of the pulse the intensity drops quickly to the detection threshold of the correlator corresponding to a contrast 1:10^8 at 4 ps before the main pulse. Note that the prepulse at 2 ps before the main pulse originates from the correlator [120] suggesting that the contrast may be even better. The pre-pulse visible 11 ps before the main pulse is a ghost of the corresponding post pulse and is consequently, like the other post pulses, of no relevance in the analysis of the contrast as it arrives at the target after the interaction with the main pulse. While the contrast of the ATLAS laser is already very good further improvement is expected from the front-end upgrade and a plasma mirror which is currently under construction.

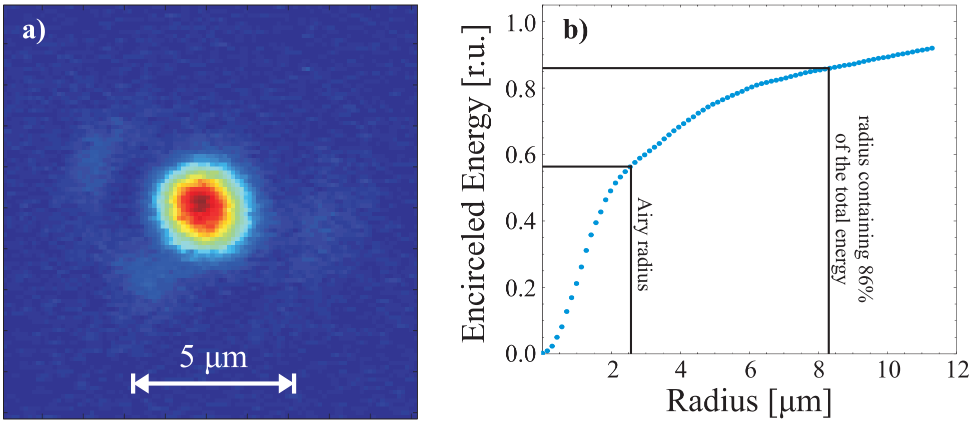

Figure 3.9: Typical focal spot of the ATLAS laser measured in the SHHG chamber. The beam was focused using a 4 inch 30° off-axis polished fused silica parabola with an effective focal length of 160.8 mm corresponding to an F-number of approximately F/2.3. (a) Shows a background-subtracted camera image of the focal spot and (b) gives the encircled energy fraction in the focus as a function of the radius. This can be used to calculate the average intensity in the laser focus.

Finally the high-contrast fs-pulses need to be focused as well as possible to achieve maximum intensity in the interaction region. For all experiments on SHHG conducted at the MPQ a high-quality 4 inch 30° off-axis parabola with an effective focal length of 160.8 mm was used for focusing the laser beam. The corresponding F-number for the ATLAS beam diameter is approximately F/2.3. To monitor the quality of the laser focus it is magnified and imaged onto a beam profiler using an F/2 aspheric objective. An image of a typical focal spot is shown in figure 3.9 (a). Aside from the round main peak a weak halo can be observed around the focus. This halo originates from the fact that the beam-profile of the ATLAS laser is not Gaussian but rather close to a flat-top resulting in an Airy-shaped focus. To analyze the quality of the focus in more detail and estimate the focused intensity the encircled energy fraction as a function of radius, i.e. the ratio between the energy contained within a certain radius around the peak of the pulse and the total energy, is calculated from the image of the focal spot. The results of this calculation

Area	Radius	Intensity	a_0
Peak	0 μm	8.0×10^{19} W/cm^2	6.1
Airy	2.5 μm	3.1×10^{19} W/cm^2	3.8
1/e^2	8.3 μm	4.4×10^{18} W/cm^2	1.4

Table 3.1: Averaged and peak focused intensities calculated for different characteristic radii of the ATLAS focal spot.

are shown in 3.9 (b).

From the encircled energy fraction one can now calculate the focused intensity of the ATLAS laser beam in the SHHG chamber. Since many different conventions are used for defining the average focused intensity three values shall be given here: The peak intensity, the average intensity inside the first Airy-minimum and the average intensity over the radius containing 86 percent of the energy. For an energy of 700 mJ on target, a pulse duration of 45 fs and 45° angle of incidence the corresponding intensities are shown in Table 3.1. This analysis proves that we can indeed reach intensities well beyond the relativistic limit when the ATLAS laser is well focused using a short focal-length parabola.

The measurements presented here demonstrate that the rebuilt ATLAS laser system performs very well in all important parameters and can be a reliable tool for high intensity laser-matter-interaction experiments.

3.2 LWS 10

In contrast to ATLAS the LWS10 system (Light Wave Synthesizer 10 TW) [118, 121–124] has been newly developed over the past couple of years at the MPQ. It is the first laser system worldwide combining multi-TW pulse power with sub-10-fs pulse duration opening the route to novel experiments in several fields of high-field science [62, 125]. The main difference to conventional laser systems is that LWS10 relies on OPCPA (an abbreviation combining OPA and CPA [126]) instead of laser amplification to overcome the limitations in gain-bandwidth of conventional systems and amplify pulses with a spectral bandwidth exceeding 200 nm to the 100 mJ range.

Like in the previous section on the ATLAS laser this section is divided into two parts, where the first one (section 3.2.1) focuses on the setup of the LWS10 system while the second part (section 3.1.2) gives an overview over the performance of the system during the experiments presented in chapter 6 of this thesis.

3.2.1 Laser Setup

As has been mentioned before the LWS10 OPCPA system is based on newly developed technology and is still undergoing constant improvement and upgrading. In the context of this thesis it shall be described in the state it was in during a period between the middle of 2007 and the middle of 2008 when, amongst others, the results presented in chapter 6 were obtained. A schematic overview over the setup is shown in figure 3.10.

Like in any high-power system the main concern during construction, besides generating short pulses and high pulse energies, is maintaining a high contrast of the laser pulses. Initially LWS10 was designed to directly amplify the broadband but weak pulses from a

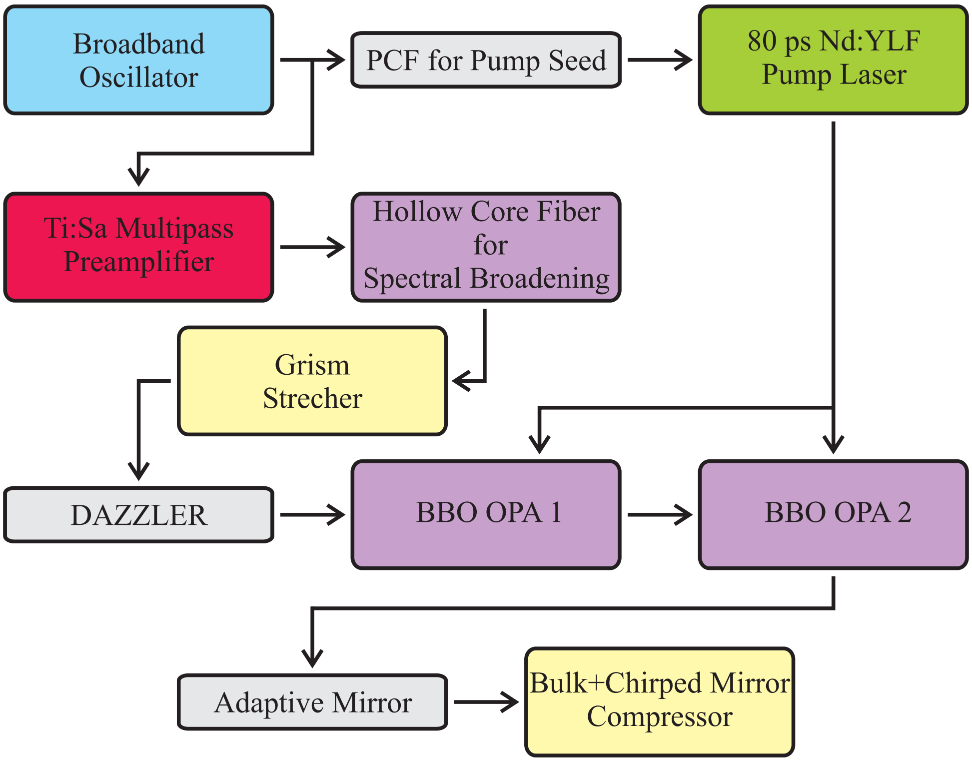

Figure 3.10: Overview of the setup of the LWS10 10 TW, 8 fs light wave synthesizer. The system is based on a Ti:Sa front-end for the generation of broadband seed pulses and a custom built OPCPA-based amplifier chain. The pump laser is seeded from the same oscillator providing the seed pulses to ensure optical synchronization of pump and seed in the amplifiers.

Femtolasers Rainbow oscillator [110] via OPA in BBO crystals. However it was found that the contrast in this configuration is significantly reduced owing to parametric superfluorescence in the weakly seeded first OPA-stage [124] making most high-field experiments impossible. To overcome this problem a significant increase in the seed energy of the first OPA stage was necessary. To achieve this goal the front-end of the laser was replaced by a Femtopower Compact Pro oscillator, amplifier combination [2] produced by Femtolasers [127]. The new setup is still based on a conventional Ti:Sa oscillator but instead of amplifying the pulses directly from the oscillator via OPA a Ti:Sa 9-pass amplifier is used to boost the energy of the oscillator pulses to 1 mJ. While this improves the contrast of the front-end significantly it has the disadvantage that the Ti:Sa amplifier is not capable of conserving the broad bandwidth necessary for achieving sub-10-fs pulses. For this reason the pulses are broadened to a bandwidth exceeding 250 nm in a Ne gas-filled hollow-core fiber after the pre-amplifier. Despite the losses in the fiber seed pulses with energies of several hundreds of μJ instead of the nJ-pulses from the oscillator are generated with this method.

After the spectral broadening the pulses are stretched to a duration of 45 ps before further amplification. However, owing to the large spectral bandwidth of the LWS10 conventional grating stretcher and compressor combinations like the one operated on ATLAS cannot be used especially because of their low efficiency. Instead LWS10 relies on a compressor based on bulk glass (fused silica and SF57) and chirped mirrors [123, 124]. While this setup has a very high throughput on the order of 80 percent and is, unlike a grating compressor, not sensitive to the polarization of the laser beam the disadvantage of such a bulk-compressor is that the dispersion is dictated by the material properties of the glass blocks and mirrors used and cannot be tuned like in a grating compressor. Therefore a very versatile stretcher capable of compensating second- as well as higher-order dispersion is necessary. To solve this problem a negative dispersion grism (where grism stands for grating-prism) stretcher [128] was implemented on LWS10. The setup essentially looks like the compressor of the ATLAS laser with an additional prism mounted in front of each grating. In addition a DAZZLER [115] is used to compensate residual higher-order chirp. This stretcher compressor combination allows the generation of fourier-limited sub-10 fs pulses as will be discussed in some more detail in the next section.

After stretching the pre-amplified and broadened seed pulses can now be amplified in two OPA stages without degradation of the pulse contrast of the kHz front-end owing to parametric superfluorescence. For pumping of the OPA stages a 80 ps frequency doubled Nd:YAG laser delivering 600 mJ pulse energy in the green is used [124]. Owing to the OPA process the construction of this pump-laser is more difficult than for a conventional laser since, unlike a laser crystal, the nonlinear medium used in OPA does not store the energy of the pump beam. Therefore it is not possible to use conventional electronically synchronized nanosecond pump-lasers like in the ATLAS system. Instead the pump pulse duration needs to be on the order of the duration of the stretched seed pulse and the two beams need to be synchronized to within better than a picosecond. The only way to ensure this is by optically synchronizing the pump and seed beams. On LWS10 this is achieved by splitting off a part of the oscillator pulses from the main beam, frequency shifting it in a photonic-crystal fiber [129, 130] and using this to seed the pump laser. With the optical synchronization the seed pulses are amplified in two consecutive OPA stages to an energy of 70–80 mJ resulting in a pulse energy of 55–65 mJ after the compressor.

Finally LWS10 is, like ATLAS, also equipped with an adaptive mirror to compensate for spatial wave-front distortions introduced in the laser chain and especially in the bulk glass of the compressor. The adaptive mirror greatly increases the quality of the achievable focal spot and thus the intensity on target available for experiments (see next section).

As has been stated earlier the LWS10 system is still under development and is currently being upgraded. A second arm in the pump-laser doubling its output power will allow amplification of the seed pulses to 200 mJ. Simultaneously the pulse-duration of the system is reduced to 7 fs. To further improve the contrast of the laser cross-polarized-wave generation (XPW) [131–133] is implemented in the front-end system.

3.2.2 Operating Parameters

Following the description of the LWS10 setup this section will go into more detail on the beam parameters of the system. Especially for temporal characterization of the beam a whole set of diagnostics is available including a single-shot second order autocorrelator [134], a scanning third-order correlator [118, 119] and a SPIDER [135, 136].

The single-shot correlator equipped with a very thin crystal for maximum time resolution offers a convenient and quick way of characterizing the pulse duration of the LWS10 system and, in combination with a spectrometer, analyze the quality of the beam compression. Figure 3.11 shows a typical spectrum and second-order AC-trace of LWS10. The spectrum spanning a range of more than 200 nm (note that the spectrum is plotted on a linear scale) would correspond to a fourier-limited pulse duration of 7.9 fs. The measured duration of 8.0 fs routinely achieved with the system proves that the stretcher–compressor combination is capable of compressing the entire amplified spectrum. Owing to the fact that the single-shot AC is very simple to operate it is used routinely to optimize the pulse duration on a day-to-day basis.

However, while the device can be used for the characterization of the duration of the main pulse its dynamic range is not sufficient to analyze the ps-contrast of the pulses. Furthermore, the second-order device is not capable of distinguishing between pre- and post-pulses. For measurements of the contrast the same high dynamic range third-order AC also used for the characterization of ATLAS (figure 3.8) is used. Figure 3.12 shows

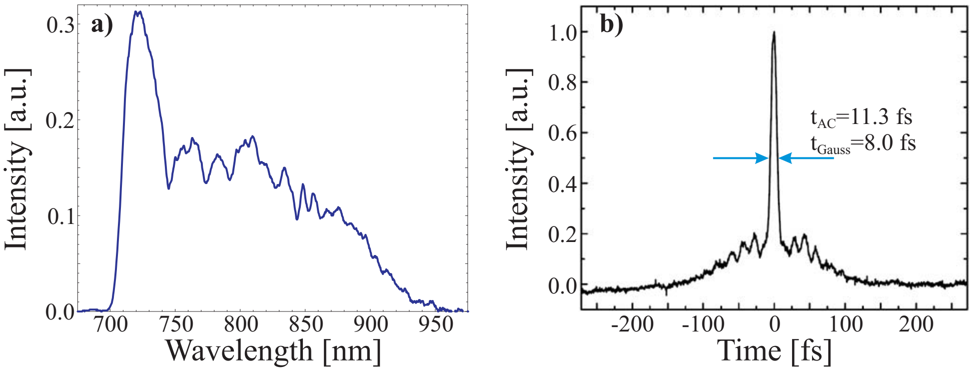

Figure 3.11: (a) Typical spectrum and (b) single-shot second-order autocorrelation trace of the LWS10 pulses. The measured duration of 8 fs corresponds to the fourier limit of the spectrum shown in (a). (AC-trace courtesy of R. Tautz [134].)

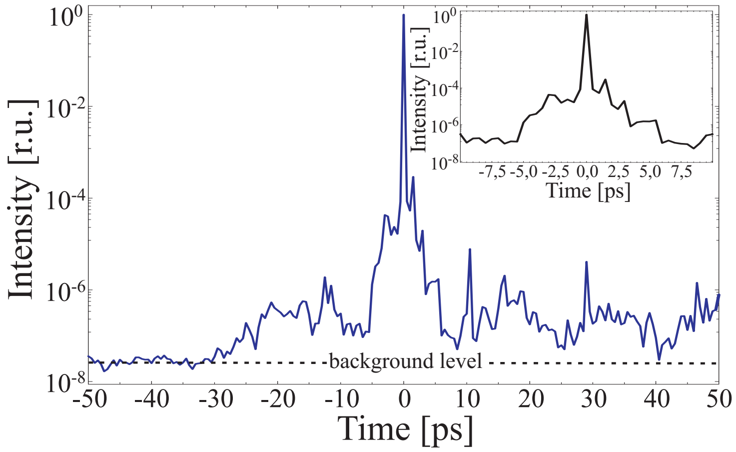

Figure 3.12: Third-order scanning autocorrelation of the LWS10 system. The inlay shows a more detailed view of the region close to the peak of the pulse. The maximum measurable contrast is limited to 1:10^8 by the dynamic range of the correlator.

a typical third-order AC-trace of the LWS10 system after contrast optimization. While the pulses are not quite as clean as in the ATLAS laser up to 30 ps before the main pulse the measurement shows that LWS10 is capable of maintaining high-contrast during amplification. However, two distinct features can be observed that limit the contrast on the few to few tens of picosecond scale: A pedestal extending 5 ps in front of and behind the pulse at a contrast of 1:5×10^5 and a longer range feature emerging from the background at about -30 ps with a contrast of 1:10^6. Recent experiments have revealed, that the two features have different sources. While the 5 ps pedestal originates from imperfect compression in the stretcher–compressor combination the long range pedestal is caused by amplification of the ASE-pedestal from the preamplifier in the OPA stages [137]. While the latter can effectively be suppressed using an XPW-stage after the preamplifier which is currently being implemented permanently in the system anyway [137] reducing the compression errors is not an easy task as it involves redesigning the stretcher and compressor of LWS10.

Finally the focusability of the LWS10 system during our experiments was routinely monitored to ensure a high focused intensity on target. It was found that, even more so than for ATLAS, the adaptive mirror is a crucial component when high-quality focal spots with short focal-length parabolas are desired. Figure 3.13 shows a typical focal spot after optimization with the adaptive mirror. In this case the beam is focused with a parabola identical to the one used in the ATLAS experiments and the focus is observed with a microscope objective and a beam profiler. Note that even though identical parabolas are used for LWS10 and ATLAS the LWS10 focus is slightly larger owing to the systems smaller beam diameter. Again the encircled energy fraction is determined from

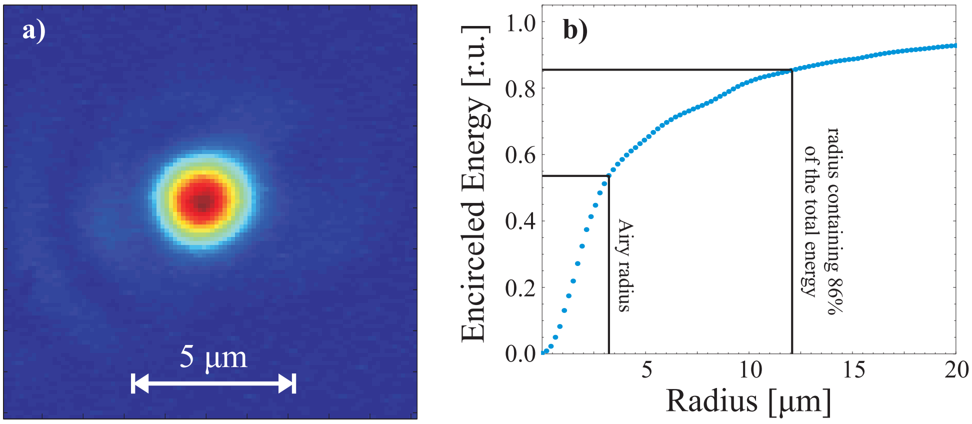

Figure 3.13: Focal spot obtained with LWS10. The beam was focused using a 4 inch 30° off-axis polished fused silica parabola with an effective focal length of 160.8 mm corresponding to an F-number of approximately F/3.2 for the 50 mm LWS10 beam. (a) Shows a background-subtracted camera image of the focal spot and (b) gives the encircled energy fraction in the focus as a function of the radius. This can be used to calculate the average intensity in the laser focus.

the image to calculate the focused intensities achieved on target. The average intensities over three characteristic areas are determined and listed in table 3.2. The values were obtained assuming 70 mJ on target, a pulse duration of 8 fs and an angle of incidence of 45°. The values are found to be slightly lower than those obtained for ATLAS (which is not surprising owing to the smaller beam diameter and slightly lower pulse-power) but nevertheless still well above the relativistic threshold inside the Airy-disc.

The measurements prove that the LWS10 system indeed reaches multi-TW peak powers and focused intensities beyond the relativistic limit with pulse durations well below 10 fs making it the first system in a new class of relativistic few-cycle lasers. Despite the fact that the development of LWS10 is far from over it is already capable of conducting novel experiments exploring high-field physics on the sub-10 fs time-scale. Future improvements will significantly increase the laser contrast and energy pushing the limit of few-cycle laser technology into the range of 100 of TW peak-power.

Area	Radius	Intensity	a_0
Peak	0 μm	4.5×10^{19} W/cm^2	5.5
Airy	3.2 μm	1.4×10^{19} W/cm^2	2.6
1/e^2	12.0 μm	1.7×10^{18} W/cm^2	0.8

Table 3.2: Averaged and peak focused intensities calculated for different characteristic radii of the LWS10 focal spot.

Chapter 4

Temporal Characterization of Surface Harmonics

One key advantage of surface harmonic generation over other laser-plasma based XUV-sources is the prospect of coherent phase locked emission of the radiation. In combination with the inherently broad-band emission spectrum this offers the prospect of generating ultra-intense pulses of as-duration. In terms of pulse duration and thus time resolution and peak pulse intensity this would make such a source superior to conventional K_α and X-ray laser sources [138, 139]. The only other laser-plasma source with similar properties is the flying mirror [140, 141] which is essentially based on the same principles as the ROM only that the reflecting electron sheet travels toward the laser source at constant velocity instead of oscillating.

In this chapter two experiments aiming at characterizing the temporal structure of the surface-harmonic emission will be presented addressing the integral question of temporal coherence and phase locking of the emitted radiation. Both experiments where conducted at the MPQ where a special experimental setup has been devised to allow the accumulation of many laser shots from a large-area target which is essential for temporal characterization experiments.

In a first section I will present results of a second-order autocorrelation (AC) measurement of a train of harmonics which shows, for the first time, that the harmonic radiation is indeed emitted as a train of as-pulses [63]. This work is also presented in detail in the thesis of my colleague Y. Nomura [69] but as it was a collaborative effort that has consumed a large portion of my PhD-work it shall also be presented here. The results also allow interesting comparisons with the data obtained in the temporal coherence measurements.

The coherence measurements are completely new, i.e. they have not been published before, and will be presented in the second experimental section of this chapter. The measurements follow a method first introduced for gas harmonics by D. Hemmers et al.

[142] and allows the determination of the coherence time of the individual harmonics. In addition the method can be used, for example, to measure the complex index of refraction of materials [142]. While the temporal coherence measurement, by nature, cannot be used to unambiguously determine the pulse duration of an unknown source the results are still very informative especially when compared to those of the AC. In this case differences in coherence time and deduced pulse duration give indirect information on the phase properties of the harmonics and allow conclusions about the dynamics of the harmonic generation mechanism.

4.1 Experimental Setup

Before the results are presented a short overview of the experimental setup and the facilities available at MPQ shall be given. The SHHG experiment is set up in one of four target chambers each one of which is dedicated to one particular experiment. The individual chambers are all connected to a sophisticated motorized beamline system which allows, in principle, the delivery of either ATLAS or LWS10 to any target chamber. In practice, however, the SHHG chamber is currently equipped with dielectric mirrors which only allow the use of ATLAS as their reflectivity is not broad-band enough to support LWS10. To alleviate this problem an upgrade of the beamline is currently under way the main objective of which is to exchange the mirrors for more broad-band silver-coated ones and allow the operation of two experiments in different chambers in parallel to maximize the efficient use of the laser systems.

A photograph of the target chamber is shown in figure 4.1 (a). The laser beam enters the chamber from the top and is directed onto the 30° off-axis, dielectrically coated focusing parabola via two plane mirrors. The 4 inch focusing mirror has an effective focal length of 160.8 mm corresponding to F/2.3 for the 70 mm diameter ATLAS beam. The parabola is positioned such that the focus is located at the geometrical center of the octagonally shaped target chamber to allow best possible access to the interaction region from the various side ports. The target is positioned in the focus of the laser under an angle of 45° resulting in a specularly reflected harmonic beam in a plane parallel to the chamber floor. This geometry ensures that the mirrors for steering the incident laser beam do not interfere with optical components used to manipulate the XUV beam. A detailed CAD drawing of the beam geometry around the focus and of the target mechanism is shown in figure 4.1 (b).

The target mechanism was specially designed for the needs of multi-shot temporal characterization experiments as it can accommodate large 120 mm disk targets allowing the accumulation of up to 2000 laser shots. To provide a fresh target spot for every shot

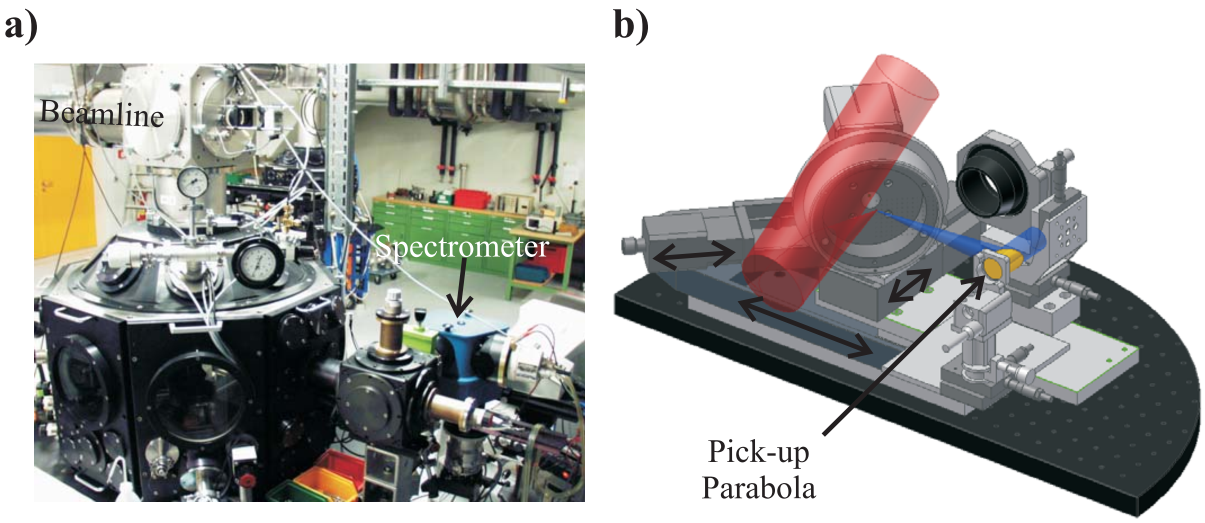

Figure 4.1: (a) Photograph of the MPQ target chamber. The ATLAS beam enters the chamber from the top and is focused to the geometrical center of the vacuum vessel using an F/2.3, 30° off-axis parabola. In this photograph the chamber is equipped with the ACTON spectrometer (blue box) and a gold focusing mirror (inside the black cube). The configuration is comparable to the one in 6.1 (b). The CAD drawing in (b) shows the details of the target mechanism inside the chamber. The 120 mm disc target is movable in three dimensions (rotation, translation along the target surface and translation in focal direction). An additional translation stage can be used to move the target out of the laser beam and allow characterization of the laser focus. The small gold parabola was used to recollimate the harmonic beam for the AC-measurements and can be flipped down for the characterization of the XUV-spectrum.

at 10 Hz repetition rate the target can be rotated and translated parallel to the target surface with two computer controlled stepper-motor stages. In addition a third stage allows translation of the mechanism in the focal direction to optimize the laser intensity on the target. Finally the mechanism is mounted together with an F/2 achromatic objective on another large translation stage. The stage is long enough to completely retract the target from the beam and allow the characterization of the laser focus with the objective. Details on the focal spot characterization can be found in section 3.1.2.

After generation on the target the XUV beam is then either diagnosed with an XUV spectrometer attached to the outside of the target chamber using the same geometries as the ones shown in figure 6.1 (b) and (c) or directed to an experiment using a suitable bending mirror. Figure 4.1 (b) shows the small recollimating parabola used in the autocorrelation experiments. It is mounted on a flipper stage to allow easy removal from the beam for measurements of the harmonic spectrum (see also figure 4.2). The details of the setups of the two experiments presented here will be described in the respective subsections.

4.2 Methods for Temporal Characterization

As has been mentioned before two experiments designed to investigate the temporal characteristics of surface harmonics shall be presented in the following: One on the XUV-autocorrelation of a train of harmonics and one addressing the temporal coherence of surface harmonics. Owing to the fact that the approaches used are very different the experiments will be presented in two different subsections, however the interpretation and the discussion especially of the coherence measurement profits greatly from the comparison of the results obtained with the two different methods.

4.2.1 The XUV Autocorrelation

First an overview of the nonlinear XUV autocorrelation experiment shall be given. While the autocorrelation is a well known and widely used temporal characterization technique in the visible wavelength range its application to XUV radiation remains very difficult and has only been successfully implemented in experiments with gas harmonics so far [143, 144]. The key problem is to find a medium that exhibits a nonlinear response in the desired wavelength range. For visible light this can be achieved with nonlinear crystals [101] but in the XUV a different detector is needed. The measurements presented here rely on the non-resonant two-photon ionization of Helium [145] as the nonlinear detector. Owing to the large ionization potential of He of 24.6 eV this is suitable for harmonics 8 to 15 of the fundamental laser wavelength. The energy of these photons is low enough to prevent single-photon ionization but high enough to ensure that any combination of two photons can produce He^+.

The setup of the XUV volume-AC used in the experiment is shown in figure 4.2 and is very similar to the one used in [143]. The spectral selection is achieved using an Indium filter to reject all harmonics below H8 and the CWE-cutoff of a PMMA (Polymethylmetacrylate) target to prevent the generation of harmonics higher that H14 (owing to the limited contrast of the ATLAS laser no ROM harmonics were generated). Additionally the recollimated beam from the target is reflected off a fused silica wedge under an angle of 57° to suppress residual IR-radiation as this is the Brewster-angle [74] for the fundamental laser wavelength. Note that this method has also been used before in the context of harmonics from gaseous media [146]. The filtered beam is then reflected under an angle of 8° off a split spherical gold mirror and focused into a helium gas jet. The ions generated in the jet are detected using an multi-channel plate (MCP) attached to a time-of-flight spectrometer. The split mirror serves two purposes in this setup. For one

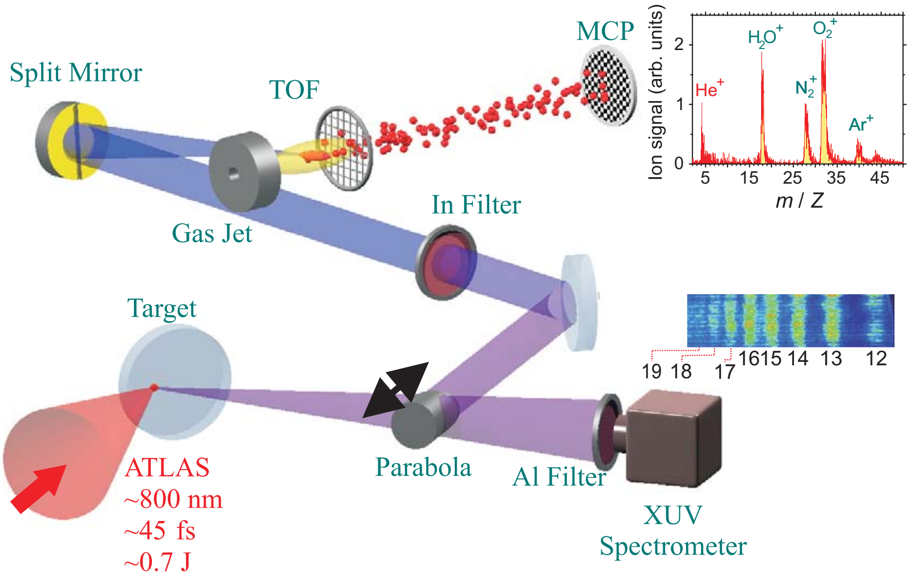

Figure 4.2: Setup of the XUV-autocorrelator. The harmonics from the target is recollimated using a 1 inch, gold coated, 90° off-axis parabola. The beam is reflected under 57° AOI (Brewster angle for the fundamental) off a fused silica wedge to suppress the residual IR and then spectrally filtered using a 150 nm Indium filter selecting only harmonics 8 and up. The selected harmonics are then focused, using a split 150 mm focal length gold mirror acting as a wave-front divider, into a helium gas-jet. The resulting ion spectra are recorded using a time-of-flight spectrometer. Typical mass- and harmonic-spectra are shown in the insets.

it acts as a fully reflective beam-splitter and simultaneously one half can be delayed with respect to the other using a piezo-driven translation stage to introduce a delay between the two halves of the beam. Depending on the delay the focused intensity in the jet is varied resulting in a variation of the 2-photon-generated He^+-ion yield and thus allowing the extraction of a second-order AC-trace.

However, before an AC-measurement can be conducted it is of utmost importance to confirm that the ionization in the gas jet is indeed dominated by the 2-photon process and thus suitable for AC. To study this the dependence of the yield of various ion species has been recorded as a function of the XUV-intensity for a fixed setting of the split mirror. Note that the O_2^+-signal, which is known to be generated via single-photon ionization in the photon energy range used (ionization potential 12.1 eV [147]), is used as a measure of the XUV-intensity as this is more precise than scaling the graph with the driving laser intensity. Figure 4.3 shows the result of this measurement for (a) and (b) a low-density PMMA target with a CWE-cutoff at harmonic 14 and a high-density fused silica target

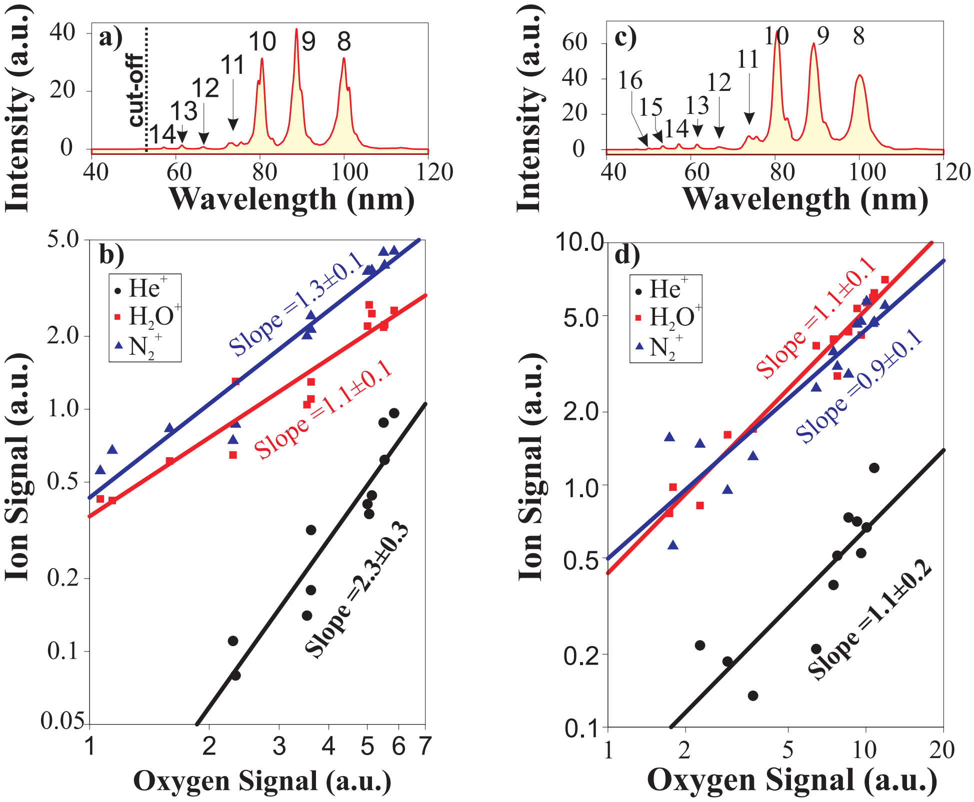

Figure 4.3: Harmonic spectra after the In-filter and dependence and ion yield dependence on XUV-intensity for (a) and (b) a low-density PMMA and (c) and (d) a high density fused silica target. The low density target displays a clear cutoff at H14 while the spectrum from fused silica extends beyond this point. The ion yields of He$^+$ and several components of the residual background gas are plotted against the O_2^+-ion yield. In this case a slope of one indicates single-photon ionization while a slope of two is evidence of two-photon ionization.

with a cutoff at H20. For comparison the harmonic spectra after the In filter are shown in panels (a) and (c). Note that weak but clearly visible harmonics beyond the 15^{th} order can be observed in the case of the high-density target while the PMMA target displays a sharp cutoff at harmonic 14. Despite this seemingly small difference in the XUV-spectra a very obvious difference is visible in the intensity dependence of the He$^+$ ion-yield in the two cases. While the measurement with the PMMA target and thus the sharp cutoff in the spectrum (figure 4.3 (b)) clearly displays an intensity dependence with a slope of close to 2 for He$^+$ in the log-log-plot indicating 2-photon ionization the high density target (figure 4.3 (d)) results in a slope of approximately one indicating that the residual 16^{th} harmonic contained in the spectrum in this case is sufficient to dominate the ionization dynamics leading to mainly single-photon ionization. In fact, this is not very surprising as the cross-section for single-photon ionization of He is roughly four orders of magnitude higher than that for the 2-photon process. For comparison the intensity dependence of the ionization of two background gases is also shown in figure 4.3. For both H_2O^+ and N_2^+ a slope of one is detected for both targets as one would expect from the respective ionization potentials of 12.6 eV and 15.6 eV [147] which are both significantly lower than the energy of the highest harmonic in the spectral composition.

The measurements indicate how crucial proper spectral filtering especially at the high-energy end of the harmonic composition used for the autocorrelation is for the success of the experiment as only a 2-photon process as detector will allow the measurement of the duration of the XUV emission. We have therefore chosen to conduct the AC-measurement with low-density PMMA targets to take advantage of the spectral cutoff despite the less favorable material properties (lower damage threshold, bigger problems with target contamination and thus faster decay of the harmonic signal [69, 70]) as compared to the more robust fused silica targets.

The temporal characterization of the harmonic train synthesized using the In filter and the PMMA target was conducted in two steps. In a first measurement a rough scan was conducted to determine the overall duration of the harmonic emission and find the best overlap between the two replica of the beam before, in a second step, a fine scan was recorded to look for sub-cycle bunching and therefore as-pulses in the harmonic emission.

For the coarse scan a delay step-size of 3.3 fs was chosen and 20 mass-spectra where recorded and averaged for each delay tstep. The AC-trace resulting from this scan is shown in the top plot of figure 4.4. Note that the observed contrast of approximately 1.5:1 is to be expected as the maximum contrast expected from a volume-AC is 2:1 and not 3:1 as for a collinear intensity-AC [148] and aberrations introduced in the XUV beam-path will lead to further contrast reductions [63, 69]. For comparison the H_2O^+-signal known to originate from single-photon ionization is also shown in the plot and, as expected, does not show any variation with delay except for a small decay toward later times which can be attributed to degradation of the target during the measurement. For the interpretation of the data it is important note that the raw data has been smoothed using a running average over 9 adjacent data points to reduce fluctuations in the plot. This has to be taken into account when extracting the pulse duration from the measured trace as the smoothing will broaden the plotted trace. The pulse duration has therefore been extracted in a first step by fitting a Gaussian to the raw data yielding an overall duration of the XUV-burst of 44±20 fs where the large uncertainty is a result of the fluctuations in the raw signal. For comparison the fit is also shown as a green dashed line in figure 4.4. It is also possible to extract the duration of the pulse from the smoothed data by unfolding the width of the smoothing function from the result of the (much improved) fit to the smoothed data. Albeit more indirect, this yields a result with a smaller error of 47±4 fs

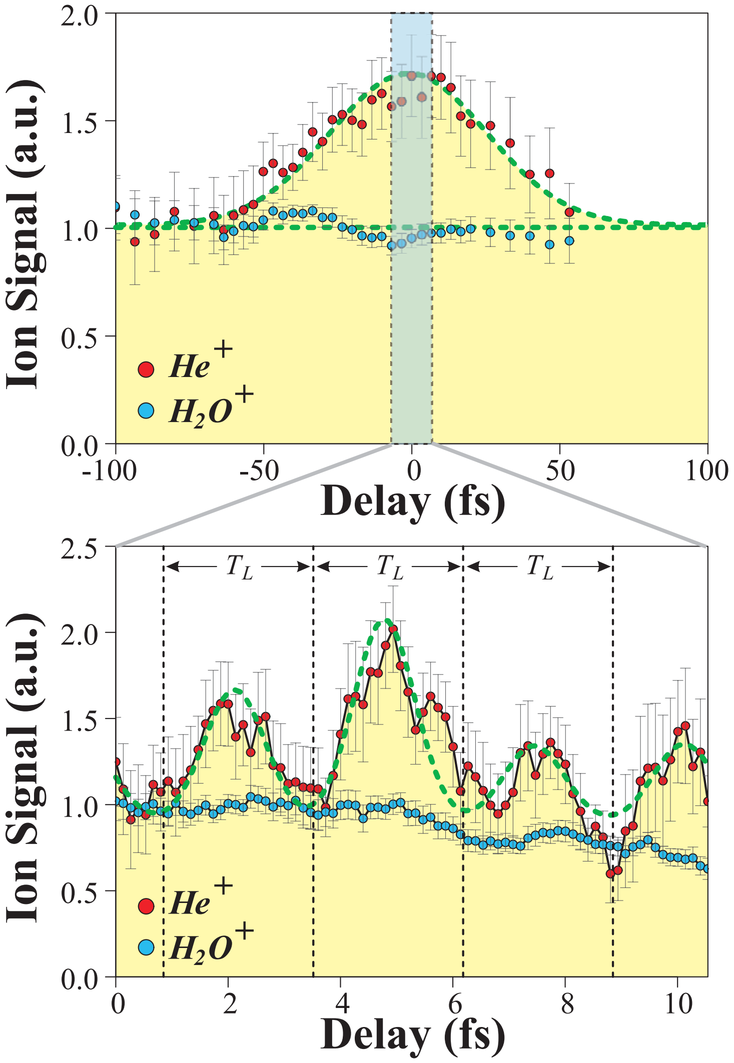

Figure 4.4: Coarse and fine second-order volume autocorrelation of a train of as-pulse composed of harmonics 8 to 14. The AC-traces are obtained from the He$^+$ signal measured as a function of the delay between the beams reflected from the two parts of the split mirror. Each data point is the result of averaging over 20 individual shots. The delay step size was chosen to be 3.3 fs in the coarse scan and 133 as in the fine scan. To visualize the trend clearly the running average over 9 delay points was taken. For comparison and extraction of the pulse duration a gaussian fit to the raw data is also shown (dashed green line). The single-photon H_2O^+ signal is given for comparison.

which is in good agreement with the duration extracted from the raw data. The fact that this value is very close to the duration of the ATLAS laser pulse indicates that the CWE mechanism is indeed a nearly linear process which is in agreement with previous findings [34].

To study the sub-cycle structure of the harmonic emission a fine scan was conducted with a very high temporal resolution of 133 as corresponding to 20 steps per driver laser cycle over a total range of 4 laser cycles around the point of best overlap. The data was treated in the same way as in the coarse scan and the result of the measurement is shown in the lower panel of figure 4.4. A periodic structure with a spacing of one fundamental laser cycle is clearly visible proving that the harmonics are indeed emitted as a train of as-pulses. Note that, in contrast to gas harmonics [143], the periodicity of one as-pulse per cycle is expected as the harmonic spectrum contains all harmonic orders and not only the odd ones in the case of surface harmonics. Again, by fitting a train of gaussians to the raw data, it is possible to estimate the duration of the individual as-pulses yielding a duration of 0.9±0.4 fs. Despite the uncertainty of this estimate it allows interesting conclusions about the harmonic generation process. Purely from the harmonic spectrum one would expect a significantly shorter as-pulse duration of approximately 450 as. However, in section 2.2.2 a simple model for the atto-chirp expected as a result of the generation of the CWE-harmonics in a density gradient is derived and a series of as-pulse trains for pre-plasmas of various scale-length are plotted in figure 2.6. Interestingly the durations deduced from the model for a harmonic spectrum very similar to the one used in the experiment are close to the measured 900 as for a wide range of scale-lengths. In fact, even though the pre-plasma scale-length has not been measured in our experiment, it most likely lies inside the window between 0.05 and 0.25 λ used for the model calculations. Therefore, while the precision of the AC is not high enough to definely prove the relation the observed as-pulse duration is most likely the result of the chirped emission of the individual harmonics from a density gradient.

The result of the fine scan shows, for the first time, that the harmonics emitted from solid targets are indeed phase-locked as predicted by theory. This proves that surface harmonics have the potential to serve as a source of as-pulses overcoming the fundamental intensity limit imposed on harmonic generation from noble gases [29] and paving the way for a wealth of new experiments [19–22]. However, while the method of XUV-autocorrelation was successfully implemented in this experiment it is limited to a fixed range of harmonics. To exploit and characterize the full potential of surface harmonics new methods based either on alternative 2-photon transitions [144, 149, 150] or for example the streak camera [10, 151, 152] method for temporal characterization will need to be investigated in the context of harmonics from solid targets to improve temporal resolution and study even shorter as-pulses.

4.2.2 Temporal Coherence Measurements

Compared to the nonlinear autocorrelation the experimental realization of a temporal coherence measurement is very simple as it essentially is a first-order autocorrelation

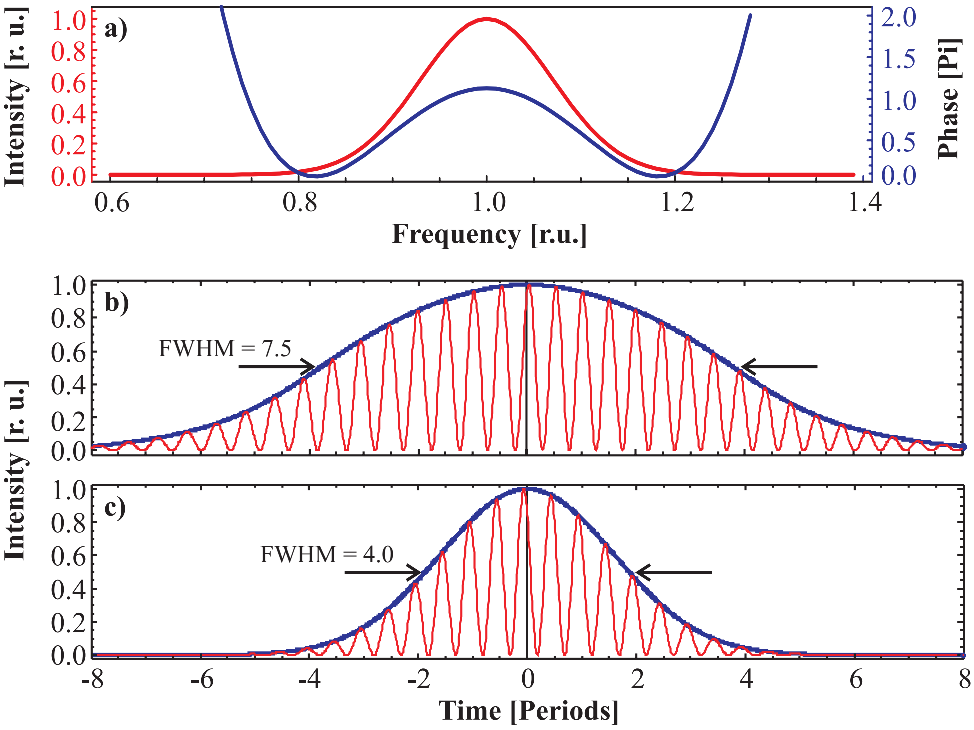

Figure 4.5: Illustration of the influence of the spectral phase of a model pulse on its duration. (a) Shows the power spectrum (red) and spectral phase (blue) of the model pulse. Fourier transforming the spectrum including the phase results in a chirped pulse of roughly 7.5 periods duration (b) while a transform without the phase yields 4 periods (c). This explains why the pulse duration measured via cross-correlation is different from the one obtained via second-order autocorrelation (see text).

and therefore does not require a nonlinear medium. The drawback of this is that the temporal coherence measurement does not return the real pulse duration of the XUV-burst but rather the duration expected under the assumption that the phase across the individual harmonics is flat, i.e. the minimum possible duration associated with a given power spectrum. Therefore the method will underestimate the real pulse duration in the case of a chirped harmonic beam. Figure 4.5 illustrates this by comparing the temporal structure of a pulse with the spectral intensity and phase shown in (a) when the phase is taken into account (b) or set to zero (c). From the comparison one can clearly see that different pulse durations will be deduced from a second-order autocorrelation (assuming a reasonable pulse shape) and a temporal-coherence measurement in the case of a chirped pulse. In return, however, this means that from the comparison of a nonlinear AC with a coherence measurement information about the harmonic chirp can be obtained.

In the context of the experiment presented here it is important to note that, in principle, the results obtained with a temporal coherence measurement can also be deduced

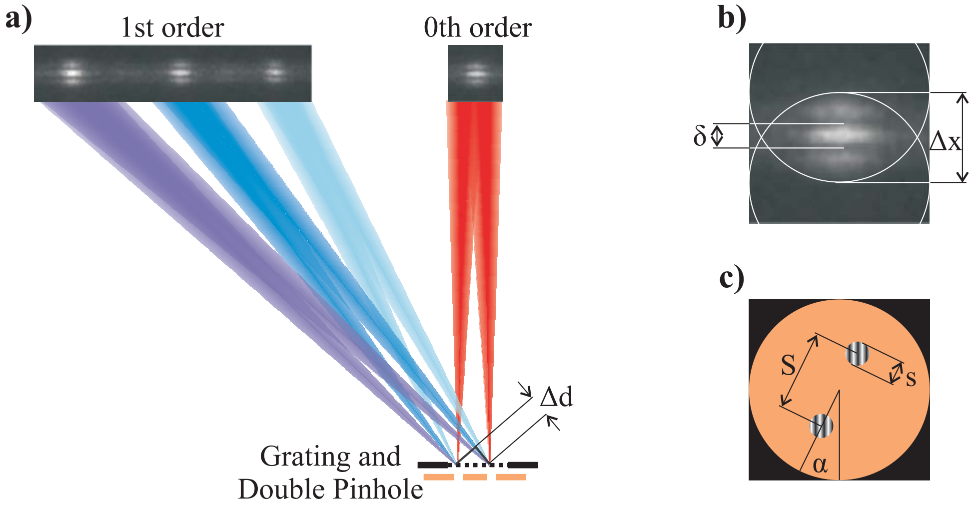

Figure 4.6: Setup of the modified transmission spectrometer used for the measurement of the temporal coherence of CWE-harmonics. (a) Top-view of the setup showing the double pinhole in front of the transmission grating. The divergent harmonic beams emanating from the pinholes are diffracted into the various orders and interfere in the plane of the detector. The time delay between the two beams Δd can be varied by rotating the double pinhole with respect to the grating lines. (b) Large view of a typical interference pattern recorded with zero delay. The white circles indicate the footprints of the beams emanating from the individual pinholes. Their separation is Δx and the resulting fringe spacing in the interference region is labeled δ. (c) Front view of the double pin-hole with labels on the important dimensions.

directly from a high-precision spectral measurement. If the line shape of the individual harmonics is measured very accurately the coherence time can be deduced directly from it. In practice, however, such high-precision measurements are very difficult as they require unfolding several parameters from the spectrum. Especially the alignment of the imaging system inside the spectrometer is almost impossible to characterize precisely. On the other hand the coherence measurement is not difficult to perform as it can be implemented with a conventional transmission spectrometer and delivers more reliable results. To underline this a comparison of the two methods will be given at the end of this section.

The concept of the measurement follows the method introduced by D. Hemmers et al. [142] for the investigation of gas harmonics with some adaptations of the setup to the special requirements of a surface harmonic experiment. It is based on a conventional non-imaging transmission spectrometer in which the entrance slit has been replaced by a pair of pinholes mounted such that they can be rotated with respect to the orientation of the grating lines (a more detailed description of the spectrometer can be found Appendix B.4). The double-pinhole serves two purposes in the experiment: It acts as a beam splitter by selecting two narrow beams from the harmonic emission cone and simultaneously introduces a delay between the them in the first diffraction-order of the spectrometer. The delay can be adjusted by rotating the pinholes and can be calculated using equation B.4. Figure 4.6 (a) shows a top-view of the setup from which one can intuitively understand the origin of the delay when the axis connecting the two pinholes is not aligned to the grating lines. (b) and (c) show an image of a typical interference pattern and a front-view of the double pinhole on which all relevant dimensions are labeled.

For the success of the experiment it is of great importance to choose the optimal dimensions s and S for the two pinholes. The separation of the two pinholes determines the maximum delay that can be introduced between the two replica of the beam and has to be determined depending on the expected range of coherence times. It should be chosen big enough to completely separate the two signals in time but not larger than necessary as this would decrease the resolution and make overlapping the beams emanating from the two sources more difficult. In a second step the size of the individual holes needs to be determined. The choice is strongly influenced by the selected pinhole separation and will always be a trade-off. On the one hand the opening has to be small enough such that the diffraction of the harmonics of interest is large enough to allow significant overlap of the two beams on the detector but on the other hand the openings should not be smaller than necessary for maximum possible harmonic transmission. As a result of this consideration we have chosen a separation of S=100 μm and a hole diameter s=60 μm for our experiment.

Figure 4.7 (a) shows a series of images recorded with a CsI-coated MCP-detector in the first diffraction order of the transmission spectrometer for different angles of the pinholes (and thus different temporal delay), where an angle of 0° corresponds to zero delay while 90° is equivalent to the maximum delay of $\Delta t_{\mathrm{q,max}} = 120\lambda_{\mathrm{q}}/c$ where q denotes the harmonic order and λ_{q} is the corresponding wavelength. From the images one can clearly see the decrease in fringe visibility for all harmonic orders with an increase in the delay as one would expect. To quantify this effect it is necessary to determine the fringe visibility $\mathcal{V}$ as a function of delay Δd for all harmonics and deduce the coherence length, i.e. the delay l_{c} for which

$$2\mathcal{V}(\Delta d = l_{\mathrm{c}}) = \mathcal{V}(\Delta d = 0) \tag{4.1}$$

and which is related to the coherence time t_{c} through the simple relation $t_{\mathrm{c}} = l_{\mathrm{c}}/c$. The visibility or modulation depth is a function of the maximum and minimum intensity I_{max} and I_{min} in the interference pattern and is defined as

$$\mathcal{V} = \frac{I_{\mathrm{max}} - I_{\mathrm{min}}}{I_{\mathrm{max}} + I_{\mathrm{min}}}. \tag{4.2}$$

Considering that the present problem is essentially one dimensional and the raw images obtained with the detector can be reduced to lineouts by binning in the direction perpendicular to the fringe pattern one can follow the derivation in [153] to determine the visibility using the interference equation for partially coherent light given therein:

$$I^{(q)}(x, \Delta d) = I_1^{(q)} + I_2^{(q)} + 2\sqrt{I_1^{(q)} I_2^{(q)}}\, |g_{12}(\Delta d)| \cos\left(\frac{2\pi}{\delta^{(q)}} x\right), \tag{4.3}$$

where the upper case (q) denotes the harmonic number, $I_1^{(q)}$ and $I_2^{(q)}$ are the intensity distributions of the individual beams on the detector, $|g_{12}(\Delta d)|$ is the absolute value of the normalized cross-correlation function (see [153]), $\delta^{(q)}$ denotes the fringe spacing for the respective harmonic and $I^{(q)}(x, \Delta d)$ is the resulting interference pattern. Inserting equation 4.3 into equation 4.2 one can rewrite the visibility as a function of delay in the new form

$$\mathcal{V} = \frac{2\sqrt{I_1 I_2}}{I_1 + I_2}\, |g_{12}(\Delta d)| \tag{4.4}$$

and reduce this in the special case when $I_1 = I_2$ to

$$\mathcal{V} = |g_{12}(\Delta d)| \,. \tag{4.5}$$

To fit the lineouts extracted from the raw data with equation 4.4 it is necessary to determine $I_1^{(q)}$, $I_2^{(q)}$ and $y^{(q)}$ from the geometry of the experiment. Assuming that the pinholes are evenly illuminated the light emanating from them will form an Airy-pattern on the detector. The radius of the Airy-disc of the qth harmonic $r_{\mathrm{A}}^{(q)}$ is given by $r_{\mathrm{A}}^{(q)} = 1.22\,\lambda L_{\mathrm{GD}}/s$ where L_{GD} denotes the distance from the grating to the detector. For the sake of simplicity and owing to the fact that only the central maximum of the Airy-pattern contributes significantly to the measured interference pattern the central Airy disc is approximated with a Gaussian of $1/\mathrm{e}^2$-radius $w^{(q)} = 0.687\, r_{\mathrm{A}}^{(q)}$ corresponding to $w^{(q)} = 6.55/q\ [mm]$ for the experimental geometry used. The intensity distributions $I_1^{(q)}$ and $I_2^{(q)}$ can therefore be written in the form

$$I_i^{(q)} = I_{i0}^{(q)} \exp\left[-2\left(\frac{x \pm \Delta x/2}{w^{(q)}}\right)\right]. \tag{4.6}$$

Δx (see figure 4.6 (b)) describes the distance between the maxima of the two individual Gaussians and can be determined from the geometry of the experiment using the relation $\Delta x = S(1 + L_{\mathrm{GD}}/L_{\mathrm{TG}})$, where $L_{\mathrm{GD}}$and L_{TG} are the distance grating to the detector and from the target to the grating respectively. Finally the last parameter $y^{(q)}$, the fringe spacing in the interference pattern, needs to be determined. It is given, in the limit of small angles which is well fulfilled in this experiment, by $y^{(q)} = \lambda^{(q)}/\beta$ where β is the angle under which the wave-fronts emanating from the double-pinhole intersect at the detector. The angle can be determined from the geometry of the experiment and is given

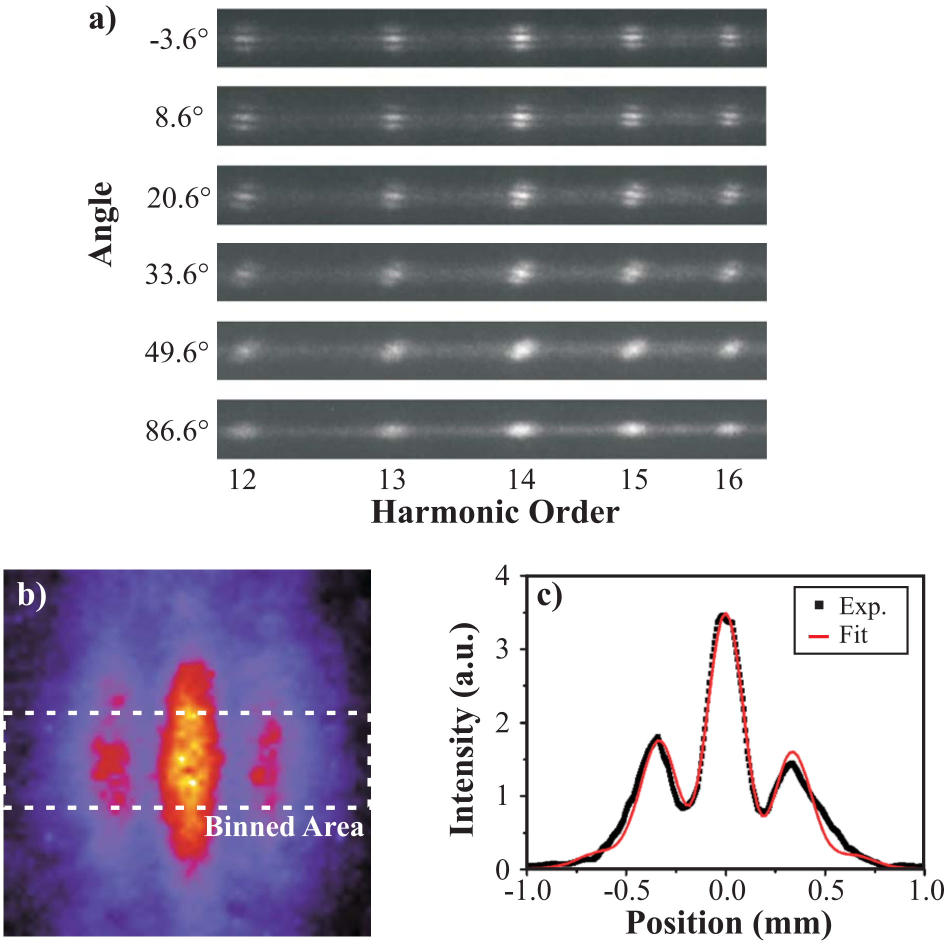

Figure 4.7: Typical interference patterns recorded with the MCP-detector in the spectrometer for different pinhole angles α (corresponding to different time delays between the interfering beams). For each image 400 laser shots where accumulated. For analysis the individual interference patterns are extracted from the image (b) and binned (c). To extract the fringe visibility a fit with the necessary free parameters is conducted (see text).

by $\beta = S/L_{\mathrm{TG}}$ (note that the effect of the slight difference in AOI onto the grating of the rays originating from the two pinholes can be neglected as its contribution to β is negligible).

Using equation 4.6 and the derived fringe spacing it is now possible to fit equation 4.3 to the interference patterns extracted from the raw images of each individual harmonic at each delay step. In the procedure the factors $w^{(q)}$,Δx and $y^{(q)}$ are determined from the experimental geometry and fixed while the best fit for $I_{10}^{(q)}$, $I_{20}^{(q)}$ and $|g_{12}(\Delta d)|$ is determined. For the 13^{th} harmonic at an angle of 3.4° the result of this fit is shown in figure 4.7 (c). Owing to the fact that the intensities of the two Gaussians are generally found to be very similar the simpler equation 4.5 is used to determine the visibility from each fit. The result of this evaluation is shown in figure 4.8 (a), where each black point in the plots is the result of the fit to one interference pattern. The error bars correspond to the error of the fit owing mainly to small differences between the two intensities $I_{10}^{(q)}$ and $I_{20}^{(q)}$. To determine the coherence times of the individual harmonics using the criterion given in equation 4.1 the extracted visibilities are fitted with Gaussians which are also shown in each plot of figure 4.8 (a). Finally the FWHM of each fit is determined and the coherence time is deduced. The results of these evaluations for harmonics 12 to 16 are shown in figure 4.8 (b).

From the measurement it is immediately obvious that the coherence time of the individual harmonics is significantly shorter than the duration of the driving laser pulse. More notably, however it is also significantly different from the XUV-pulse duration determined using the second-order AC (figure 4.4). In addition, unlike the AC where the harmonic composition was diagnosed, the spectrally resolved measurement in this experiment allows the wavelength dependent analysis of the temporal characteristics of the XUV-radiation. This reveals an almost constant coherence time for all analyzed harmonics with a slight tendency toward shorter coherence for higher harmonics. It is important to note however that this trend lies well within the error bars of the measurement for harmonics 13 to 16 making an analysis of this effect very difficult.

To analyze and interpret the discrepancy between the overall length of the XUV-emission deduced from the AC and the coherence measurement it is important to understand that the main difference between a second-order AC and a coherence measurement lies in the way in which chirp influences the results of the experiments. While the AC is capable of finding the real pulse duration of both the envelope as well as the individual as-pulses including the effects of chirp the coherence analysis only yields the fourier-limited duration supported by the generated harmonic power spectrum (see figure 4.5), i.e. the pulse duration of the emission envelope under the assumption of a flat phase. In fact, owing to the spectrally resolved measurement of the coherence time, no direct information about the individual as-pulses can be deduced from this measurement. The discrepancy (within the experimental errors) in the results of the two measurements therefore proves that each individual harmonic in the emitted spectrum is indeed chirped as expected for CWE. While chirping of the CWE-harmonic spectrum has also been identified as the source of the broadening of each individual as-pulse in the fine AC-measurement it is important to emphasize that it is a different kind of chirp that has the main contribution to the decrease in harmonic coherence and is therefore probed here (as the coherence measurement does not yield direct information about the individual as-pulses). While the broadening of the as-pulses originates from the fact that the individual harmonics are generated at different depths inside the pre-plasma gradient which results in a smooth

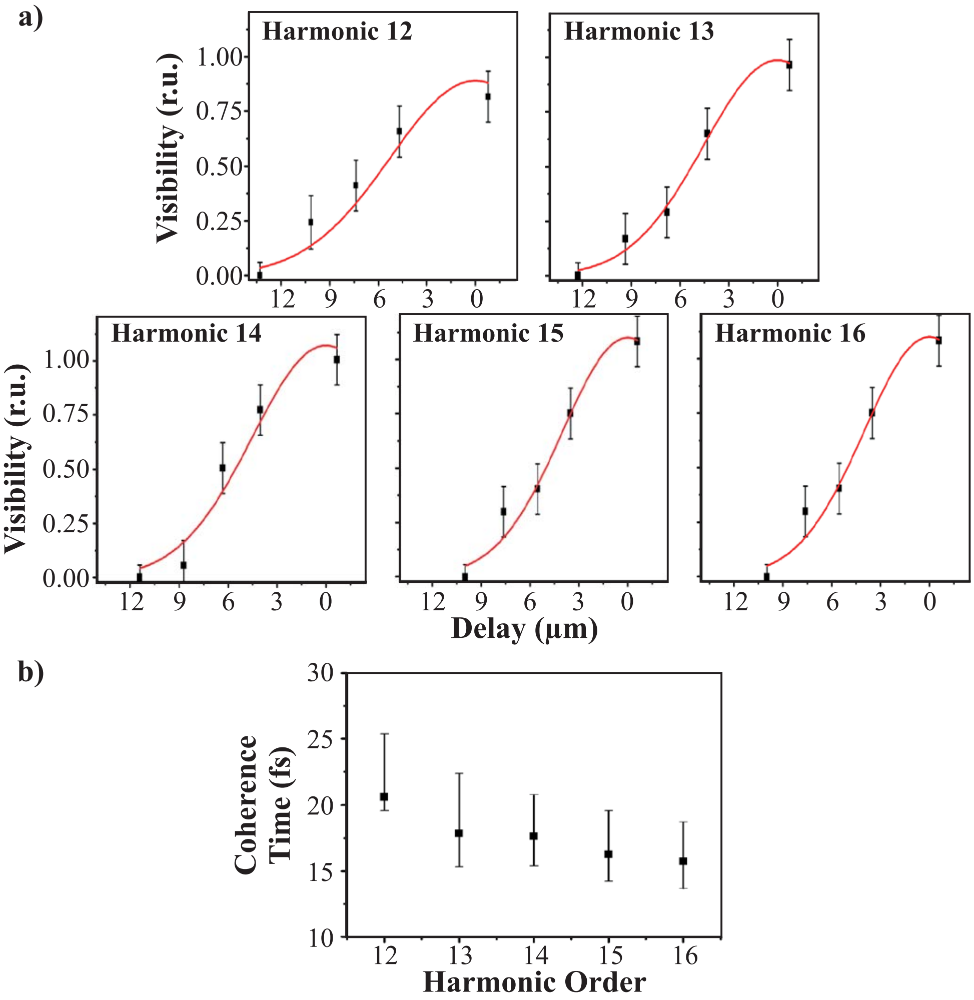

Figure 4.8: (a) Plots of the fringe visibility as a function of delay between the beams emanating from the two pinholes. The coherence time is deduced by fitting a Gaussian to the data points for each individual harmonic. The resulting coherence times as a function of harmonic order are shown in (b).

variation of the phase across the whole CWE-spectrum, the decrease in coherence time is mainly caused by rapid phase modulations across individual harmonics. These are expected to be the result of the unequally spaced emission of the individual as-pulses within the pulse train resulting from the indirect generation of the harmonics via Brunel-electrons (Section 2.2.2 [34]).

To determine whether the coherence time deduced from the measurement presented here can indeed be explained by unequal spacing of harmonic emission model calculations have been conducted in which an unequally spaced train of as-pulses was fourier-transformed to determine the expected harmonic spectrum under these conditions. To find a realistic model for the spacing this was extracted from a PIC-simulation and introduced into the model calculation. For a more detailed discussion of the model calculations see chapter 6 and references [62, 67]. From the resulting harmonic spectrum recovered for a 40 fs pulse with intensities similar to those used in this experiment the harmonic width was extracted for comparison with the coherence measurements presented here. For the harmonic 13 the model returns a spectral bandwidth of $\Delta\omega/\omega = 0.15 \pm 0.05$ (compared to $\Delta\omega/\omega = 0.04$ expected for an equally spaced train of the same duration). This finding is in good agreement with the value of $\Delta\omega/\omega = 0.10 \pm 0.03$ (corresponding to a coherence time of 17.5±2.5 fs) deduced from the experiment suggesting that the unequal spacing is indeed the origin of the discrepancy between coherence time and the overall duration of the generated XUV burst. The model calculation may also hint at the origin of the decreasing coherence time at higher harmonics. When an atto-chirp, i.e. a chirp as a result of harmonic generation in a gradient, is introduced in the model slight broadening of the higher harmonics is observed. This is the result of the fact that the phase variation is stronger for higher harmonics than for lower ones in a linear pre-plasma ramp (see equation 2.32). However, while this is a possible explanation the data presented here is not precise enough to draw any final conclusions in this respect. For this purpose further higher precision measurements and more refined calculations are necessary.

Having discussed the results of the coherence measurement and compared it with the model it is interesting to revisit the discussion about the necessity of such a measurement as the coherence time can, in principle, also be deduced from a spectral measurement directly. For this purpose it is interesting to analyze some typical spectra obtained with the McPherson spectrometer. Even though great care was taken to align the spectrometer correctly and the entrance slit was narrowed to prevent line-broadening owing to a large entrance aperture typical line-width derived from such measurements are $\Delta\omega/\omega = 0.25 \pm 0.05$ and thus more than two times larger than the value derived from the coherence measurement (typical spectra are shown for example in figures 4.3 and 6.3 (b)). More importantly however the value deduced from the spectral measurement does not match the model calculations nearly as well as the coherence measurement does.

In the future it will be very interesting to repeat the coherence measurement on harmonics generated via the ROM mechanism and compare the results obtained there to an autocorrelation as the phase of the relativistic harmonics is expected to be flat [30, 38]. Thus the coherence measurement should yield the same duration for the overall duration of the XUV-burst as the AC in that case. If, in addition, the AC shows transform-limited individual as-pulses the coherence measurement could then be used for temporal characterization in future as-beamlines envisioned for example on the ELI system [154] by measuring the coherence time of each individual harmonic and synthesizing the as-pulse with the phase known from the AC. If this is indeed the case it would be very simple to build an easy-to-use temporal diagnostic based on this method. In fact it would only require a retractable double pinhole in front of a transmission grating spectrometer which would most likely be integrated into such a beamline anyhow.

4.3 Summary

The results presented in this chapter constitute the first set of measurements addressing the temporal characteristics of harmonics generated from solid surfaces and thus investigate one of the most promising features of this new radiation source. The nonlinear XUV-AC proves, for the first time, that the harmonics emitted from solid targets are indeed phase-locked and emitted as a train of individual sub-fs pulses as predicted by theory [63, 69]. This finding is of utmost importance when such a source is to be employed in experiments requiring as-pulses of very high intensities. Furthermore a simple method for the determination of the temporal coherence of high harmonics is presented (see also [67]). It yields coherence times significantly shorter than the overall duration of the XUV-burst determined from the AC which is in good agreement with theoretical predictions suggesting that CWE should be emitted with unequal spacing between the individual as-pulses and thus be chirped.

The key to the XUV-AC is the choice of a suitable nonlinear medium and the filtering of the harmonic spectrum to the harmonic range matching this detector. In the measurement the two-photon ionization of He to He^+ was used for this purpose. The corresponding spectrum suitable for exciting the two-photon transition ranging from harmonics 8 to 14 was filtered from the emission of a PMMA target using an indium filter and a fused silica wedge for IR-suppression. A split spherical mirror was used to focus the beam into a helium gas jet and simultaneously introduce a time delay between the two parts of the XUV-beam. The measurement itself was conducted in two steps. First a rough scan of the delay spanning the whole length of the XUV-burst was used to characterize the envelope of the harmonic emission before a fine scan with very high resolution was conducted to prove the existence of individual pulses under the envelope. The resulting traces are shown in figure 4.4. From the measurement the pulse durations where extracted yielding a duration of 44±20 fs for the envelope and 0.9±0.4 fs for the individual pulses which is in good agreement with theoretical predictions in both cases.

To characterize the temporal coherence a conventional non-imaging transmission spectrometer was modified by replacing the entrance aperture with two pinholes mounted on a rotation stage. The dimensions of the pinholes are chosen such that the diffracting beams emanating from the two openings overlap and interfere in the detector plane. In the first diffraction-order of the transmission grating the time delay between the two beams was modified by rotating the two pinholes with respect to the orientation of the grating lines.

For each delay setting the interference pattern generated in the first diffraction-order was recorded for several harmonics and the fringe visibility for each interferogram was determined. From the decrease in fringe visibility with increasing delay the coherence time can be deduced. It is found to be 17.5±3 fs for harmonics 13 to 16 and thus significantly shorter than the overall XUV-pulse duration deduced from the AC. Model calculations reveal that the discrepancy can be explained by the chirping of the individual harmonics in the spectrum as a result of the unequally spaced emission if CWE-radiation. It is important to note that this method is very easy to use (perhaps even simpler that optimizing the alignment of a spectrometer to obtain reliable line-width measurements) and may well be used for day-to-day temporal characterization in future experiments especially if the prediction that the phase of ROM-harmonics is indeed flat holds true, as in that case the coherence measurement directly returns the overall emission duration of each individual harmonic and would thus also allow the reconstruction of the as-pulse duration.

Chapter 5

Harmonic Generation with High Contrast Pulses

In contrast to the previous chapter, where the experimental focus was on multi-shot experiments aiming at the temporal characterization of the generated CWE-harmonics, the experiments presented in this chapter aim at the generation of ROM harmonics and their characterization. All the measurements were conducted on the ASTRA laser facility [95] at the Rutherford-Appleton-Laboratory. To achieve the goal of generating relativistic harmonics a plasma mirror (PM) was inserted into the setup to significantly enhance the contrast of the laser pulse generating the high harmonics. This limited the number of shots that could be taken before changing targets severely but none the less the PM enabled a series of unique experiments studying in detail the interaction of ultra-high contrast 50 fs laser pulses with solid targets.

The results are presented in two sections. Section 5.2 focuses on the reflection of the fundamental and second harmonic generation at intensities around $10^{19}\ W\ cm^{-2}$ constituting the first demonstration of a high contrast plasma mirror (HCPM) at these intensities. Moreover it is shown that efficient spatial filtering and second harmonic generation from a plasma can be achieved at these intensities which may be of interest for the big laser systems envisioned for the future [154, 155] where the conventional filtering and conversion techniques are not applicable owing to damage issues [68].

The second set of measurements (section 5.3) exploits the properties of the high harmonics generated in our high contrast interaction. Amongst others the results demonstrate for the first time the generation of harmonics in the range of the relativistic cutoff for a 50 fs laser system, they show that the relativistic harmonics are emitted with constant divergence and demonstrate the influence of surface roughness on the harmonic generation process [64].

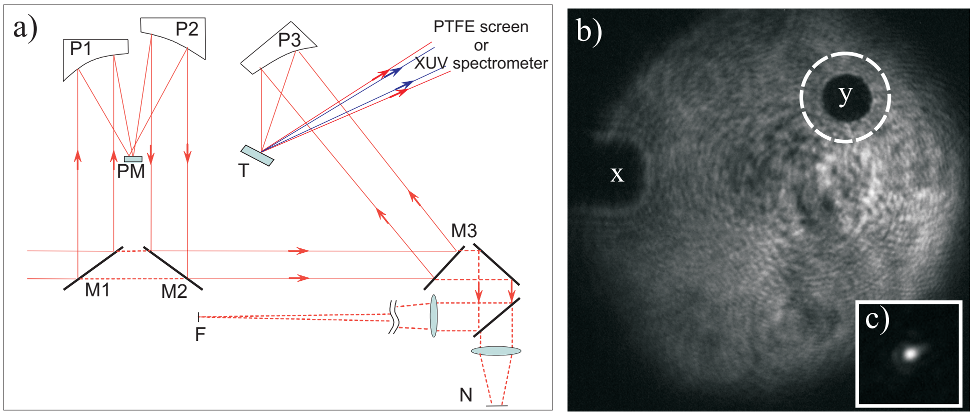

Figure 5.1: (a) Schematic drawing of the experimental setup. The laser beam incident from the left side of the plot is first focused onto the plasma mirror (PM) to enhance the laser contrast. Near- and far-field of the beam reflected off the PM are routinely monitored with cameras N and F. The beam is then focused onto a fused silica target using a third off-axis parabola P3. The emission from the target is studied using either an XUV spectrometer to look at high-order harmonics or a polytetraflouroethylene (PTFE) screen imaged with a CCD camera for measurement of low harmonics. (b) and (c) show typical images of the laser near-field and far-field obtained with cameras N and F.

5.1 Experimental Setup

The experiments presented in this chapter were conducted using the ASTRA laser at the Central Laser Facility (CLF) of the Rutherford-Appleton-Laboratory (RAL) in the UK. Astra delivers pulses with an energy of up to 800 mJ in 50 fs at a maximum repetition rate of 10 Hz to the target area. The peak-to-pedestal contrast is 1:10^7 500 fs before the peak of the pulse. Both the amplifier technology as well as the operating parameters are very similar to those of the ATLAS Upgrade laser at the MPQ described in chapter 3.1. More details on the ASTRA laser can be found in [95].

The setup of the experiments described here is shown in figure 5.1 (a). The beam from the compressor is incident from the left side of the sketch. The contrast of the incident laser beam is further improved from 1:10^7 to approximately 1:10^{10} using a conventional plasma mirror positioned in the near field of the beam focused with the off-axis parabola (OAP) P1 and operated at intensities around $5 \times 10^{15}\ W\ cm^{-2}$. For details on the operation of plasma mirrors see Appendix A. The high contrast pulse was then recollimated using a second OAP P2 identical to P1. To monitor the performance of the plasma mirror the near- and far-field of the reflected beam were routinely measured for every shot in the transmission of mirror M3 using cameras N and F. The main beam is focused under an angle of 30 degrees onto a fused silica target, T, using a 150 mm f/3 off-axis parabola P3 resulting in 3 μm radius near diffraction-limited focal spot with a spot-averaged intensity of approximately 2×10^{19} $W\ cm^{-2}$.

Typical images obtained with cameras N and F are shown in figure 5.1 (b) and (c). While (c) shows that the beam after the reflection off the PM is still nicely focusable, the near field image in (b) is more instructive. Two holes can be observed in the near-field beam profile (marked with (X) and (Y) respectively). While (X) can be disregarded because it is the result of clipping in the diagnostic system after mirror M3 (Y) is of key importance for the interpretation of the result in the following section. This dark spot in the beam originates from a hole in one of the ASTRA compressor mirrors the transmission through which is used for autocorrelation measurements of the laser pulse duration. In the next section we will show that, under certain conditions, the fundamental beam is spatially filtered in its interaction with the target leading to disappearance of this dark feature.

Two different diagnostics where used to characterize the emitted radiation from the target. For the observation of the fundamental and the second harmonic a polytetrafluoroethylene (PTFE) screen was placed in the specularly reflected beam from the target and imaged with a CCD-camera. Different color filters were used to distinguish the beam profile of the fundamental and the second harmonic. The higher harmonics discussed in section 5.3 were measured using a grazing incidence flat-field XUV-spectrometer and an Andor X-ray CCD. Details on the spectrometer are given in Appendix B.3.

5.2 The High Contrast Plasma Mirror

With the advent of increasingly intense ultra-short pulse laser systems [103, 154–156] tailoring and modifying laser beams becomes increasingly difficult. At intensities approaching the breakdown threshold for the bulk materials / crystals for example spatial filtering and second harmonic generation become a problem. Consequently, for very high intensity lasers, novel concepts that can withstand arbitrarily high intensities are necessary.

The reflection off an overcritically dense plasma is a promising candidate fulfilling these requirements. Since the reflection in this case does not depend on an optical coating but rather on the plasma density such a mirror can, in principle, withstand arbitrarily high intensities. In fact, higher intensities are actually beneficial as they lead to a more rapid ionization on the leading edge of the laser pulse.

While the plasma mirror is a well studied concept at moderate intensities around 5×10^{15} $W\ cm^{-2}$ [77–79, 157–161] the scalability of the process toward relativistic intensities has only been investigated in the context of high harmonic generation [57]. The question whether it can also be used for reflection of the fundamental laser beam and for frequency doubling at intensities up to $2 \times 10^{19}\ W\ cm^{-2}$ and is thus a candidate for application in next-generation ultra-high-power laser systems and it will be investigated in the following. These measurements also have implications for the investigation of high harmonics since a plasma surface capable of nicely reflecting the fundamental of the laser beam is an absolute prerequisite for the generation of near diffraction-limited harmonic beams.

5.2.1 Spatial Filtering at Relativistic Intensities

In this section experimental evidence of high quality reflection and significant spatial filtering of the fundamental laser beam at intensities up to $2.0 \pm 0.5 \times 10^{19}\ W\ cm^{-2}$ is shown. This high quality reflection, returning a highly focusable beam, is the key in determining whether a plasma optic is a useful tool for applications in this intensity range.

To study the reflection of the fundamental laser beam off the target under different conditions we conducted a series of measurements with different positions of the laser focus relative to the target surface, thus probing both the reflection in the near- as well as the far-field field of the laser.

When the front surface of the target is placed 200 μm in front of, or behind the best focus, the reflecting overdense plasma is formed in the near field of the incident focusing laser beam at an intensity of roughly $10^{17}\ W\ cm^{-2}$. The intensity, in this case, is roughly constant over the whole extension of the laser beam as a consequence of the flat-top beam profile that is common to all high-power lasers. Under these conditions all features of the incident beam are reproduced well in the reflected beam, as can be seen in Figures 5.2 (a) and 5.2 (c) and the red line out in Figure 5.2 (e). The edges of the beam profile remain steep and the hole in the beam originating from the laser compressor (see Figure 5.1) is well reproduced suggesting that the reflectivity of our HCPM is constant over the whole near-field beam diameter.

The fact that this observation holds true even for near-field reflections with intensities on the order of $10^{18}\ W\ cm^{-2}$ makes this the first observation of PM operation in the relativistic regime. It suggests that extremely high pulse contrast can indeed be achieved by cascading multiple plasma mirrors either between the focusing optic and the target as suggested by B. Dromey et al. [77] or even in a geometry similar to the one used in this experiment where the beam is recollimated after contrast cleaning on multiple PMs. This way the dilemma that, while focused laser intensity increases steadily with every newly developed laser system, the ionization threshold of target materials is constant requiring ever higher pulse contrast can be overcome enabling high contrast interactions at intensities far beyond those currently exploited using double plasma mirrors.

When the target is positioned in the focus, i.e. the far-field of the incident laser beam, an additional interesting effect can be observed. The beam is significantly spatially

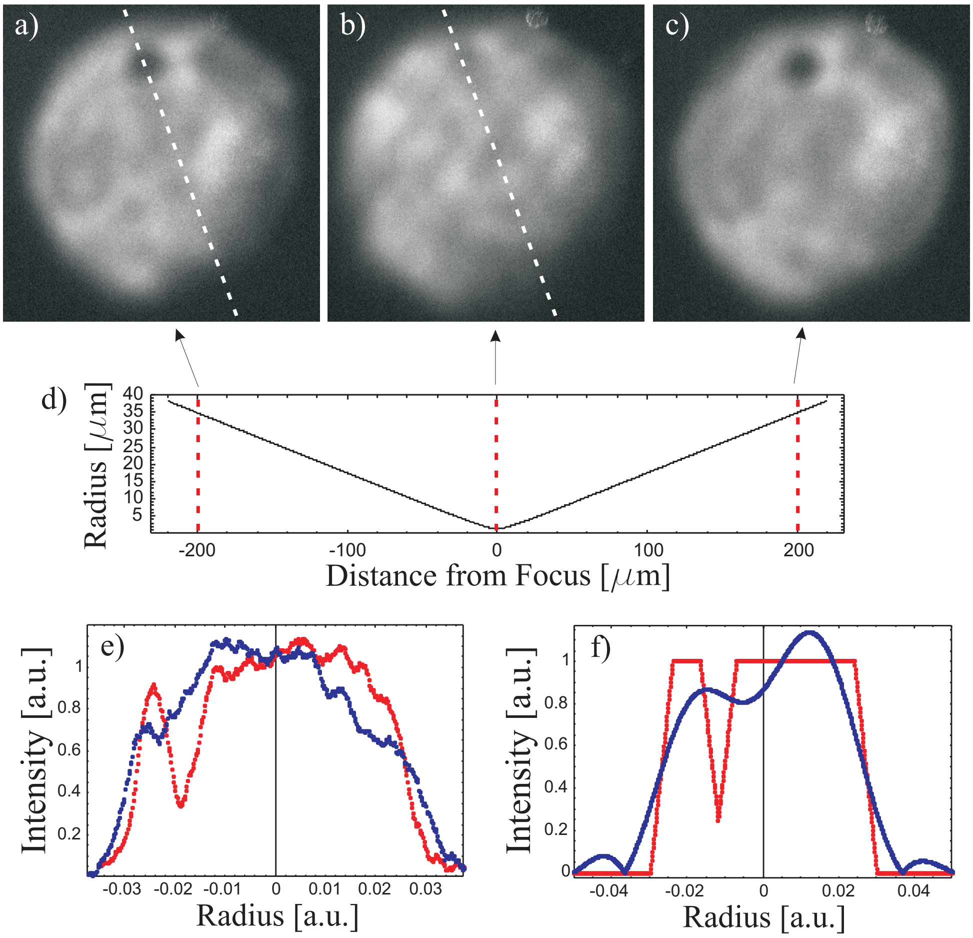

Figure 5.2: Spatial filtering of the fundamental can be observed when scanning the focal spot position with respect to the surface of the target. Figures a) to c) show near field images of the reflected infrared beam at focus positions of a) 200μm in front of the target, b) best focus on the target and c) 200μm behind the target. Obvious spatial filtering (i.e. disappearance of the hole in the incident beam (see also Figure 5.1)) can be observed. In d) we show the radius of the focusing laser beam on the target as a function of target position. The red dashed lines indicate the positions of the laser focus with respect to the target surface corresponding to the reflection conditions under which images a) to c) were taken. Graph e) shows vertical line-outs through figures a) (red) and b) (blue) respectively as indicated by the dashed line in the image. f) shows the results of a calculation comparing a near flat-top incident beam with a hole (red) to the reflected beam (blue) assuming the target is positioned in best focus and only the energy inside the second Airy minimum of the focus is reflected.

filtered. In Figure 5.2 (b) and the blue lineout in Figure 5.2 (e) the hole in the beam has completely disappeared and the edges of the pulse profile are less steep. This suggests that higher spatial frequencies of the beam, that are located further out in the wings of the focal region, are reflected less efficiently than those spatial frequencies focused in the center of the beam.

This effect was first observed at moderate intensities by K. Moncur [159] and can be understood from the results of earlier measurements with conventional plasma mirrors [77–79, 159–161]. In contrast to the near-field reflection the intensity distribution of the laser in the far-field is not a flat-top but rather its fourier transform, an Airy pattern. The more intense parts of the focal distribution generate a highly reflecting plasma faster and more efficiently than the low intensity wings which leads to a preferential reflection of the energy in the central region of the focus. As a result of this the higher spatial frequency contributions to the beam profile are suppressed and the resulting reflected beam is significantly smoothed.

To illustrate this the results of a simple model calculation are shown in figure 5.3. The incident beam profile shown in red in the figure was modeled to resemble the features of the real beam in the experiment (red line out in figure 5.2 (e)) - a near flat-top beam profile with steep edges and a dip on one side. This beam profile is fourier transformed to calculate the intensity distribution in the focus of the incident beam and the wings of the distribution are then truncated at different radial positions in figures 5.3 (a) to (c) to model the lower reflectivity of the low-intensity side lobes. The truncated spectra are depicted in black on the right side of the figure. Inverse fourier transform of the filtered focal distribution yields the beam profile of the reflected beam in the near-field which is plotted in blue on top of the initial beam. Especially (b) shows good qualitative agreement with the measured data. The hole in the beam has disappeared almost completely and the slopes have become shallower. For comparison plot 5.3 (b) it is also shown in figure 5.2 (f) next to the measured results.

To understand why it is at all possible to nicely reflect the fundamental beam off our HCPM at intensities around 10^{19} $W\ cm^{-2}$ while in other experiments [77] the reflectivity breaks down above 10^{16} $W\ cm^{-2}$ one has to consider that the key to the operation of plasma optics is that the intensity on target has to be sufficiently low before the main pulse to prevent early ionization. If the plasma is generated too long before the main pulse the plasma surface is deformed as a result of pre-plasma expansion and the specular reflection is lost. This implies that, for high intensity ($> 10^{18}$ $W\ cm^{-2}$), the pulse must already have a significant contrast (greater than 1:10^{10}) so that by the time of arrival of the main pulse the target surface is essentially still at solid density, and not a tenuous plasma with a long density scale-length, $L > \lambda_{\text{Laser}}$, compared to the laser wavelength.

To study this effect we have changed the pulse contrast at the target from high contrast ($\sim 10^{10}$) to low ($\sim 10^{8}$) contrast by varying the timing of the fast rise time (200 ps) Pockels-cell in the laser chain. Figure 5.4 shows the reflected near field profile for reflection

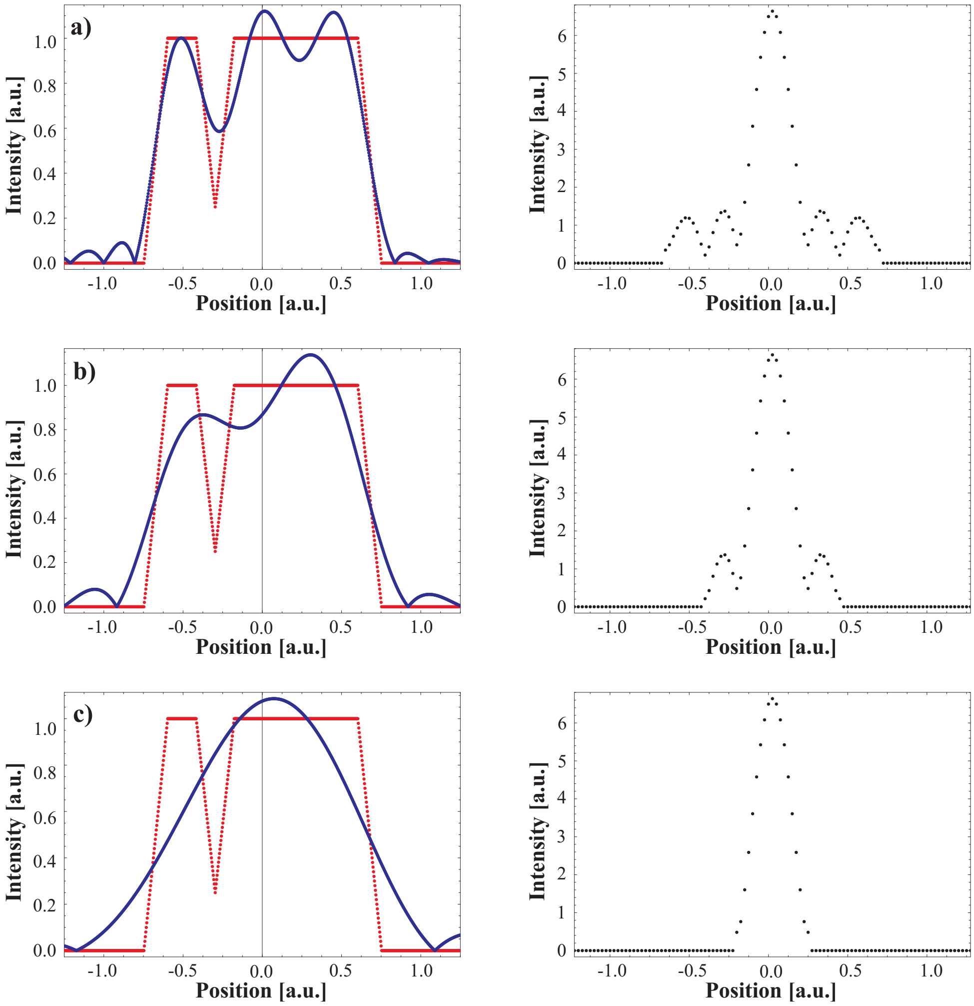

Figure 5.3: Results of a model calculation demonstrating the effect of low reflectivity in the wings of the focal distribution. (a), (b) and (c) show the incident beam profile (red) the reflected beam profile (blue) on the left and the filtered focal distribution on the right for different degrees of filtering.

of our fundamental 800nm laser beam at an intensity of 10^{18} $W\ cm^{-2}$ from the fused silica target under high and low contrast plasma mirror conditions respectively. This yields a very striking result: The specular reflection is completely lost under low contrast conditions.

In the low contrast case the reflected beam profile breaks up completely and no beaming is observed in the direction of the specular reflection (the dashed circle in Figure 5.4 (b) marks the area where the specular reflection would be expected). This beam break-up can be attributed to a reflection of the beam off a long scale-length pre-plasma generated by the pedestal of the laser pulse. This is in good agreement with results from previous plasma mirror experiments [77] that show strongly fluctuating PM reflectivity for intensities above 10^{16} $W\ cm^{-2}$.

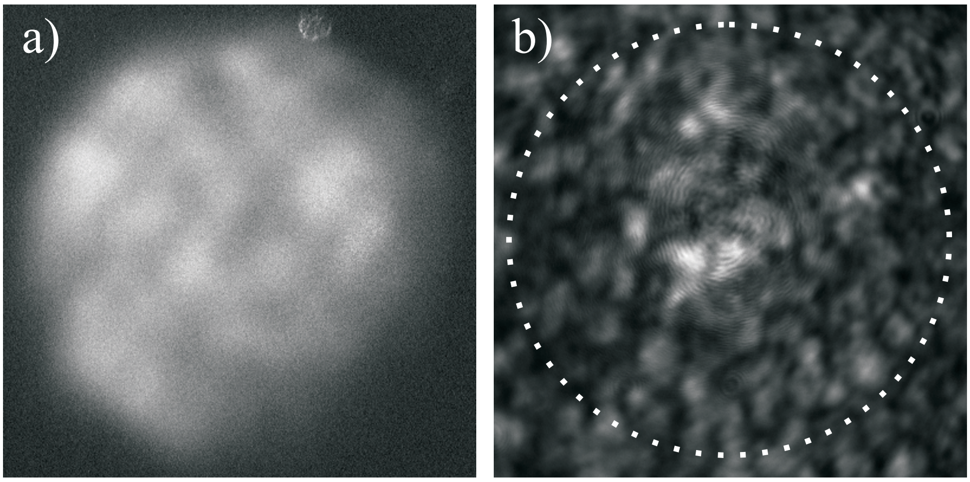

Figure 5.4: Reflected infrared beam profile for a) high laser contrast and b) low laser contrast. Note that in both cases the laser beam was reflected off the plasma mirror and the reflected near and far fields looked similar on N and F.

In the high contrast case the behavior of the plasma mirror at high intensities is very different. Figure 5.4 (a) shows a high quality beam reflected from the target surface. This is a clear indication that the beam was reflected off a well defined surface with a very short scale-length pre-plasma and that, despite the high focused intensity of the laser beam, the contrast was high enough to prevent an early ionization of the target. This has two important implications. One is that a plasma mirror can be operated properly at intensities much higher than those quoted in [77–79, 160, 161] provided the contrast of the laser beam incident on the PM is sufficient. The other is that the reflected fundamental of the driving laser from a solid target can be used to monitor the quality of the surface at the time when the main laser pulse is incident on it. Good reproduction of the near field indicates an interaction with a well defined, steep density gradient, while beam breakup implies that a long scale length pre-plasma was formed.

As a result monitoring the reflected fundamental light in, for example, an ion acceleration experiment from very thin foils as has been proposed recently [162, 163] could give important insight into the state of the target at the instance of the interaction with the main laser beam. It is also of interest in high-harmonic-generation experiments from solid targets since a surface that is 'clean' enough to reflect the fundamental laser beam is the absolute prerequisite for the observation of near diffraction limited harmonic beams the generation of which is presented and discussed in the next section of this thesis and in [64].

In the context of the results shown above it should be noted that in both, the low- and the high-contrast case, the laser beam was cleaned using the plasma mirror and the near- and far-field of the cleaned beam look identical excluding the possibility that the PM itself is the source of the different reflected beam profiles. This can be readily understood when considering that the interaction intensity at the PM position is much lower than at the target position. This ensures that, even though the contrast of the laser was changed significantly between the two measurements, the prepulse intensity is in both cases not sufficient to ionize the PM thus leading to a well defined reflecting surface in both cases.

5.2.2 Second Harmonic Generation

The second aspect studied in this experiment is the efficient generation of second harmonic radiation and its high beam quality. In conventional laser systems second harmonic generation using non-linear crystals (e.g. KDP, BBO) is a well established technique. The use of crystals does have some disadvantages though when very intense and extremely short pulses are used. Due to the insufficient bandwidth of the crystals and the GVD walk-off between the fundamental and the second harmonic the generated second harmonic is lengthened. In addition, for high power femtosecond laser systems, the intensities in the expanded beams become so high that non-linear effects both in time and space become intolerable even for ultra-thin crystals [164]. The B-integral [98] can get as high as 5 in a few 100 μm of crystal at intensities of $2 - 4\ TW\ cm^{-2}$. On the other hand expanding the beam even further is not feasible because ultra-thin crystals can only be fabricated up to limited diameters.

Harmonics from solid targets may provide an attractive alternative because the second harmonic is predicted to reach reflectivities $R_{2\omega} > 0.5R_\omega$ [46] for $a_0 > 3$ – provided high efficiency can be demonstrated without degradation of the beam quality. Since the harmonic generation is a surface effect, there should also be no pulse stretching owing to dispersive effects or bandwidth limitations.

To investigate the beam profile of the second harmonic and the efficiency with which it is generated on our High Contrast Plasma Mirror a 2ω interference filter was placed in front of the camera observing the PTFE screen in the beam path. To completely exclude any contribution from XUV-radiation-induced fluorescence of the screen a glass pellicle was placed between the target and the screen to absorb any XUV-light but leaving the fundamental and second harmonic unmodified. Figure 5.5 (a) shows a comparison of the reflected beam profile of the fundamental and the generated second harmonic when the target is positioned in the focus of the incident laser beam. A lower bound for the conversion efficiency is estimated by comparing the signals measured for the fundamental and the second harmonic and the filters used in the measurements. This comparison shows that >5 percent of the incident laser light is converted into the second harmonic. This value approaches 0.2, the value achievable with non-linear crystals at fs pulse durations.

The conversion efficiency may actually be substantially higher because the generated

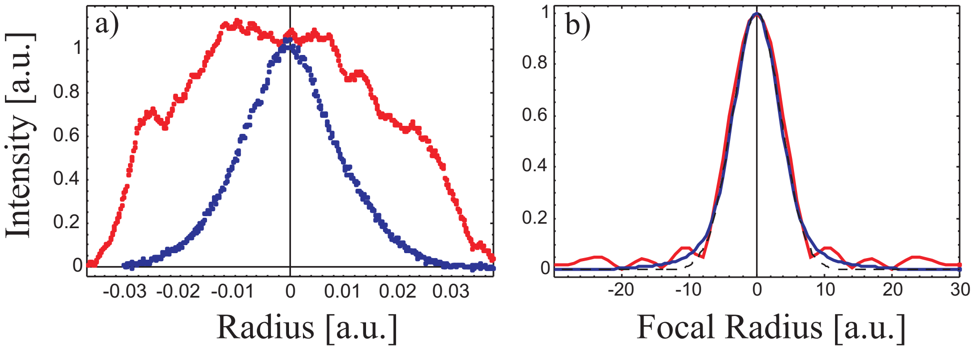

Figure 5.5: Comparison of fundamental and second harmonic emission from the target. Figure 4a) shows a comparison between the beam profiles of the fundamental (red) and the second harmonic (blue) measured on the PTFE screen behind the target (see figure 5.1a)). In b) we plot the profile of the source on the target for the fundamental (red) and second harmonic (blue) calculated via fourier transform from the beam profiles shown in a). The dashed black line corresponds to a gaussian fit to the central part of the 2ω focal distribution.

second harmonic is expected to have roughly two times the bandwidth of the interference filter used for suppressing radiation of other wavelengths. Furthermore the second harmonic is expected to be red-shifted with respect to the maximum transmission of the 2ω-filter as a result of holeboring effects [165] further reducing the measured signal.

Perhaps even more interesting than the conversion efficiency is the beam profile of the generated second harmonic. The measured near field profiles for the fundamental (red) and the second harmonic (blue) are shown in figure 5.5 (a). Two striking differences between the reflected IR- and the generated 2ω-radiation yielding interesting insight into the interaction on the HCPM can be observed. Firstly the divergence of the fundamental and the 2ω beams are very different and secondly the beam profile of the second harmonic is much smoother and more Gaussian-like than that of the fundamental. The divergence of the 2ω beam is half of that of the fundamental corresponding to a diffraction limited second harmonic beam being emitted from a source the same size as the laser focus. Consequently it should be possible to focus the 2ω beam to a diffraction limited focus at its wavelength. This implies that even at the lower bound of the conversion efficiency the peak intensity achievable at 2ω is likely to exceed that of a beam frequency doubled in a crystal, where the divergence of the frequency doubled beam is typically similar to that of the fundamental and consequently not diffraction-limited. Taking into account that the conversion efficiency is likely to be considerably higher than the measured value and that the duration of the second harmonic generated on the HCPM with fs-pulses is not elongated owing to bandwidth limitations the HCPM appears to be favorable, compared to nonlinear crystals, in terms of the focused intensity that is achievable.

To understand the difference between the beam profiles it is important to consider that the fundamental and the second harmonic have a very different origin. While the fundamental is the reflection of the incident laser beam off the over-critical plasma density surface formed on the target the second harmonic is generated during the relativistic interaction of the driving laser with the target. This difference becomes obvious when considering what kind of intensity distribution in the focus results in the experimentally measured beam profiles after the beam has expanded from the target. Figure 5.5 (b) illustrates this by comparing the normalized intensity distributions of the fundamental and the second harmonic in the focus of the incident beam, i.e. at the source of the expanding beam. The focal distributions were calculated from the measured beam profiles via fourier transformation taking into account the different wavelengths of fundamental and second harmonic.

Originating from the different generation mechanisms the source distribution of the fundamental and the second harmonic look very different. Despite the fact that the fundamental beam is spatially filtered owing to lower reflectivity in the wings of the focal distribution compared to its peak (see previous section) we still expect substantial reflectivity of the mirror at intensities of $10^{17}\ W\ cm^{-2}$. Thus it is reasonable that the side maxima of our focal distribution at least partially reflect the incident light as can be seen in the red plot in figure 5.5 (b). In contrast to this the second harmonic shows no emission originating from the side maxima of the focal distribution (blue curve in figure 5.5 (b)). Instead the source distribution is nearly Gaussian with some extra energy in the wings smearing out across the first minimum in the fundamental distribution.

This gives important insight into the mechanism generating the second harmonic on the High Contrast Plasma Mirror. The lack of harmonic radiation originating from the side lobes of the incident lasers focal distribution implies that the second harmonic is dominantly generated via the Relativistic Oscillating Mirror mechanism. Only the intensity in the central spot is larger than the relativistic threshold, i.e. only in this region the a_0 is larger than unity, which is the necessary condition for the generation of harmonics via this mechanism while the sub-relativistic side lobes do not emit. Note that the central peak in the source is not narrowed despite the nonlinearity of the generation process. The transverse motion of the electrons in the oscillating surface results in an oscillating mirror of about the same width as the focal spot [64]. This transverse electron motion is also discussed in more detail in section 5.3.3.

While it is nicely possible to explain the profile of the second harmonic beam with the ROM mechanism the question remains why the side lobes with intensities up to a few times $10^{17}\ W\ cm^{-2}$ do not emit at all even though CWE harmonics can be generated at intensities as low as $1 \times 10^{16}\ W\ cm^{-2}$ [34]. To understand this it is important to look at the CWE mechanism in a little more detail. CWE harmonics are generated via plasma waves excited in the target pre-plasma by bunches of Brunel electrons. This implies that a finite layer within the pre-plasma has to have the proper density to support oscillations at the frequency corresponding to the emitted harmonic. A step-like density ramp does not create any CWE [35, 91]. If we now take into account that the second harmonic is generated at a density of $n = 4n_c$ simulations show that, under the high contrast conditions present in this experiment, the relativistic laser pulse steepens the density profile in this density range so strongly that the scale length becomes practically zero [88, 91]. In this case the main source for harmonic emission is the relativistically oscillating plasma surface [30] which is only efficient for intensities higher than the relativistic limit of $I\lambda^2 = 1.38 \times 10^{18}\ W\ cm^{-2}\ \mu m^2$ leading to practically no emission from the side maxima of the focus.

Finally it is important to point out that this approach is obviously not limited to generation of the second harmonic. It could also be used in applications where, for example, the third or fourth harmonic are needed. It is important to note though that the beam profile for these harmonics would have to be investigated in detail since the CWE contribution to these harmonics is generated at higher densities in the pre-plasma gradient where the effect of steepening from the laser may be less pronounced. None the less this method constitutes a promising route for the generation of low order harmonics for applications where the use of nonlinear crystals is not feasible owing to damage issues and bandwidth limitations in such materials.

5.3 Characterization of Relativistic Harmonics

While the analysis of the reflected fundamental and second harmonic gave important insight into the interaction of high-contrast relativistic laser pulses with solid targets the main aim of our experimental campaign was the generation of high harmonics via the ROM mechanism and the subsequent characterization of this radiation. For this purpose the PTFE screen and CCD camera setup used for the detection of the fundamental (see figure 5.1) was replaced by an XUV flat-field spectrometer. A detailed description of the spectrometer is given in Appendix B.3 of this thesis.

The results shown and discussed in the following sections address several properties of relativistic harmonics that have not been studied before experimentally for 50 fs 10 Hz laser systems. In the first section spectral measurements showing harmonics up to the 40^{th} order of the fundamental 800 nm laser beam are shown, constituting, to the best of my knowledge, the highest surface harmonics ever observed from a 50 fs 10 TW-level laser system (note that the claim, the observation of the 35^{th} harmonic, made in [52] is most probably wrong since neither CWE nor ROM harmonics of the presented order are expected to be generated at the laser intensities used in those experiments). The second section focuses on the divergence of the generated radiation. Most notably the divergence of the ROM harmonics is observed to be constant for all observed ROM-orders. Finally, in the third section, the dependence of the harmonic emission on the target roughness is studied.

5.3.1 Spectral Measurements

The spectral measurements were conducted using the simplest possible experimental setup where the XUV spectrometer is mounted in the direct harmonic beam emanating from the target. This way a modification of the spectrum originating from the reflection off a collection mirror can be excluded. The only disadvantage of this method is, that slightly less signal is collected on every shot because the light is not focused on the slit. This does not really pose a problem though since the signal is strong enough without a collection optic and the divergence of our harmonics is relatively low anyway (see section 5.3.2).

Figure 5.6 gives an overview over the typical spectra generated in the high-contrast interaction at approximately $1 - 2 \times 10^{19}$ $W\ cm^{-2}$. Harmonics up to the 40^{th} order are clearly visible in the vertically binned spectra (left side of the figure) and even in the four raw camera images (right side of the figure). At the same time the transition from CWE to ROM harmonics can be observed in the same spectra owing to the large spectral range (20 nm–40 nm) spanned by the spectrometer. Both of these features shall be discussed in some more detail in the following. Note that the increasing background toward lower wavelength originates from an incoherent oxygen emission line around 18 nm and increased scattered light from the grating for smaller diffraction angles.

A strong decrease in the measured signal is observed between harmonics 19 and 21. This coincides with the cutoff expected for coherent wake emission in the case of the fused silica targets used in these measurements (see equation 2.28). At the same time harmonics are clearly visible beyond the cutoff. This radiation can only be attributed to the ROM mechanism and proves that the laser pulse contrast in this set of measurements was indeed high enough to enter the relativistic regime. This is in good agreement with other publications showing the transition to the generation of relativistic harmonics with similar intensities and pulse contrast [57, 59]. Another interesting observation on the long-wavelength side of the spectra is that the generation efficiency of the CWE harmonics is highest for the highest observed CWE-order (the 19^{th}). The investigation of this effect is still ongoing, but the explanation may well be the same as the one explaining why the second harmonic observed under essentially the same experimental conditions (section 5.2.2) shows the properties of a ROM harmonic rather than those of a CWE harmonic. The CWE mechanism is only efficient if the plasma from which the harmonics are generated has a finite scale-length pre-plasma. If the electron density profile in the high-contrast interaction was so steep that it did not support the generation of lower-order CWE harmonics this may lead to a signal like the one observed [91].

Turning to the short wavelength side of the spectrum harmonics up to the 40^{th} order can clearly be observed in the black line-out in figure 5.6, where the detector was shifted slightly toward shorter wavelength compared to the other shots shown. Note that the spectral lines beyond the 40th harmonic are incoherent emission lines which are also visible in low-intensity interactions in which no ROM harmonics are generated. The cutoff at the 40^{th} harmonic is in good agreement with the theoretical prediction given by equation 2.27. Using this equation one can calculate that a normalized amplitude of $a_0 = 2.2$, corresponding to an intensity of $1 \times 10^{19}\ W\ cm^{-2}$, is necessary to generate the observed harmonic spectrum. This value is, within the uncertainty of the focused intensity measurement, in good agreement with the experimental conditions. In fact, a harmonic measurement could thus even be used to estimate a lower limit for the focused intensity achieved in an experiment.

It is important to note that the high energy cutoff observed in the spectra can only be explained by the actual cutoff of the harmonic generation process and not by the properties of the XUV-spectrometer itself. A cutoff owing to a dip in the detector efficiency can be excluded. To illustrate this figure 5.7 shows the overall efficiency of the spectrometer used for the measurements presented in figure 5.6. To obtain the overall efficiency the spectral response of all components of the spectrometer were accounted for separately. The quantum yield of the x-ray CCD-camera is known and was taken from the data sheet of the manufacturer, the grating reflectivity was measured in an earlier experiment at the Daresbury synchrotron facility in the UK and the transmission of the Al filter and some CH contaminations were obtained from [92, 93]. Note that the thickness of the carbon contamination of 20 nm assumed here is only an estimate, the real value may be even higher but is difficult to determine precisely.

Looking at the detector efficiency calculated from the individual components it can be seen that it increases by one order of magnitude with decreasing wavelength in the range between 20 nm and 40 nm up to a cutoff at 17 nm originating from the L-edge of the Al filter [166] used to shield the spectrometer from IR radiation. The wavelength of the 40^{th} harmonic is 20 nm and thus well below the cutoff excluding that higher harmonics cannot be observed owing to decreasing detector sensitivity. At the same time the increase in detector efficiency toward shorter wavelength can also explain the dip observed in the spectrum around the 30^{th} harmonic. While the theory predicts a decrease in harmonic signal by a factor of approximately six between the 20^{th} and the 40^{th} harmonic the detector

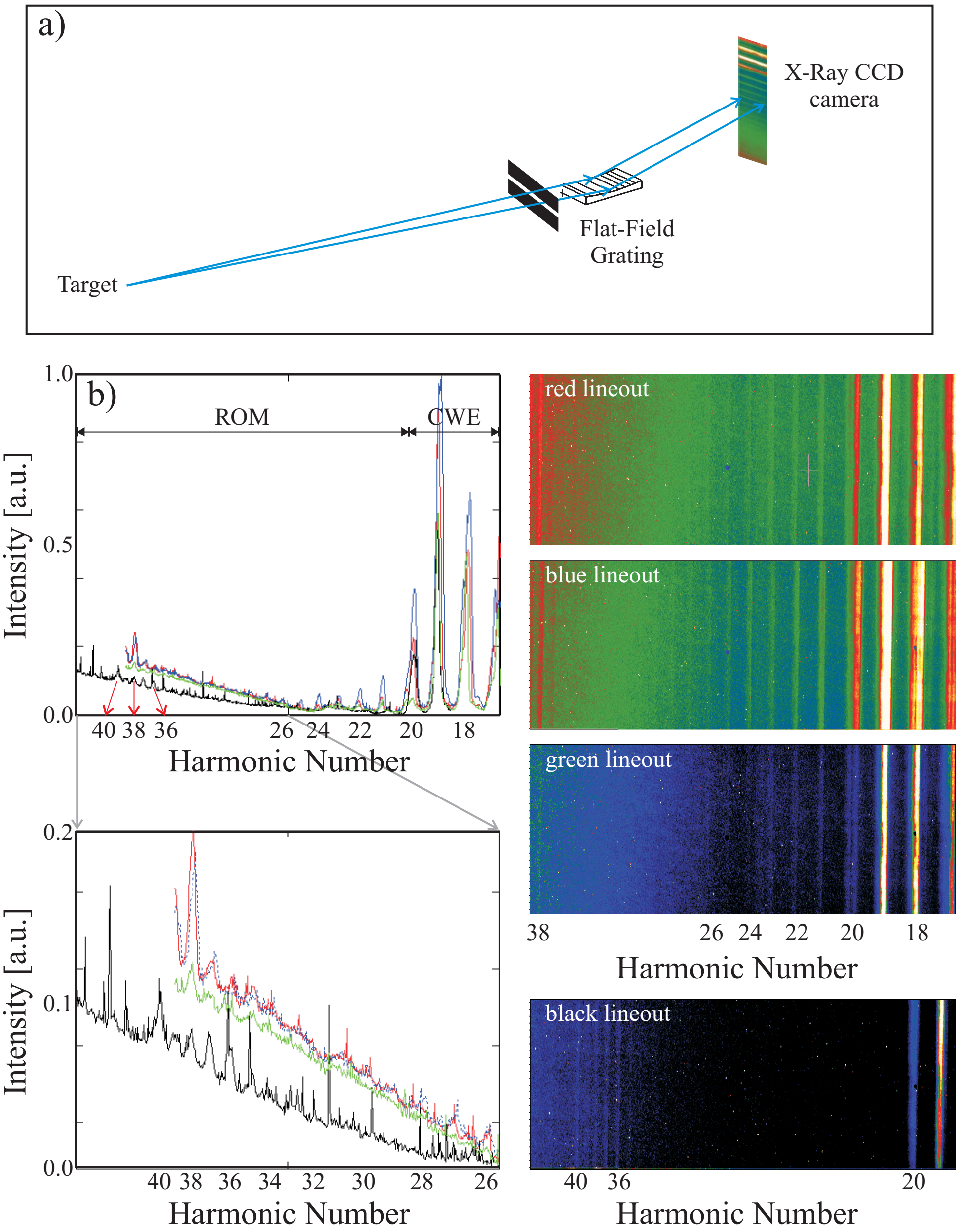

Figure 5.6: (a) Detector setup used for the measurement of relativistic harmonics. (b) Single-shot harmonic spectra generated in the high-contrast relativistic interaction of the ASTRA laser with highly polished quartz targets. Left side: harmonic spectra of four different shots obtained by binning the measured camera images showing the generation of harmonics up to the 40^{th} order. Right side: Raw X-ray CCD-camera images corresponding to the four lineouts clearly showing the generation of harmonics up to the 40^{th} order. The spectral lines at shorter wavelength are incoherent emission lines (see text).

efficiency drops by a factor of ten in the same range. This decrease in efficiency is mainly the result of the grating efficiency and the expected carbon contaminations. It may thus

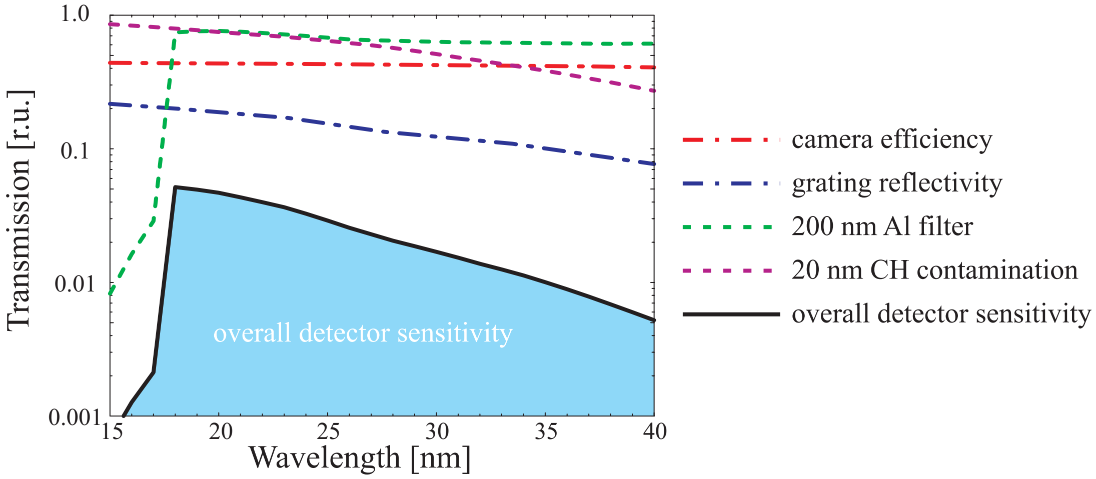

Figure 5.7: Overall efficiency of the XUV spectrometer. The quantum efficiency of the m-ray CCD-camera is taken from the manufacturer (Andor) data sheet, the reflectivity of the grating was measured and calibrated at the Daresbury synchrotron in the UK and the transmission of the Al filter is taken from [92, 93]. From the same source the transmission of the small CH contaminations expected to be present on all surfaces in the spectrometer was also obtained.

be even more pronounced if the contamination layers were thicker than the 20 nm assumed in the calculation. In an unfolded spectrum the lower order harmonics will thus have a higher intensity than the higher orders just as expected from theoretical predictions.

5.3.2 Divergence of Harmonics

While the demonstration of the generation of relativistic harmonics up to the 40^{th} order from a 50 fs Ti:Sa laser is an important new result in itself the aim of the experiments presented in this chapter is to not only demonstrate the generation but also to characterize ROM harmonics. For this purpose the detector setup used for the measurements shown in the previous section (figure 5.6 (a)) was modified as shown in figure 5.8 (a). An aperture placed in the harmonic beam was used to separate XUV-radiation emitted on-axis, i.e. in the center of the emission cone, which hit the spectrometer grating directly and off-axis, large divergence, radiation directed into the spectrometer using a custom-made grazing-incidence gold bending-mirror. It is important to note that, owing to the shallow angle of incidence, the gold mirror has an almost constant reflectivity in a range extending well beyond the 20^{th} harmonic. Both spectra, on-axis and off-axis, were recorded simultaneously with the spectrometer for every shot.

Two typical harmonic spectra obtained with this method for focused intensities of (b) $10^{17}\ W\ cm^{-2}$ and (c) $10^{19}\ W\ cm^{-2}$ respectively are shown in figure 5.8. In the sub-relativistic case b) both the on-axis as well as the off-axis spectrum extend up to the

19^{th} harmonic order corresponding to the CWE cutoff for the fused silica target used in the measurement. The signal visible around the position of harmonics 23 and 24 in the off-axis trace is the second diffraction order of a strong incoherent oxygen emission at 18 nm line which is also responsible for the short-wavelength background in figure 5.6. At relativistic intensities (figure 5.8 (c)) the picture changes completely. While the off-axis trace still shows the cutoff at harmonic 19 corresponding to the maximum CWE order expected and the signal from the second diffraction order of the oxygen line the on-axis spectrum clearly extends well beyond the CWE cutoff. These harmonics beyond the 19^{th} order cannot be explained by CWE and can thus be attributed unambiguously to the ROM mechanism. This directly shows that ROM harmonics are emitted with a divergence that is considerably smaller than that of the CWE radiation. The third trace between the two signals visible in the image is the result of imperfect focusing of the gold bending mirror and can be disregarded in the interpretation of the spectrum as it does not contain any additional information.

While this measurement proves in a nice way and especially in a single shot that the divergence of ROM and CWE harmonics is different it cannot be used to quantify the divergence of the individual harmonics because the harmonic beam is clipped with the on-axis aperture to allow the measurement of the two spectra simultaneously. In fact, even the configuration used for the spectral measurements shown in figure 5.6 does not offer a large enough field of view perpendicular to the dispersion direction in the spectrometer to extract the divergence of the individual harmonics. However, it is possible to rotate the camera on the spectrometer by 90 degrees to enlarge its field of view. While this limits the spectral range visible on a single shot to 4 to 6 harmonics depending on the wavelength range this configuration allows the extraction of the divergence of the individual harmonics directly from the measured spectra. The experimental configuration used for the divergence measurements is shown in figure 5.9 (a).

Figure 5.9 (b) shows the transverse beam profiles for selected harmonics in the ROM (harmonic orders 20 and 39) as well as CWE regime (harmonic 18) obtained with the method described above. The most striking observation from the beam profiles is that the divergence and the beam profile of the 20^{th} and the 39^{th} harmonic are identical. In fact, this also holds true for all other ROM orders observed in our experiment. The CWE orders on the other hand exhibit a larger divergence that decreases with the wavelength. Furthermore the beam profile of these harmonics is not as nice as that of the higher orders and fluctuates from shot to shot. An overview over the divergence of the XUV radiation as a function of wavelength is given in figure 5.9 (c). In this plot the striking difference between the divergence of the ROM and the CWE harmonics becomes even more obvious. For the relativistic harmonics it is constant at a value of 18 mrad while it is larger and

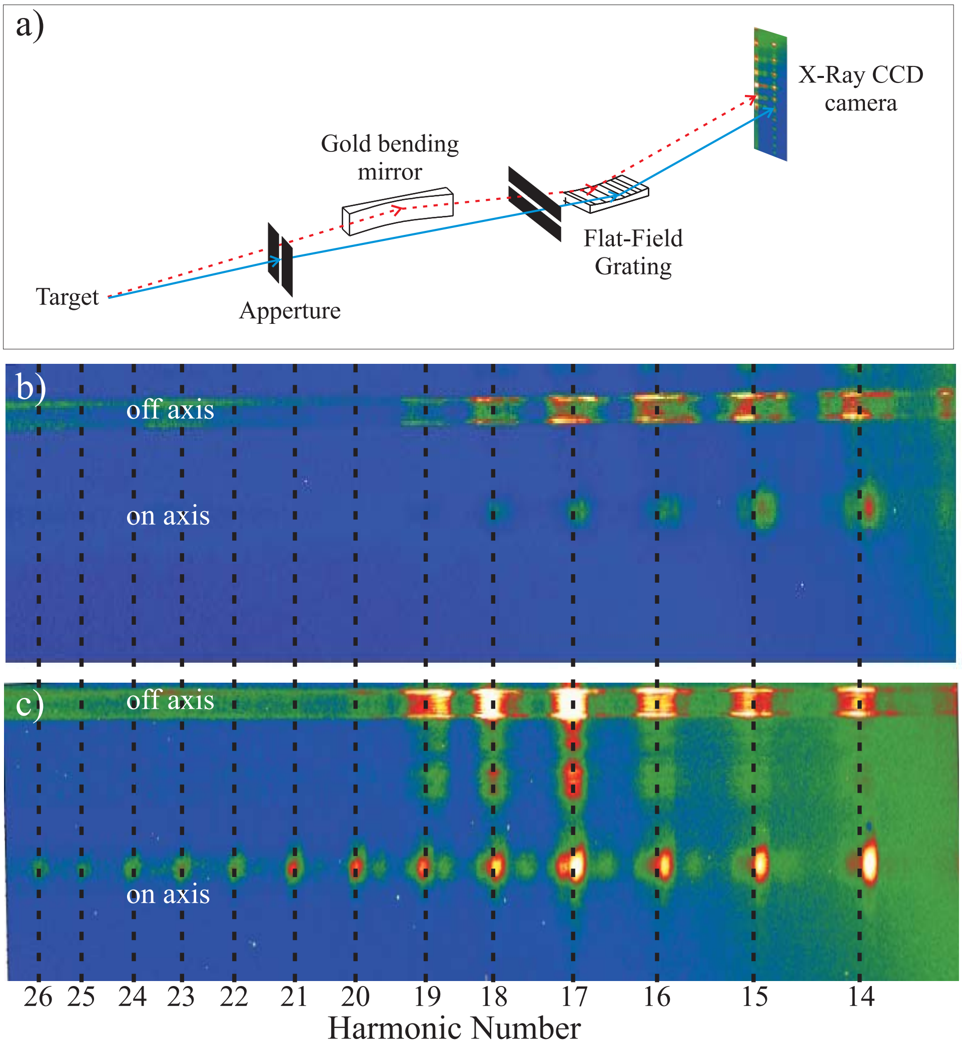

Figure 5.8: Experiment demonstrating the different divergence of CWE and ROM harmonics. (a) experimental setup showing the method for discriminating on-axis and off-axis radiation. The on-axis component is selected using a narrow aperture while the off-axis light is collected with a bending mirror and directed into the spectrometer. (b) and (c) show spectrometer images obtained for (b) $10^{17}\ W\ cm^{-2}$ and (c) $10^{19}\ W\ cm^{-2}$. For the high-intensity shot ROM harmonics are only visible on-axis while CWE is observed in both channels.

wavelength dependent for the lower orders. For reference the diffraction limited divergence Θ_q of a given harmonic q assuming constant source size for all wavelength corresponding to the laser spot size on the target is also shown in figure 5.9 (c). In this case it can be calculated from the divergence of the fundamental beam and, in the limit of small divergence angles (which is well fulfilled for the harmonics discussed here), is given by

$$\Theta_q = \frac{\Theta_{\mathrm{Laser}}}{q}, \tag{5.1}$$

where Θ_{Laser} is the divergence of the fundamental laser beam and thus a function of the focal spot size on the target. Note that in the experiment the divergence of the XUV radiation at 40 nm is diffraction limited when a source of the size of the fundamental laser spot on the target is assumed.

To explain the constant divergence of the ROM harmonics, which seems surprising at first glance, and understand the consequences of this behavior it is necessary to look at the different factors influencing the harmonic divergence in more detail. In general two things can lead to a divergence larger than the diffraction limited one deduced from the focal spot size of the fundamental. A source of the harmonics smaller than the one of the fundamental and phase variations of the harmonic beam across its radial profile, i.e. the generation of beams with a distorted wavefronts. In this context it is important to note that a distorted wavefront does not generally imply that the beam is not focusable to a diffraction-limited spot anymore. If the length-scale of the distortions is sufficiently large it may be possible to compensate them using a suitable complementary curved optic. The best example for this is actually a set of two spherical mirrors in a telescope where the first one introduces a wavefront curvature that is compensated by the second mirror. In contrast to that small scale ($\ll \lambda_{\mathrm{Laser}}$) distortions originating for example from the roughness of the target can, in general, not be compensated. The effects of target roughness will be discussed in more detail in the next section and neglected in the considerations presented here since the targets used in the divergence measurements where characterized to have negligible roughness ($< \lambda/20$) even for the 20 nm wavelength of the highest harmonic observed.

Let us first consider the source size of the individual harmonics and its influence on the harmonic divergence in more detail. While it is very difficult to measure directly for the high harmonics because it would require the aberration-free imaging of the interaction region in the XUV it can, in principle, influence the divergence of the individual harmonics significantly. In fact, in the limit of small divergence angles which is applicable for the high harmonics above the 20^{th} order, the divergence is inversely proportional to the source size. In the case of a flat-top beam it is

$$\Theta_q \approx \frac{d_q}{1.22\ \lambda_q}, \tag{5.2}$$

where d_q and λ_q are the source size and the wavelength of the harmonic of interest. From

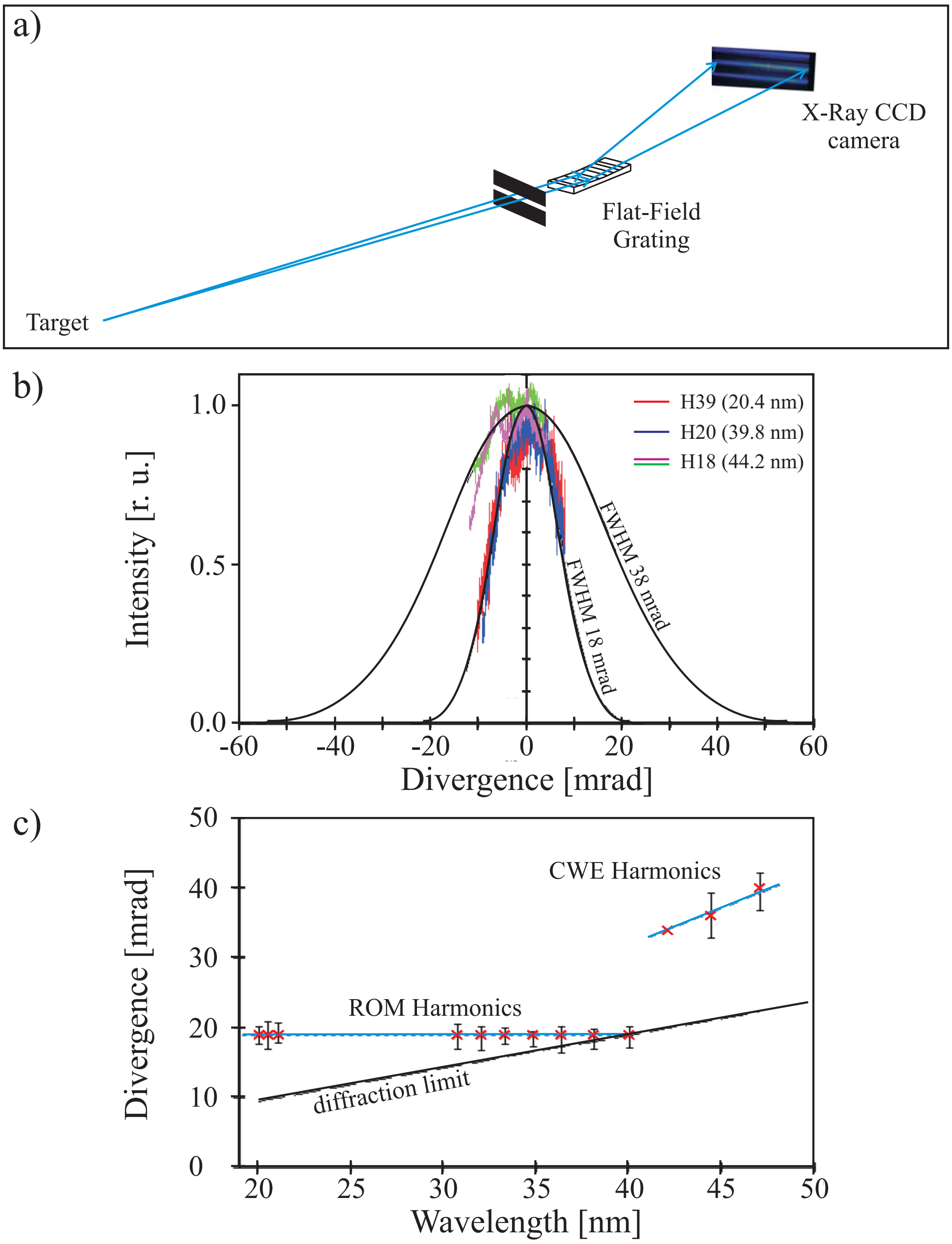

Figure 5.9: (a) experimental setup for the more detailed measurement of the harmonic divergence with the camera rotated to accommodate a larger divergence angle of the generated harmonics. (b) shows the beam profiles of various harmonics and (c) demonstrates the dependence of the divergence on the harmonic number. ROM harmonics can be seen to have constant divergence.

this equation one can immediately derive that, in order to obtain constant divergence of different harmonics from variable source sizes, these would have to decrease linearly with the harmonic wavelength. Considering that the radial intensity distribution in the laser focus is an Airy pattern for the flat-top laser beam used in the experiments and the

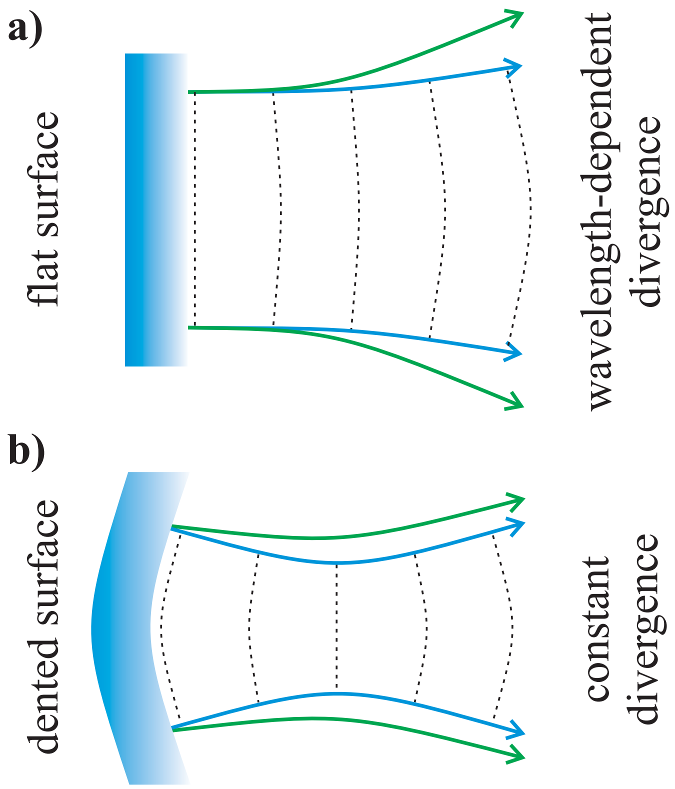

Figure 5.10: Illustration of the divergence of different wavelength laser beams from (a) a plane surface and (b) a curved surface. From the plane surface the divergence is governed by the wavelength while the divergence of all wavelength is constant for the curved surface.

generation efficiency, at least of the harmonics below the cutoff, saturates at intensities much lower than the peak intensity of the driving laser beam (see chapter 2.2.1) this will never be the case. The dependence of the source size on intensity should be much more pronounced for the harmonics near the cutoff than for the lower orders. While the only way of investigating this in more detail would be to actually image the harmonic source, and an influence of the source size on the observed divergence is definitely present it cannot explain the observed constant divergence in a satisfactory manner.

A much better explanation can be found when assuming the generation of harmonics with curved wavefronts. Figure 5.10 illustrates the effect of a curved wavefront on the divergence of different harmonics. While in (a) the harmonics generated with a plane wavefront exhibit a wavelength-dependent divergence that can be obtained using equation 5.1 the harmonics generated on the curved surface, and thus with curved wavefronts, in (b) travel through a focus (the size of which is wavelength-dependent) and then expand with constant divergence as long as this is larger than the intrinsic divergence expected from a plane wavefront as a result of diffraction.

In the experiment two different effects are definately present that will contribute to the curvature of the wavefront of the emitted harmonics. Denting of the oscillating surface owing to radially varying light pressure in the focus [167] and intrinsic phase effects in the harmonic generation mechanism itself [65]. While the first effect becomes more pronounced the longer the driving laser pulse is [64, 167] and should essentially disappear in the limit of a single cycle laser pulse the second effect is always present even for fixed ions and a perfect surface. The physical origin of this intrinsic phase effect can be understood when considering that the target surface acts like a strongly driven oscillator. In this case the relative phase between the driver and the surface will be a function of the ratio between driving frequency ω_L and resonance frequency ω_res, $\phi_\mathrm{rel} = F(\omega_\mathrm{L}/\omega_\mathrm{res})$ and thus also a function of the local plasma density. Furthermore it may become a function of intensity for large oscillation amplitudes of the anharmonic oscillation. In [65] D. an der Brügge et al. derive an analytical expression for the dependence of the relative phase on laser intensity and plasma density in the relativistic limit from 3D PIC-simulations. It yields

$$\phi(a_0, n_\mathrm{max}) = 2.7\ a_0 \frac{n_\mathrm{c}}{n_\mathrm{max}} - 0.32, \tag{5.3}$$

where n_c and n_max are the critical density for the fundamental laser frequency and the maximum density of the target respectively. However, care has to be taken when applying the equation to the conditions in our experiment since a single-cycle driver pulse and fixed ions where assumed in the simulation. Under realistic conditions the electron density will decrease radially across the focal spot owing to the light pressure of the driving laser pulse. This will tend to decrease the influence of the intrinsic phase effects on the curvature of the wavefronts of the generated harmonics.

A careful analysis of the denting necessary to generate a beam of the measured divergence, taking into account the oblique incidence of the driving laser pulse, yields a depth of the surface modulation of approximately 30 nm. To within the experimental accuracy this value is also in good agreement with the results of PIC simulations studying the denting over a wide range of parameters for the ASTRA as well as the VULCAN laser system [64]. In comparison the wave-front curvature corresponding to a 30 nm dent the intrinsic phase effect calculated from equation 5.3 is a factor of two to three smaller when assuming constant density across the target. Under the conditions in our experiment this will be even smaller owing to the profile steepening mentioned above. This means that the constant divergence observed for all ROM harmonics in our experiment can be attributed mainly to a denting of the target surface. This opens intriguing possibilities for future experiments because it means that the generated harmonics travel through a focus in front of the target in which intensities much higher than those of the driving laser maybe as high as the Schwinger limit [33] of $10^{29}\ W\ cm^{-2}$ can in principle be achieved

[32]. However, for this to become reality the focusing of the harmonics would have to be aberration-free. In this experiment that was definitely not the case for two reasons: first the shape of the generated curved wavefront follows the intensity profile of the laser and is thus an Airy-pattern and not a sphere and secondly the angle of incidence in our experiment was 30° which will introduce further aberrations.

Never the less the experiments presented here demonstrate the generation of near-diffraction-limited harmonic beams at wavelength as low as 20 nm which propagate through a focus. Furthermore several possibilities are available for improving the quality of the generated harmonic. Decreasing the angle of incidence will decrease spherical aberrations, The use of few-cycle laser pulses for the harmonic generation can strongly suppress the effect of target denting and An der Brügge et al. have shown that tailoring focal intensity distribution can be used to alter the wavefront of the generated harmonics [65]. In principle one could try to create a spherical focal intensity distribution to achieve aberration-free focusing or one could also think of applying micro-machined targets with pre-curved surfaces prepared in the proper way to compensate the aberrations introduced by the denting. To explore the possibilities of improving the harmonic focus we have also conducted a series of 2D-PIC simulations which are presented in [66].

5.3.3 Influences of Target Roughness

Of equal importance for the beam quality of the emitted harmonics as the large-scale denting is the influence of the target roughness on the harmonic divergence. In fact, even a surface that is perfectly flat or spherical on the scale of the focal spot diameter will not generate a nice harmonic beam if the target roughness on a sub-wavelength transverse scale is too large. To illustrate this figure 5.11 shows the influence of a random phase error on the quality of a beam emitted from a gaussian source. As the roughness increases more and more energy is scattered out of the specular direction and the beam quality degrades. For a phase error of $\lambda/2$ no beaming is observed anymore. Note that the relevant wavelength in this case is that of the harmonic and not the fundamental. As a consequence of this one would expect the beaming of the high harmonics observed in the experiment presented here only from targets with a surface roughness considerably smaller than 10 nm.

To study this systematically measurements of the harmonic spectrum and divergence were conducted with targets of different roughnesses. For this purpose all targets where accurately characterized using an optical interferometric surface profiler (Wyko NT9300 from Veeco) in the RAL target-preparation laboratory. Figure 5.12 shows the experimental setup, surface profiles and measured harmonic spectra for targets of sub-nm and 18 nm rms surface roughness. Interestingly the harmonic spectra obtained from the two

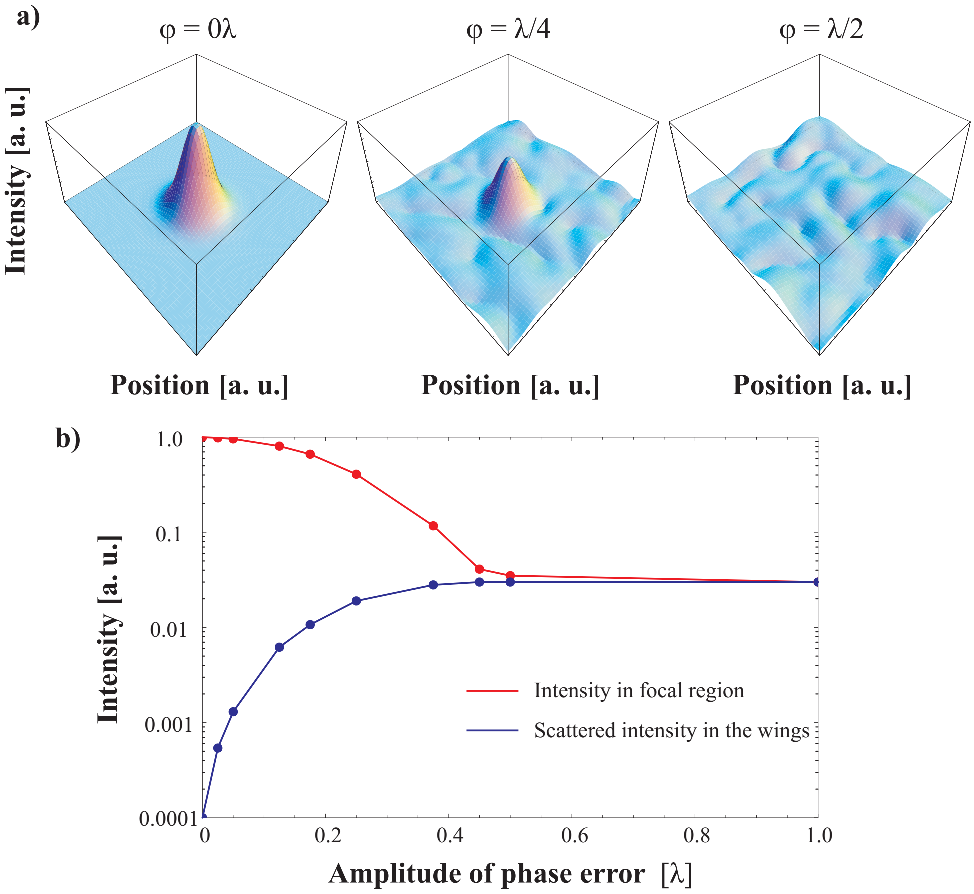

Figure 5.11: Effect of random phase errors on the beam quality of radiation emitted from a source with gaussian intensity distribution. (a) shows the near-field beam profile of the emitted radiation for three different phase error amplitudes. In (b) the intensity in the main peak and the wings is plotted as a function of the random phase error amplitude. For a phase error $> \lambda/4$ no beaming of the radiation is observed.

different targets are the same both spectrally as well as in the divergence of the harmonic radiation despite a surface roughness on the order of the wavelength of the highest generated harmonic (the 40^{th} order at approximately 20 nm). Only when the roughness is increased further to 164 nm rms it begins to influence the generated harmonics. Figure 5.13 shows the results from a measurement with such a target. Only CWE harmonics are observed and the radiation had to be refocused with a collection mirror (see figure 5.13 (a)) to collect more photons and be able to measure any signal at all.

These experimental results seem to contradict the theoretical considerations presented at the beginning of this section. While the random phase-error model predicts no beaming in the range between harmonics 20 and 40 for an 18 nm roughness target exactly that is observed. Only for a roughness 15 times higher than the wavelength of the highest

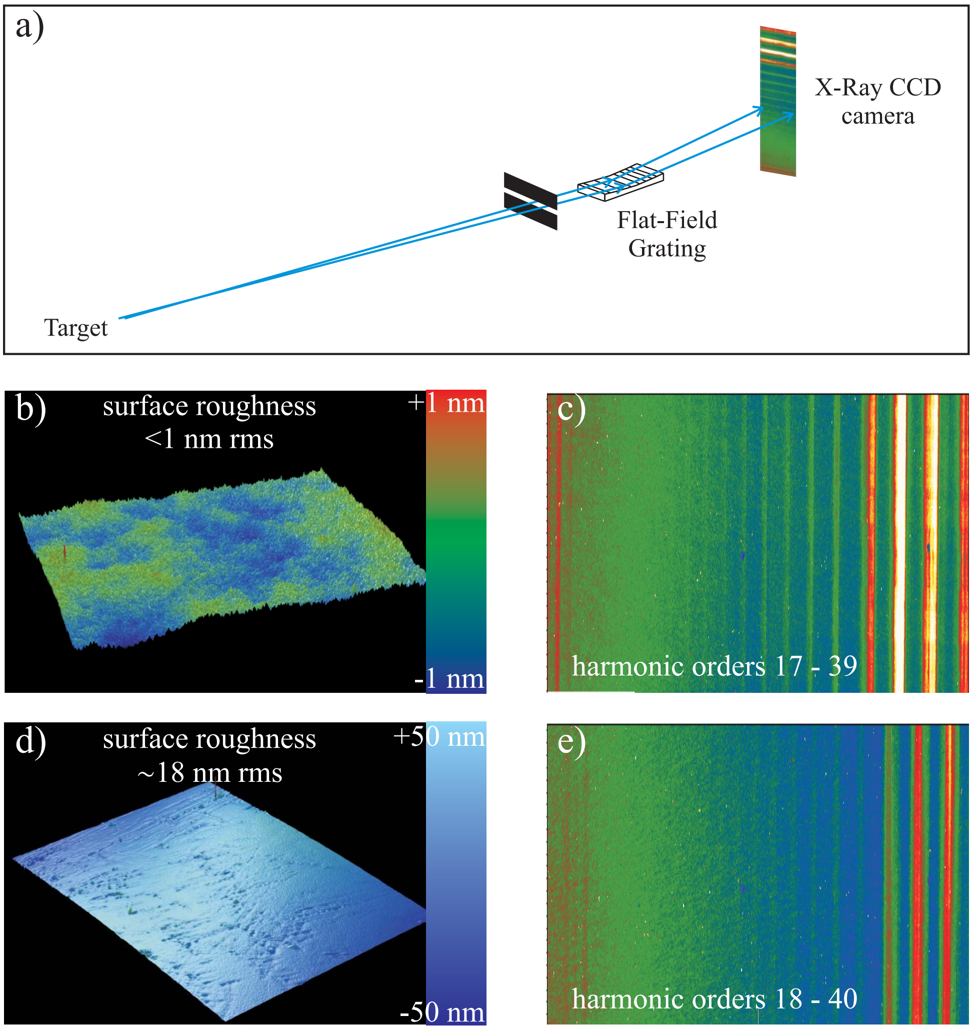

Figure 5.12: Experimental setup (a) and measured harmonics from two targets with different sub-wavelength surface roughness. (b) and (d) show the surface of the two targets measured using a Wyko NT9300 Optical Profiling System (Veeco) surface profiler. The spectra generated off the two targets are shown in figures (c) (sub-nm roughness) and (e) (18 nm rms roughness) respectively.

harmonic i.e. on the scale of the fundamental wavelength the harmonics are scattered into a wide emission cone.

To explain this discrepancy between the model and the experimental observation it is necessary to look more closely at the generation mechanism for ROM harmonics. The key is the reflection of the incident laser pulse off the relativistically oscillating critical density surface. The harmonics are generated off a dynamically moving bunch of electrons and not the static surface of the rough target. If the trajectories of the electrons in their oscillatory motion are considerably larger than the roughness of the target significant

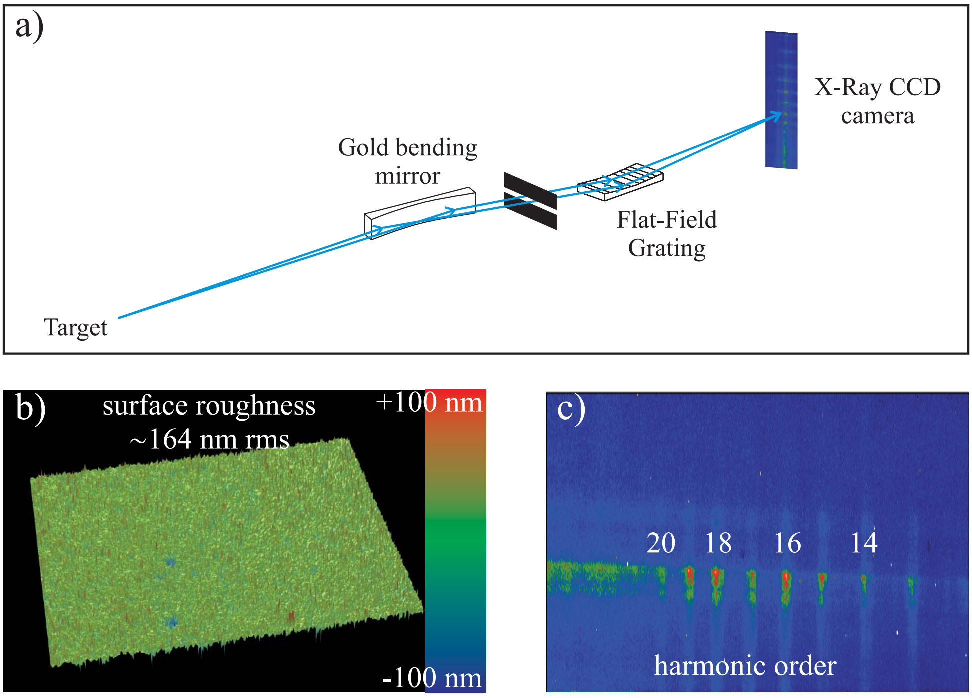

Figure 5.13: Measurement of harmonics generated from a target with large surface roughness. A collecting mirror was used to accumulate more signal on the CCD. b) and c) show the surface profile and harmonic spectrum generated from the 164 nm rms roughness target.

smoothing of the surface will occur and the generated harmonics will beam. Only if the roughness is larger than the electron trajectories diffuse scattering of the generated harmonics is expected. An indication that the electron oscillation amplitude is indeed greater than 20 nm can be found when estimating the oscillation amplitudes of the mirror surface in the simple oscillating mirror model presented in section 2.2.1 of this thesis. This assumption is further supported by more sophisticated PIC simulations. Figure 5.14 shows the trajectories of the individual macro-particles as obtained from such a simulation. The electrons move as much as 50 nm parallel as well as perpendicular to the surface of the target during one laser cycle which is clearly sufficient to smooth out a 20 nm rms roughness target and allow the generation of a nice harmonic beam. In addition recent 2D-simulations of a rough target supports these results [94].

This result has important implications for the generation of even higher harmonics with more powerful laser systems. If the roughness of the targets would have to be significantly smaller than the wavelength of the harmonics the generation of harmonic beams in the sub-nanometer wavelength range would not be possible because targets with such a low surface roughness do not exist. In fact, in these cases even mono-layers of contaminants would be sufficient to destroy the phase properties of the generated harmonics. Fortunately the

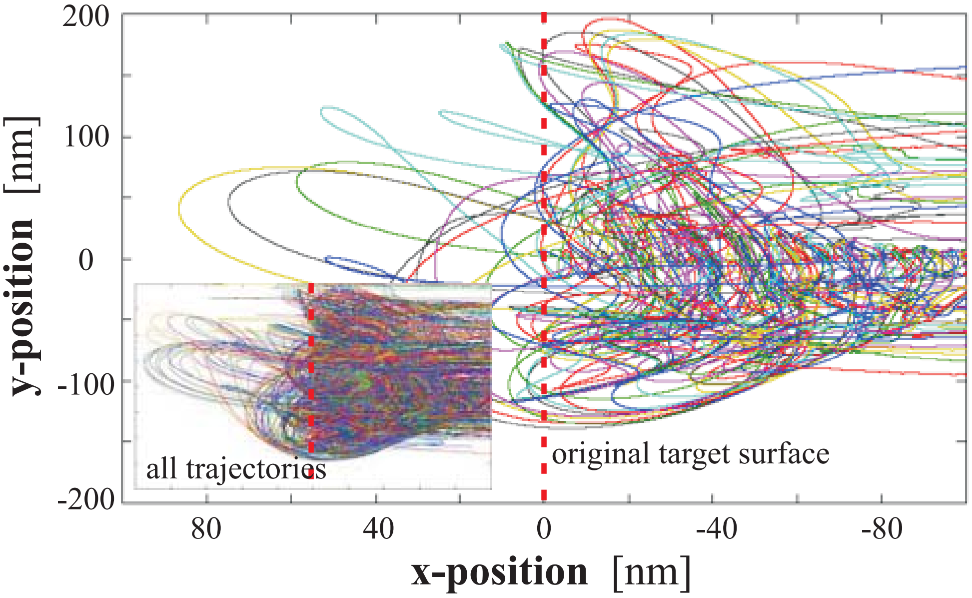

Figure 5.14: Trajectories of individual macro-particles in a 1D PIC-simulation with $a_0 = 3$ and 30° angle of incidence and a two-cycle laser pulse. Only one out of twenty trajectories is shown in the main figure (the inlay shows all trajectories). Simulation and figure courtesy of S. Rykovanov.

smoothing of the surface lifts this severe constraint and allows the generation of beaming harmonics even in the keV-range as has already been demonstrated by Dromey et al. [58].

5.4 Summary

The experiments described in this chapter have lead to a wealth of new insights into the relativistic interaction of ultra-high contrast 50 fs laser pulses with solid density targets. Novel features in both the reflection of the fundamental as well as the generation of high-order relativistic harmonics have been observed.

The demonstration of high quality fundamental and second harmonic beam profiles after the relativistic interaction of the driving laser pulse with the fused silica target constitutes the first demonstration of a High Contrast Plasma Mirror HCPM. This proves that the concept of the plasma mirror can be extended into the relativistic regime if the contrast of the incident pulse is high enough thus allowing the staging of multiple PMs. This goes beyond the concept of the conventional double plasma mirror and offers the possibility of generating pulses of unprecedented contrast for the ultra-high power laser systems envisioned for the future [154, 155]. Furthermore, when placed in the focus of the driving laser beam, the experiments demonstrate that the HCPM acts as an efficient spatial filter that does not suffer from damage limitations as conventional systems relying on pinholes do. The generation of a second harmonic beam with a conversion efficiency larger than five percent in a diffraction limited beam and without the bandwidth limitations always present when frequency doubling in a nonlinear crystal may constitute an alternate route toward frequency doubling in future experiments with the next generation lasers mentioned above.

In the measurements of the high-order harmonics emitted from the fused silica target harmonics up to the relativistic cutoff have been demonstrated. The ROM harmonics up to the 40^{th} order are furthermore shown to be emitted in a near-diffraction-limited beam with constant divergence. The constant divergence is attributed to the generation of the harmonics with a curved wavefront mainly as a result of the denting of the target surface during the interaction implying that the generated radiation propagates through a focus. With proper tailoring of the target and/or the laser beam it may be possible to achieve unprecedented intensities in this focus far beyond those achievable with the fundamental laser beam [32]. Finally the influence of the target roughness on the harmonic generation process was studied. Near diffraction-limited harmonic beams are observed even from targets with a surface roughness on the scale of the wavelength of the generated harmonics. This implies that the target surface is significantly smoothed during the harmonic generation process. The key to this smoothing is the transverse motion of the electrons in the oscillating mirror surface. This smoothing also has important implications for the generation of harmonics in the sub-nm wavelength range since the preparation of targets with initial roughnesses much smaller than these wavelength is simply impossible.

Chapter 6

Surface Harmonic Generation with LWS10

While the detailed study of the harmonic generation mechanisms from solid targets and the characterization of the resulting XUV beams is of great importance the ultimate goal remains the generation of a single ultra-intense attosecond pulse from such a plasma source. To achieve this goal it is necessary to confine the emission of the harmonics used to synthesize the as-pulse to a single cycle of the driving laser electric field. This can, in principle, be achieved in two different ways. The most straight-forward solution is to generate the harmonics with a driving laser with such a short pulse duration that its intensity is only sufficiently high for harmonic generation during one half-cycle of the electric field. This has been demonstrated for harmonic generation from gaseous targets [8] but is very challenging for solid-target harmonics as it requires a phase-stabilized sub-5-fs laser pulse with relativistic intensity. The other possibility is to use a method dubbed relativistic coherent control or polarization gating [38, 83, 84] which relies on the fact that the ROM mechanism is very sensitive to the polarization of the driving laser pulse (see Chapter 2). By manipulating the polarization of a longer laser pulse in such a way that it is only linear for the duration of one cycle of the pulse it should therefore be possible to generate a single as-pulse. This method has also been demonstrated for gas harmonics using various schemes [11, 168] but it remains to be shown that it can be applied to surface harmonics.

Driven by the proof that the harmonic emission from solid targets is phase-locked and thus suitable for the generation of as-pulses (Chapter 4, [63]) and the generation of low-divergence beams of relativistic harmonics (Chapter 5, [64]) ideally suited for applications with 40 fs pulses we have conducted a series of experiments using the 8 fs LWS10 laser system to explore the possibility of harmonic generation in the few-cycle regime and come significantly closer to the generation of single as-pulses from solid targets. (For details on

LWS10 see Chapter 2.3).

In this chapter and also in [62] I present, for the first time, conclusive evidence of the generation of surface harmonics up to the CWE-cutoff from a fused silica target using a sub-10-fs driving laser. While the driving laser pulses used for harmonic generation where not short enough yet to actually generate a single as-pulse the experiments nevertheless demonstrate the ability of the novel OPCPA-based LWS10 system to reproducibly generate bursts of XUV-radiation with sub-10-fs duration. Beyond the mere demonstration of harmonic generation with such a system the results give interesting new insight into the sub-cycle dynamics of the CWE-mechanism as the effects of unequal spacing of the individual as-pulses emitted (see Chapter 2.2.2) becomes more pronounced and, in fact, directly visible in the harmonic spectra. In addition the, to the best of my knowledge, first systematic study of the dependence of CWE on the laser polarization is presented.

6.1 Experimental Setup

Before the measurements are presented a short overview of the experimental setup used shall be given to introduce the main components referred to later during the discussion of the results.

As has been mentioned above the 8 fs LWS10 laser system was used for these experiments. After amplification the pulses are compressed using a combination of bulk glass and chirped mirrors and then focused onto a fused silica target using an F/3 silver-coated 30° off-axis parabola reaching spot-averaged intensities as high as $1.4 \times 10^{19}\ W\ cm^{-2}$ (see section 3.2.2). A detailed analysis of the focal spot and the pulse duration during the experiments is presented in Chapter 3.2. The target is positioned in the focus of the parabola under an angle of 45° to allow the extraction of the specularly reflected harmonic beam. A schematic drawing of the setup is shown in figure 6.1 (a). Two different detector setups where used to measure the spectrum of the emitted XUV-radiation. The harmonic beam was either refocused to a line-focus on the entrance slit of the ACTON normal-incidence spectrometer using a spherical gold-coated mirror (figure 6.1 (b)) or detected directly in the divergent XUV-beam using the McPherson grazing-incidence spectrometer (figure 6.1 (c)). A detailed description of the XUV-spectrometers can be found in Appendix B. It is important to note that while configuration (b) was used extensively in the beginning of the experimental campaign all the results presented here were obtained using the grazing-incidence spectrometer in the direct beam. The big advantage of this setup is the larger detectable spectral range as the reflectivity of the gold-mirror limits the spectral range to harmonic orders 16 and lower in configuration (b) and the larger spectral resolution.

Finally a broad-band achromatic quarter- or half-wave plate can be placed in the beam

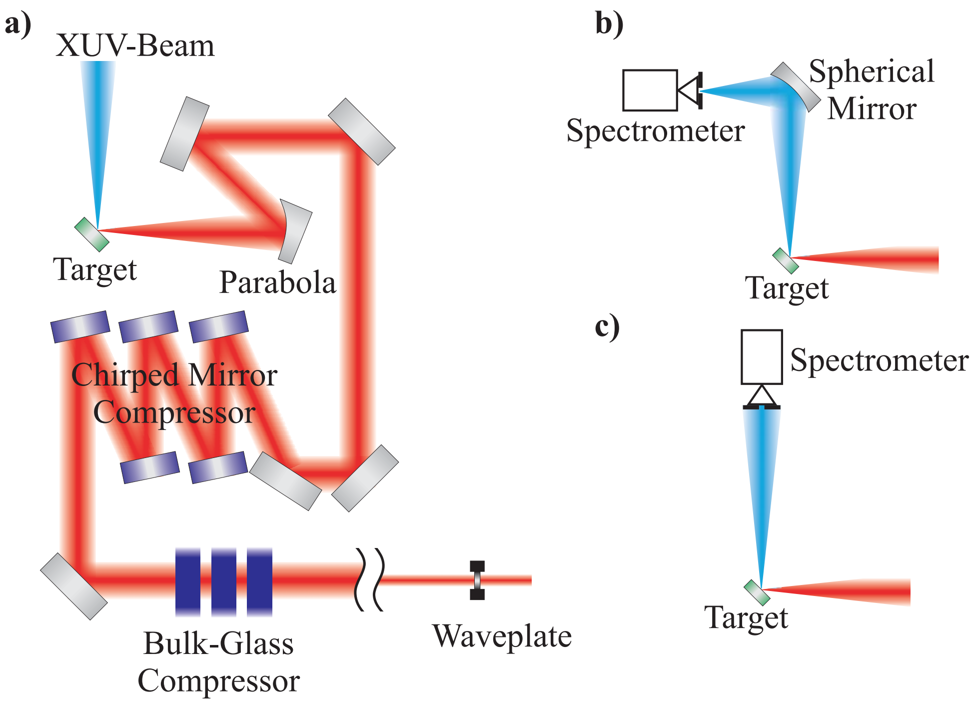

Figure 6.1: Experimental setup for the generation of high harmonics with the LWS10 system. (a) After the compression of the pulses to a duration of 8 fs using bulk glass and chirped mirrors the beam is focused under 45° AOI onto a fused silica target using an F/3 silver-coated 30° off-axis parabola. Furthermore a wave-plate can be inserted into the setup to modify the polarization of the laser beam. Two different setups where employed to record the harmonic radiation using either a gold-coated focusing mirror (b) or an XUV spectrometer placed directly in the diverging beam (c).

after the final NOPA-amplifier to vary the polarization of the laser beam and study the dependence of harmonic generation on this parameter. Note that in LWS10 the wave-plates can be positioned in the stretched beam as the bulk glass and chirped mirror compressor is insensitive to the beam polarization. This is not possible in conventional laser systems based on grating-compressors as the gratings would be damaged by the component of the beam polarized parallel to the grating lines. The great advantage of placing the polarizers in front of the compressor is that optics with small apertures on the order of 15 mm which are readily available can be used for polarization manipulation. In addition the intensity in the optical elements is kept low owing to the fact that the pulse is still stretched making the issue of nonlinear effects in the wave-plates negligible. The biggest advantage of the polarization insensitive compressor however is the fact that it should also be much simpler to employ a more sophisticated polarization gating setup like in [11, 168] into such a system as this could also be positioned in front of the compressor.

6.2 Surface Harmonics from a sub-10fs Driver Laser

The discussion of the experimental results obtained with the LWS10 laser system will be presented in two separate sub sections. The main part of the discussion is dedicated to spectral measurements and especially the explanation of distinct substructures observed on the individual harmonics. A simple model is presented to clarify the origin of these features. In the second section the dependence of CWE-harmonic emission on the laser polarization is studied. This is of particular interest not only from a fundamental point of view, but also when polarization gating is to be employed in the CWE-regime as the design of a gating-setup depends critically on the polarization response of the harmonic generation process.

6.2.1 Spectral Measurements

As has been mentioned before the spectral measurements presented in this section where all conducted using the McPherson grazing-incidence XUV-spectrometer positioned directly in the divergent harmonic beam emanating from the target (configuration (c) in figure 6.1). Two raw images of the harmonic spectra at 40 nm (top) and 60 nm central wavelength (bottom) as recorded by the camera of the spectrometer are shown in figure 6.2. Two things are immediately visible from the raw images of the spectra: The harmonic spectrum exhibits a cutoff at the 20^{th} harmonic and the individual harmonics are very broad and not homogeneous in shape. Both of these basic observations already give important insight into the harmonic generation with the 8 fs pulses.

The cutoff at harmonic 20 observed reproducibly in the measurement is consistent with the maximum harmonic expected from the CWE-process for the fused silica target used in the measurement [34]. This suggests that, despite the relativistic intensities in the laser focus (see Section 3.2.2), the harmonics in this experiments are predominantly generated via the CWE-mechanism. This is in agreement with a similar observation in experiments using the ATLAS laser (Chapter 4) where the emission of ROM-harmonics is also strongly suppressed in the relativistically intense focus. The origin of the suppression lies in the generation of a pre-plasma gradient by the ps-pedestal of the laser pulses which prevents the main peak of the pulse from interacting with a steep plasma-density step. In fact, so far ROM harmonics have only been observed in experiments in which extra measures where taken to improve the pulse contrast using either a plasma mirror ([57, 58, 61] and Chapter 5) or frequency doubling of the driving laser pulse [59].

Explaining the width of the individual harmonics and their inhomogeneous shape is not so straight forward. While broadening of the harmonics compared to those observed in experiments with the ATLAS laser is expected simply owing to the shorter duration of the

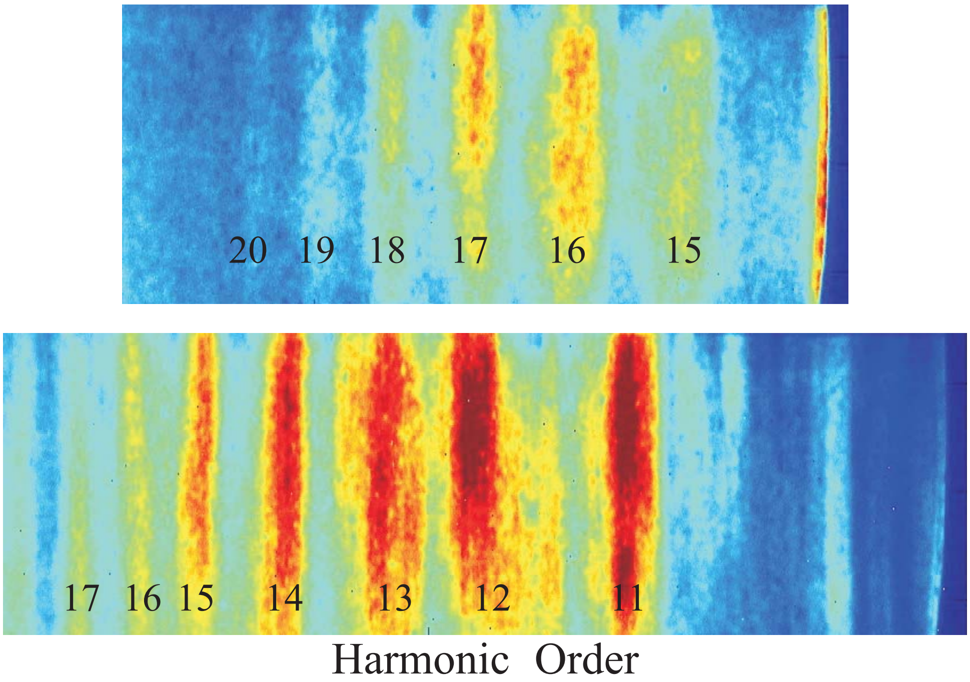

Figure 6.2: Two raw images of harmonic spectra recorded at different central wavelength using the McPherson grazing-incidence spectrometer (see Appendix B.3) in the divergent harmonic beam after the target (configuration (c) in figure 6.1). Harmonics up to the 20^{th} order corresponding to the highest harmonic expected from the CWE mechanism are clearly visible. Note that the color scaling is different in the two images.

emitted harmonic burst and can be seen as indirect proof of the fact that the emission is indeed confined to the duration of the 8 fs driving pulse it cannot explain the substructure on the individual harmonics. To visualize how strongly the spectra obtained with LWS10 are distorted figure 6.3 shows a vertically binned spectrum recorded with LWS10 (a) and in comparison to one obtained with ATLAS (b). While the ATLAS spectrum shows clean individual harmonics the LWS10 harmonics are much broader, as expected, but also appear to be split up into multiple separate peaks. Note that the peak visible between harmonics 15 and 16 in the ATLAS spectrum is not part of the harmonic spectrum but originates from the third diffraction order of a strong incoherent oxygen-line at 18 nm. In 6.3 (a) it is difficult to determine if the peak between H15 and H16 also originates from line radiation or whether this is actually part of the harmonic spectrum. It is important to state however that the observed line radiation was generally much weaker with the 8 fs driver which can be attributed to the significantly lower pulse energy, and thus energy deposition, in the target in this case.

The experimental observation of a distinct cutoff in the harmonic spectrum and the fringing of the individual harmonics is also backed by the results of 1D PIC-simulations.

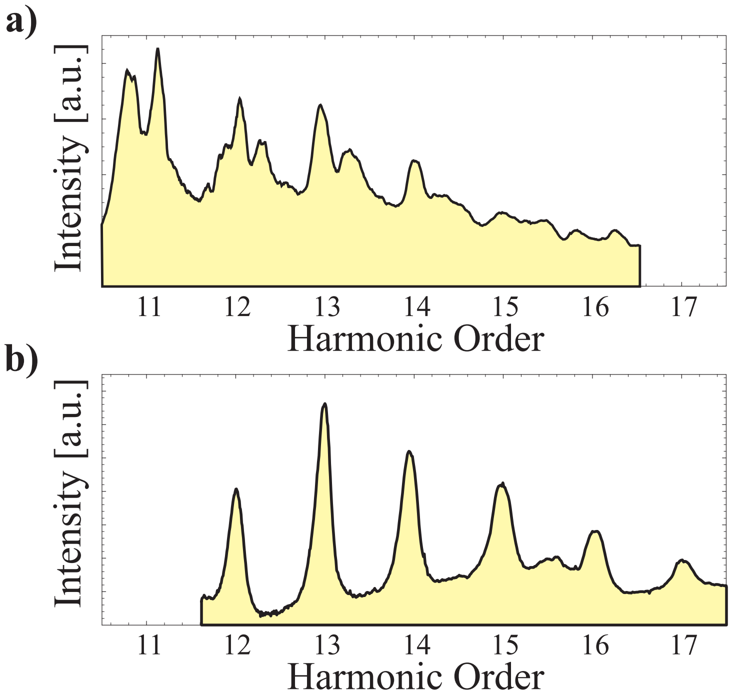

Figure 6.3: Comparison of a harmonic spectrum recorded with LWS10 (a) and ATLAS (b). The harmonics from LWS10 are significantly broader then those from ATLAS and are strongly structured. Note that the peak visible in between harmonics 15 and 16 in spectrum (b) is the third-order diffraction signal of a strong incoherent oxygen emission line at 18 nm.

Figure 6.4 shows the result of such a simulation which nicely reproduces the experimental observations. The simulation parameters where chosen to be an intensity of a_0=1.5, a pulse duration of 3 laser-cycles, an angle of incidence of 45°, p-polarization, a peak target density of n_{max}=200n_c and a linear pre-plasma ramp with a length of 0.2 λ_L. Note that the difference in cutoff harmonic between the simulation and the experiment is the result of the lower peak target density used in the simulation. Just like in the experiment the cutoff in the simulation coincides with the maximum plasma frequency supported by the target.

Beyond the mere observation of the fringing the simulation also helps to identify the origin of this effect. In principle, the fringes could be caused by the interference of harmonics generated by pre- and post-pulses a few laser-cycles before and after the main pulse. In LWS10 such pulses are known to exist and have been characterized via third-order interferometric autocorrelation [137]. However their intensity of a few percent of the peak intensity 12 fs before and after the main pulse should not lead to significant interference effects. In addition, the fact that distorted harmonics are observed in the simulation conducted with a perfect Gaussian pulse, i.e. without pre or post-pulses, in time helps to rule out this effect as a possible origin of the fringing of the individual

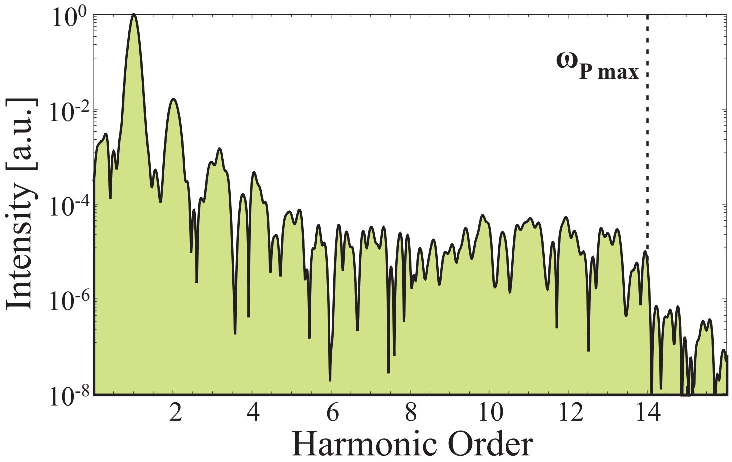

Figure 6.4: Harmonic spectrum obtained from a PIC simulation for a 3-cycle pulse. The simulation parameters where chosen to be an intensity of a_0=1.5, 45° AOI, a peak target density of n_{max}=200n_c and a linear pre-plasma ramp with a length of 0.2 λ_L. Like in the measurement the individual harmonics are strongly deformed and a clear cutoff is visible at the maximum plasma frequency. Simulation courtesy of S. Rykovanov

harmonics. The source of the distortions therefore has to be the result of the dynamics within the main pulse itself.

To find the origin of the structured harmonics it is necessary to look at the mechanism generating them in more detail. In CWE the individual as-bursts emitted from the target are generated by fast Brunel-electron bunches injected into the plasma [34]. The exact injection time of these electrons relative to a peak in the oscillating laser field is a function of the instantaneous laser intensity and thus not constant over the laser-pulse duration. This leads to the emission of an unequally spaced train of as-pulses, i.e. a train with a coherence time shorter than the duration of the harmonic emission. In other words there is a chirp on the individual harmonics (see Chapter 2.2.2). For pulses of 40 fs duration this leads to spectral broadening of the individual harmonics which has been observed experimentally and reported in several publications [34, 35]. In fact, the spectrum shown in figure 6.3 (b) is also broadened as a result of this effect. For the ATLAS laser this is studied in detail in Chapter 4 of this thesis where it is shown that the coherence time of the harmonic bursts generated with the ATLAS laser is indeed significantly shorter than the XUV-pulse duration.

However, while the unequal spacing is reported to be the origin of the spectral broadening in the publications mentioned above and experimental evidence is given these results allow only limited conclusions on the influence of unequal spacing in the case of very short driver pulses. For this reason model calculations have been conducted to address this question in more detail.

The model is based on the assumption that a series of individual as-pulses is emitted from the target with varying inter-pulse spacing, i.e. with chirp on each individual harmonic. The difficulty and at the same time the key to properly modeling the CWE harmonic emission is to find a good description of this harmonic chirp. Once a model is found the unequally spaced train of as-pulses can be described as the convolution of a single as-pulse $P(t)$ with an unequally spaced train of discrete delta functions with relative intensities given by a suitable envelope function $T(t)$. To obtain the spectrum $S(\omega)$ of the harmonic emission the convolution simply needs to be fourier-transformed to frequency-space. Here we can take advantage of the convolution-theorem [169]

$$S(\omega) = \mathfrak{FT}(P(t) \otimes T(t)) = \mathfrak{FT}(P(t)) \cdot \mathfrak{FT}(T(t)) \tag{6.1}$$

to simplify the calculation especially since the as-pulse can easily be described directly in frequency space.

For the model calculations presented here the single as-pulse is synthesized from a train of broad, equal-intensity, Gaussian harmonics ranging from harmonic order 11 to 18. In frequency-space it can be written in the form

$$P(\omega) = \sum_{18}^{n=11} \exp\left[-\left(\frac{\omega - n}{0.5}\right)^2\right], \tag{6.2}$$

where ω is given in multiples of the fundamental laser frequency and the value of 0.5 for the harmonic width was chosen as it results in the generation of a single pulse. For the sake of simplicity the phase across the spectrum of the pulse is assumed to be flat. Note that this simplification is valid and has been checked to have no influence on the resulting power spectrum as the atto-chirp, i.e. the chirp between the individual harmonics originating from harmonic generation inside a plasma gradient (see Section 2.2.2), varies only very slowly across each individual harmonic. If necessary to address a special question, however the atto-chirp can be incorporated into the model without problems.

As has been mentioned before the description of the unequal spacing is a little more tricky. To obtain a good approximation the emission times of the individual as-pulses have been extracted from a PIC-simulation conducted for a 15-cycle laser pulse (corresponding to the pulse duration of the ATLAS laser) with an $\mathrm{a_0}$=1.5 and a peak target density of $\mathrm{n_{max}}$=400$\mathrm{n_c}$ (all other parameters where the same as in the simulation shown in Figure 6.4) as has also been done in [35]. For the model calculation deviation $D(t)$ of the spacing from the periodicity of the driving laser pulse was approximated by a function of the form

$$D(t) = \left(\frac{t}{a}\right)^4 \tag{6.3}$$

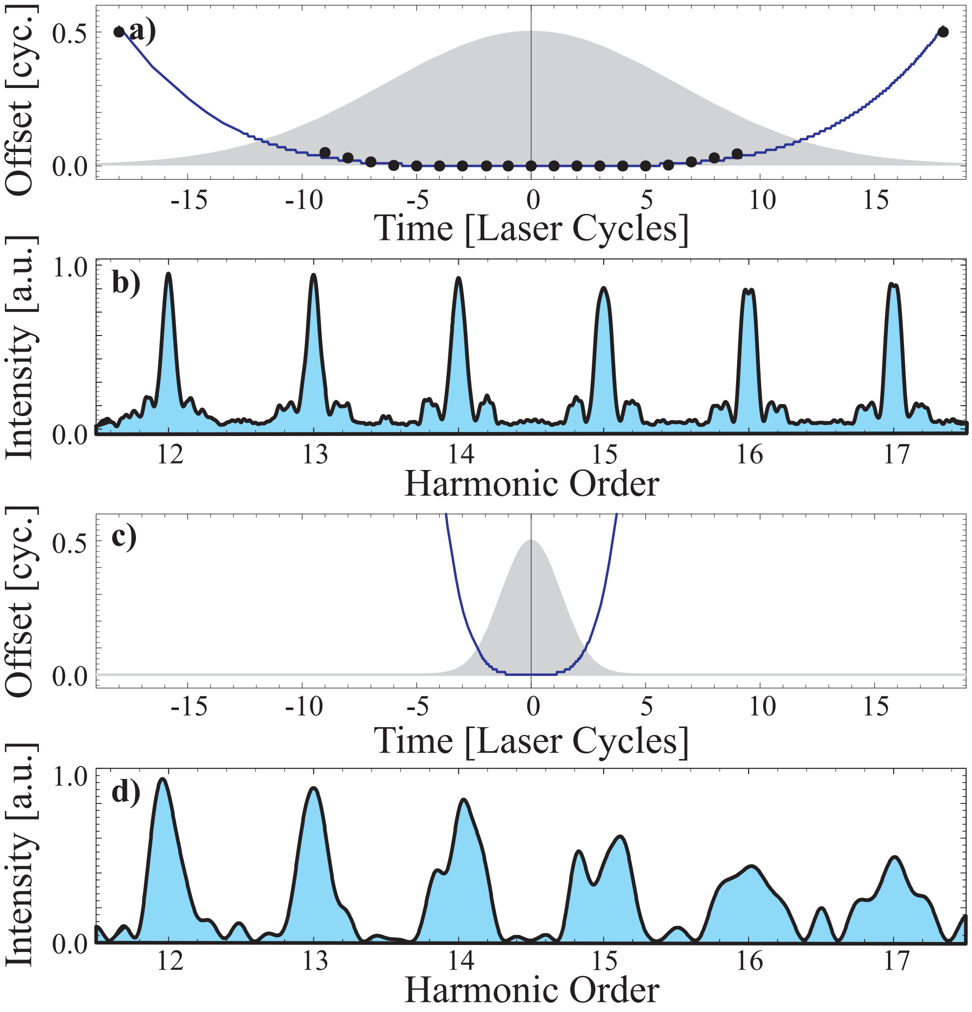

Figure 6.5: Model calculation of the harmonic spectra generated as a result of the unequally spaced emission of the individual as-pulses for (a) and (b) a 15-cycle and (c) and (d) a 3-cycle driving pulse. The deviation of the as-pulse emission times from the period of the driving laser is shown in (a) and (c). The functional dependence of the unequal spacing used in the model (blue curve) is obtained by fitting a fourth-order function to the individual emission times extracted from a PIC-simulation (black dots). The resulting harmonic spectra from the unequally spaced emission are shown in (b) and (d). Substructures are clearly visible on the individual harmonics for the short laser pulse.

where a is determined by fitting the function to the data points, t is given in laser cycles and $t = 0$ is the point in time corresponding to the peak of the driving laser pulse. The data points (black dots), the fitted function $D(t)$ (blue line) and the envelope of the 15-cycle driving pulse are depicted in figure 6.5 (a).

To further support the model analytical calculations of the trajectories of individual electrons in the field of the laser pulse similar to those conducted by Corkum et al. [9] for harmonics from noble gases where conducted. To adapt the model to surface harmonics relativistic effects where added to the calculation and the field driving the electrons was assumed to be the laser electric field outside and zero inside the target. When tracing only those electrons that actually return to the target surface and propagating them through the pre-plasma gradient bunching and unequal spacing is observed. Preliminary results show the spacing derived from this model calculation is in good agreement with the values extracted from the PIC-simulation further supporting the validity of the model assumption made for $D(t)$ (equation 6.3). The analytical model for the spacing of the as-pulses is also presented in more detail in [62, 67].

Using $D(t)$ to synthesize an unequally spaced train of delta-spikes it is now possible to determine the harmonic spectrum expected for CWE harmonics generated with the ATLAS laser by solving equation 6.1. The result of the model calculation is shown in figure 6.5 (b). Compared to the spectrum expected for an equally spaced train the harmonics are significantly broadened ($\Delta\omega/\omega = 0.15 \pm 0.05$ for the unequally spaced train compared to $\Delta\omega/\omega = 0.04$ in the case of equal spacing) and some energy is located in the side-lobes of the individual harmonics. The shape of the main harmonic peak, however, remains close to Gaussian. Despite the simplicity of the model and the assumptions made this result is also in good agreement with the experimental findings (Chapter 4 and especially Figure 6.5 (b)). While the side-lobes visible in the model calculation are not observed in the measurement which may well be the consequence of incoherent background radiation (especially the various diffraction orders of the 18 nm Oxygen-line) masking this effect there is a discrepancy between the harmonic width of $\Delta\omega/\omega = 0.25 \pm 0.05$ in the measurement and the value of the model calculation. Note however that the extraction of the exact line-width from a measurement with an imaging spectrometer is difficult as many effects like, for example, imperfect imaging can lead to an additional broadening of the harmonics observed. To overcome the problem of unfolding such effects from the measurement, which is very difficult anyway as quantifying the contributions is nearly impossible, it is instructive to determine the temporal coherence of the emitted radiation and extract the expected line-width from that measurement as has been described in chapter 4 of this thesis. Note that this analysis yielding a harmonic width of $\Delta\omega/\omega = 0.10 \pm 0.03$ (see chapter 4) which is in much better agreement with the model calculation than the value extracted from figure 6.3.

Based on the good results achieved with the model for long pulses it is now also possible to investigate the effect of unequal spacing in the case of very short 3-cycle driver pulses. For this purpose equation 6.3 needs to be adapted to incorporate the shorter pulse duration. As the peak intensity used in the simulation from which the unequal spacing is derived is very close to the actual focused intensity in the LWS10 experiment this is

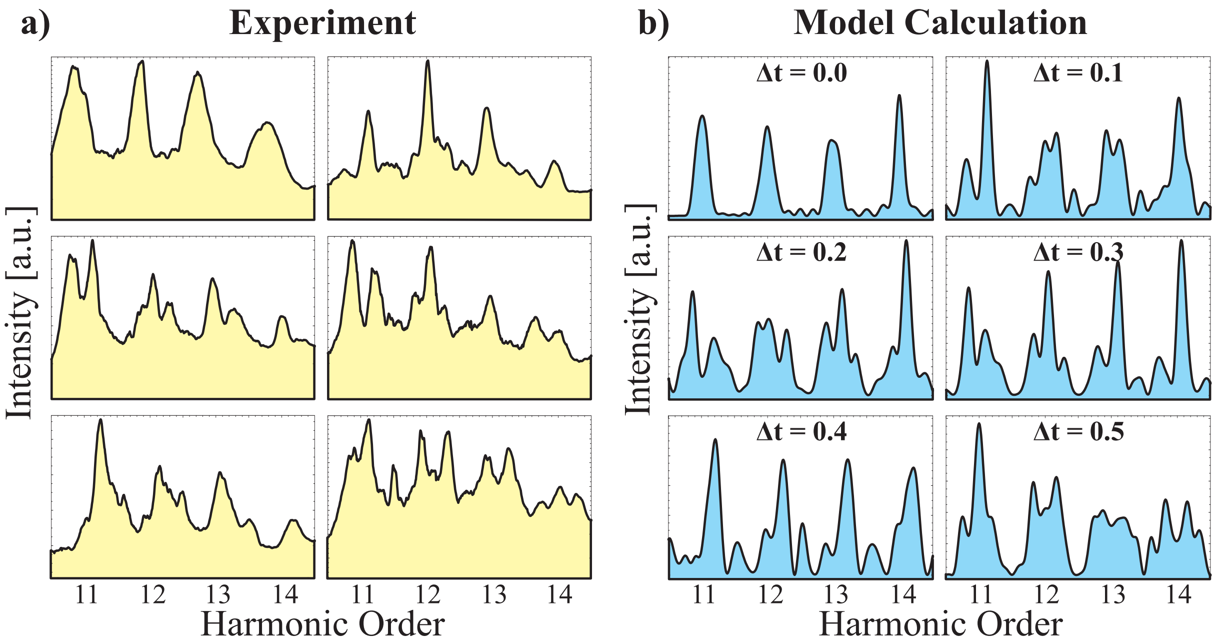

Figure 6.6: (a) A series of measured harmonic spectra obtained under fixed experimental conditions. The harmonics vary significantly in shape from shot to shot. (b) Influence of the carrier-envelope (CE) phase on the generated harmonic spectra obtained from model calculations for a 3-cycle laser pulse. Δt gives the offset between the central as-pulse and the peak of the envelope in units of laser periods. The shapes of the individual harmonics are found to depend strongly on the CE-phase.

achieved by keeping the functional dependence of the deviation from equal spacing as a function of laser intensity constant and simply rescaling $D(t)$ to account for the shorter pulses. The resulting deviation from equal spacing used in the model is shown together with the envelope of the 3-cycle pulse in figure 6.5 (c) and is again in good agreement with the calculated electron trajectories [62, 67]. The harmonic spectrum resulting from the calculation is depicted in (d). In the short-pulse case the harmonics are strongly modulated and deviate significantly from the Gaussian shape expected for an equally spaced train. While it is difficult to compare a single-shot LWS10 spectrum directly with the model calculation owing to the strong fluctuations this still proves that the CWE-mechanism itself is capable of generating harmonic spectra with significantly distorted harmonics. This in turn means that the observation of such fringed harmonic spectra is a strong indication that the harmonic emission in the experiments with LWS10 is indeed confined to the duration of the driving laser confirming that we have taken a significant step toward the generation of single as-pulses.

However, the model is capable of more than just qualitatively reproducing distorted harmonics. As has been mentioned before the individual harmonic spectra recorded with

LWS10 exhibit strong shot-to-shot fluctuations. To illustrate this figure 6.6 (a) shows six harmonic spectra recorded with LWS10 under exactly the same experimental conditions. The only real similarity between the individual shots is the harmonic structure of the recorded XUV-radiation. The shape of the individual harmonics varies strongly from gaussian-like on the top left to completely fringed on the bottom right. Since nothing was changed in the setup between the shots the fluctuations have to originate from variations of the individual laser pulses used to generate the harmonics. The pulse energy and duration are known to vary slightly from shot to shot (this was investigated first), and model calculations show that these cannot be the origin of the strong fluctuations observed. There is, however, another pulse parameter which is of no importance for longer laser pulses but is known to significantly influence the dynamics of laser-matter interactions in the few-cycle regime: The carrier-envelope phase (CEP) [29], i.e. the relative phase between the rapidly oscillating electric field and the envelope of the laser pulse. To analyze the influence of CEP-variations on the harmonic spectrum with the model presented above a variable offset between the train of delta-spikes representing the as-pulses and the envelope function was introduced. A series of spectra obtained with variable CEP but otherwise constant simulation parameters is shown in figure 6.6 (b). Interestingly the model spectra qualitatively reproduce many features also observed in the experimental data. To illustrate this the experimental spectra where sorted to match model spectra with similar harmonic structure. Especially in the top-left and the middle- and lower-right spectra the similarities are striking. While the model is obviously not precise enough to actually determine the CEP from the simulations the similarities suggest that the fluctuating spectra are indeed the result of this effect. This is further supported by the fact that CEP variations have practically no influence on the model spectra of the 15-cycle pulse as one would expect which is again in good agreement with the observation that the spectra generated with ATLAS are very reproducible.

Finally, however, it is important to emphasize that this is strong evidence for the observation of CEP-effects in harmonic generation with LWS10 but no definitive proof. To prove the relation and perhaps even find rules for how to estimate the CEP from the harmonic spectra LWS10 would have to be phase-stabilized which is technologically very challenging and has never been achieved for such a large laser-system or the CE-phase would at least have to be recorded for every shot with a single-shot phase-meter [170] to allow a correlation analysis.

6.2.2 Polarization Dependence

As has been mentioned before a second integral part of the experimental results obtained with LWS10 is the dependence of harmonic emission on the laser polarization. To the best of my knowledge such studies have so far been limited to purely p- or s-polarized beams (for example in [59]). Here I present scans of the polarization from s- to p- as well as from linear to circular polarization allowing interesting new insight into the CWE-mechanism. However, beyond that the results could be used to design a polarization gating setup with which the CWE-emission of LWS10 could be further confined to a window of only a fraction of the driving laser duration. The experimental data is of special interest in this case as even theoretical studies of polarization gating in SHHG have so far been limited to ROM-harmonics [38, 83, 84].

The polarization was varied using broad-band achromatic $\lambda/2$- and $\lambda/4$-plates placed in the amplified but uncompressed LWS10 beam taking advantage of the fact that the LWS10 compressor is polarization insensitive. The details of the setup can be found in section 6.1. For each polarization a series of single-shot spectra where recorded and analyzed. Figure 6.7 shows the XUV-intensity emitted into harmonics 11 to 14 for different laser polarizations normalized to the signal obtained with a purely p-polarized beam. The error bars correspond to the standard deviation of the XUV-signals measured for each wave-plate setting. Note, that the polarization dependence of each individual harmonic (11 to 14) was also analyzed and found to have the same functional dependence on laser polarization as the spectrally integrated signal and is therefore omitted in the plots for clarity.

As one would expect the harmonic intensity is highest when the driving laser is p-polarized and zero when the polarization is s. This is a direct consequence of the CWE-mechanism as it relies on the acceleration of electrons by the electric field component perpendicular to the target surface. Note that for ROM this would be substantially different, as in that case s-polarization will generate harmonics but circular polarization would not (see Chapter 2). While the behavior in the limiting cases of pure s- and p-polarization was to be expected the functional dependence of the harmonic intensity is surprising. Previous work on CWE harmonics [34, 63] has shown that the intensity dependence of the harmonic emission for a p-polarized driver close to linear and lies somewhere in the range of

$$I_{\mathrm{XUV}} \propto I_{\mathrm{L}}^{0.5-1} = \left|\vec{E}_{\mathrm{L}}\right|^{1-2} \tag{6.4}$$

in the previous publications. If this scaling was also valid for varying polarization, i.e. if in the case of changing polarization the harmonics where simply only generated by the p-polarized component of the driving pulse, the observed harmonic intensities should follow the scaling shown above. If this was the case the data points in figure 6.7 should lie inside the gray shaded areas covering the range of intensity dependences given in equation 6.4. Experimentally, however, a much stronger dependence of the XUV-intensity on the polarization is observed. This means that in addition to the reduction of the electric field

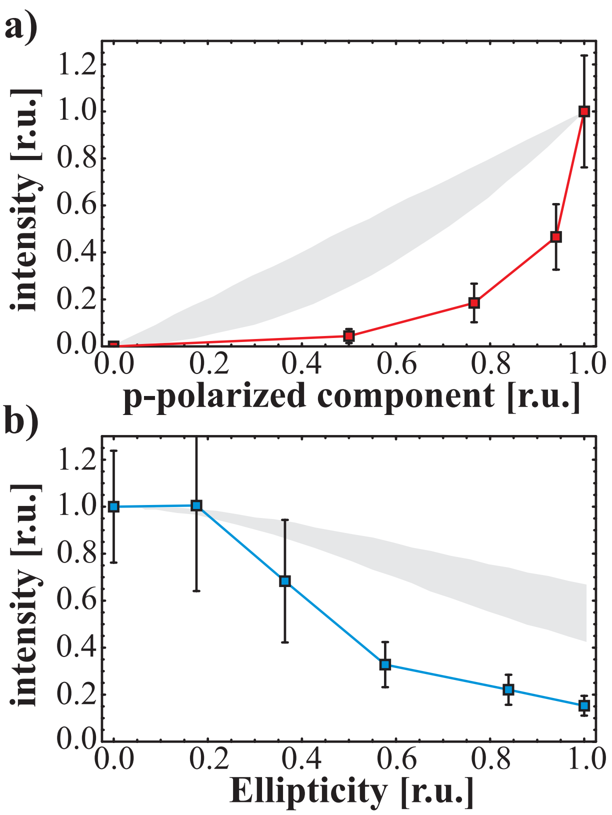

Figure 6.7: Dependence of the XUV-intensity emitted into harmonics 11 to 14 as a function of varying driving laser polarization for (a) the transition from s to p and (b) linear to circular. The intensity is normalized to the signal obtained with a purely p-polarized driving pulse and each data point is averaged over several shots. The p-polarized component of the laser beam in (a) is defined as the ratio between the electric field in p-polarization direction and the total electric field while the ellipticity in (b) gives the ratio between the electric field components along the ordinary and extraordinary axis of the wave-plate. The gray shaded area shows the range in which the data would be expected if it followed the simple scaling shown in equation 6.4 (see text).

component perpendicular to the target surface other factors have to contribute to the reduction of the XUV-signal. The main difference between a simple intensity reduction and a polarization modification lies in the trajectories of the electrons. In the case of linear polarization the trajectories will be tilted with respect to the target normal resulting in a longer effective pre-plasma ramp. This, in turn, has been shown to reduce the harmonic generation efficiency significantly in earlier experiments [51]. For circular polarization a similar effect should occur as the trajectories of the electrons injected into the target are not linear anymore. Electrons extracted from the plasma at different times will not only return at different times but also under different angles and spread out laterally. This will lead to reduced bunching of the electrons and less efficient plasma-wave and thus harmonic generation. It is important to emphasize however that more detailed theoretical analysis is necessary to place this interpretation on firmer ground. For this purpose detailed PIC-simulations are planned to analyze the electron trajectories in the case of non-perpendicular polarization. Based on the observation that CWE is actually suppressed when the pre-plasma gradient becomes too short in very high contrast interactions [91] one could furthermore devise an experiment in which the polarization is varied under such experimental conditions. If the electrons indeed experience a longer effective pre-plasma this could lead to increased harmonic emission for beams with a polarization between p and s.

Independently of the exact origin of the steep drop in harmonic signal with varying intensity the finding is encouraging in the context of a possible polarization gating experiment in the CWE regime, as a strong polarization dependence will lead to a narrow gate. The simplest possible gating setup which has also already been implemented successfully in gas-harmonic generation [11] is depicted in figure 6.8 (a) for a pulse with a duration of 8 fs. The linearly polarized original pulse (black) is split into two equal intensity parts with perpendicular polarization in a birefringent plate the thickness of which is designed to introduce a delay of three laser cycles between the pulses propagating along the ordinary and the extraordinary axis of the crystal. The resulting pulse is still linearly polarized but the polarization direction is rotated by 90 degrees over its duration (red pulse in Figure 6.8 (a)). Finally a quarter-wave plate is placed in the beam and aligned such that it rotates the polarization of the leading and the trailing edge of the pulse while leaving the central part unchanged (blue pulse). While the blue pulse is the one desired for gating in gas-harmonics [11, 168] and also for ROM [38] this is not so obvious for CWE since the decay of harmonic signal with laser ellipticity is not very strong. It may well be beneficial to use the pulse after the delay plate directly. To analyze this in more detail the x- and y-components of the electric field of the pulses after the delay-plate and the $\lambda/4$-plate are shown in Figures 6.8 (b) and (d) respectively. In addition plots (c) and (e) show the p-polarized component of the pulse after the delay plate and the ellipticity of the final pulse. Note that the definitions of these parameters are the same as in Figure 6.7 to simplify the comparison.

From the comparison of the measured data and the calculated pulse shapes one can immediately see that there is one big disadvantage in gating coherent wake emission: Unlike in gas harmonics and ROM the harmonic generation efficiency does not drop to zero in the wings of the pulse. Nevertheless, owing to the strong decrease in harmonic generation efficiency for small deviations from p-polarization, a reduction of the emission time by almost a factor of two should be achievable when the pulse after the delay plate, i.e. the one with rotating linear polarization, is used. This can, in combination with a

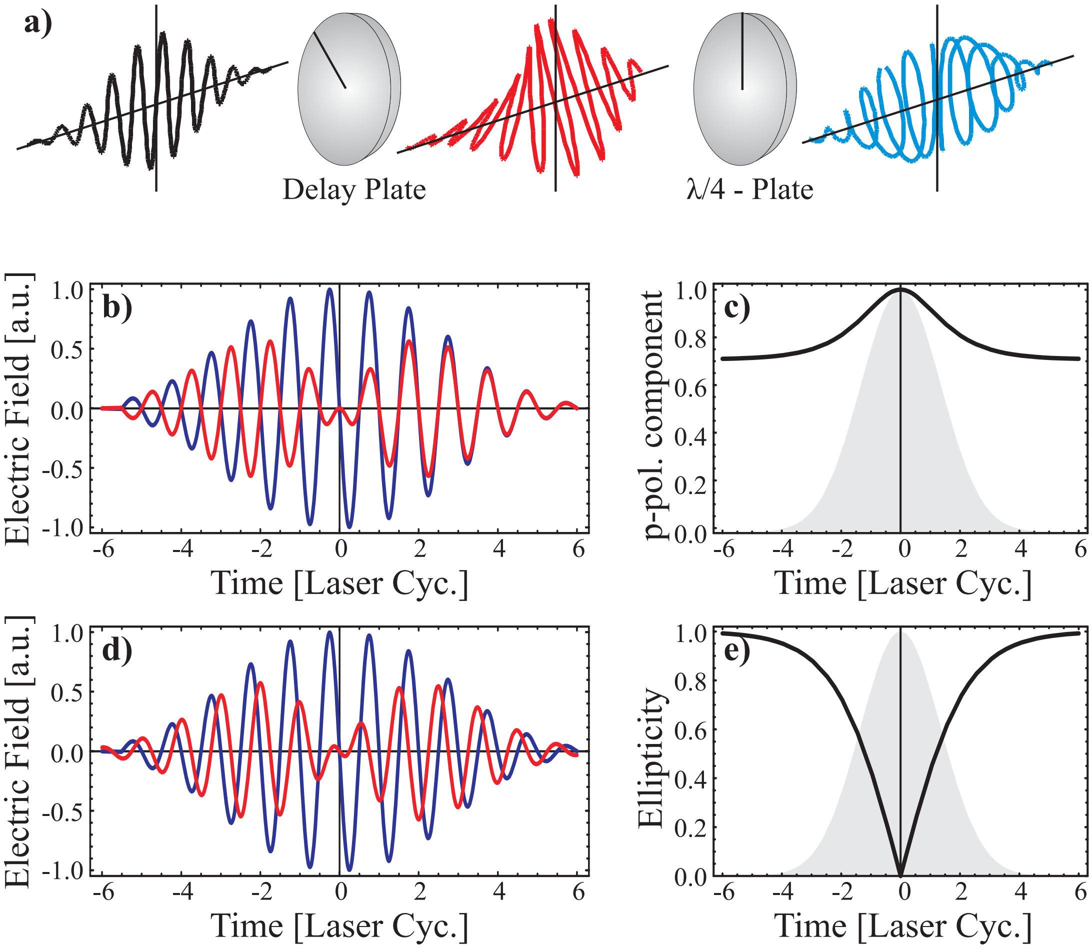

Figure 6.8: (a) Schematic drawing of the concept of polarization gating [11, 38]. A linearly polarized pulse (black) is split into two equal intensity components in a birefringent delay plate. For a plate with delay of 3 λ this results in the red pulse. Finally a $\lambda/4$-plate is used to synthesize a pulse with a polarization changing from circular to linear and back to circular (blue). To analyze the properties of the gated pulse in more detail (b) and (d) show the p- (blue) and s- polarized component (red) of the pulse electric field after the delay plate and the $\lambda/4$-plate respectively. In addition (c) shows the p-polarized component of the field shown in (b) and (e) depicts the time-dependent ellipticity of the field in (d). Axis definitions see figure 6.7.

single-shot CEP measurement, help to understand the origin of harmonic fringing and give additional valuable insight into the dynamics of the CWE process. Finally it is important to mention that a gating setup implemented and tested in a CWE experiment can also be used without modification to gate ROM emission when the necessary ultra-high contrast driver-pulses become available.

6.3 Summary

The results presented in this chapter constitute the first demonstration of high harmonic generation from solid surfaces with few-cycle driver pulses. They prove that new state-of-the-art OPCPA-based systems offer a promising route toward the generation of ultra-intense single as-pulses and simultaneously improve the understanding of the electron dynamics in the harmonic emission process. Two effects have been studied in detail in this chapter. The appearance of distinct sub-structures on the individual harmonics and the dependence of harmonic emission on the driving laser polarization.

Owing to the limited contrast of the current LWS10 pulses ROM-harmonic generation was not observed despite the relativistic laser intensity and the harmonic emission was thus limited to orders below 21 owing to the properties of the fused silica target used. The origin of the distortions of the observed harmonics (figure 6.3) is therefore a direct consequence of the electron dynamics in the CWE process for 8 fs driving pulses. While it is well known that the unequal spacing of the individual emitted as-pulses, a result of the fact that CWE harmonics are generated via plasma waves excited by bunches of Brunel-electrons penetrating the target, leads to a broadening of the emitted harmonics for 40 fs driving pulses [34, 35] its influence on even shorter pulses has not been studied previously. Based on a model for the unequal spacing derived both from PIC-simulations and an analytical calculation of individual electron trajectories I demonstrate that the distorted harmonics are indeed a natural consequence of the shortness of the driving laser pulse. In turn this is strong (albeit indirect) proof that the harmonic emission was indeed confined to a few-cycle window constituting an important step toward the generation of single as-pulses. Beyond this the model calculations also help to understand the strong fluctuations observed from shot-to-shot in the experiments. They show that CEP variations can lead to significant modification of the harmonic spectrum and the modeled spectra show good qualitative agreement with the measured ones (figure 6.6). However additional measurements with simultaneous detection of the harmonic spectrum and the CEP are necessary to prove the connection.

In a second set of measurements the polarization dependence of CWE-harmonics has been studied systematically (figure 6.7). The intensity of harmonic emission is shown to decay strongly when the polarization is changed from p and no harmonics are observed for s-polarization as one would expect since the origin of CWE-harmonics are fast electrons accelerated in the electric field component perpendicular to the target surface. Interestingly, however, the decay of the harmonic signal is found to be stronger than the decrease of the p-polarized laser component. This can be attributed to a change in the electron trajectories leading to a longer effective pre-plasma scale-length and subsequently stronger harmonic-signal decay. The results show that it should, in principle, be possible to further confine the emission of CWE to a fraction of the driving laser duration using polarization gating. However there is one problem which cannot be overcome and which excludes the possibility of generating a single attosecond CWE-pulse: Owing to the dynamics of the CWE process it is not possible to generate a driving laser pulse for which the harmonic generation efficiency is zero in the wings as a result of polarization manipulation. Nevertheless, as a gating setup prepared for the use in the CWE-regime can also be used to gate ROM-harmonics once sufficiently high-quality driver pulses are available the design and testing of such a setup with CWE may be well worth the effort.

Chapter 7

Conclusions and Outlook

Throughout this thesis a set of experiments have been discussed addressing various aspects of high harmonic generation from solid-density targets. They advance the understanding of the fundamental processes of SHHG and also represent a step towards the grand goal of realizing a source of single as-pulses with unprecedented intensity which will expand the scope of *Attoscience* to experiments currently not accessible owing to the low number of XUV-photons in conventional gas harmonic sources [29]. The experiments where conducted using three different laser systems and experimental setups specifically designed to address various fundamental questions.

In a first set of measurements the temporal structure of the harmonic emission from solid targets was addressed using two different methods: A nonlinear second-order autocorrelation and a temporal coherence measurement. The autocorrelation reveals that the harmonic burst generated via the CWE mechanism is of the same duration as the driving laser pulse which is consistent with previous findings that CWE scales roughly linearly with laser intensity. Additionally a finer scan reveals a distinct periodic substructure in the harmonic emission at the frequency of the driving laser proving that the emitted XUV radiation is indeed phase-locked resulting in a train of as-pulses [63, 69]. This is the first conclusive proof of this long predicted feature of solid-target harmonics and constitutes an integral step on the route to a novel source of as-pulses. In addition, a temporal coherence measurement of a range of harmonics was conducted to test a simpler, albeit indirect, method to obtain information about the temporal structure of the harmonic emission. This method allows conclusions about the sub-cycle dynamics of the harmonic generation process [67] and is much more precise than a simple harmonic line-width measurement. The coherence time obtained in this measurement is found to be significantly shorter than the duration of the emitted XUV burst. The discrepancy between pulse duration and coherence time observed is shown to be the result of an inherent harmonic chirp [35] resulting from the unequal spacing of the individual as-bursts emitted via the

CWE process. It is important to note, however, that the phase of ROM emission is expected to be flat so that the method for the coherence measurement presented in this thesis may well be sufficient to analyze the XUV-pulse duration in future systems.

The second experiment featured in this thesis was conducted using the ASTRA laser facility at the Rutherford Appleton Laboratory in the UK and addressed a different aspect of SHHG. The experimental setup included a plasma mirror to enhance the contrast of the laser pulses before the interaction with the main target. With this method ROM-harmonics extending up to the relativistic cutoff [30] were produced. The measurements show that the generated harmonics are emitted into a narrow, near-diffraction-limited cone with a constant divergence observed for all harmonics. In addition it was found that that a target roughness on the scale of the skin-depth does not adversely influence the generation process (despite the fact that this roughness is on the scale of the wavelength of the highest observed harmonics.) [64]. The constant divergence is shown to be the result of harmonic generation on a curved surface resulting from denting of the target in the focus of the intense laser beam. Interestingly this also implies that the individual harmonics have propagated through a focus after their generation in which, under certain conditions, extreme intensities could be reached [32]. In a second measurement the properties of the fundamental and the second harmonic emitted from the target where characterized. Significant spatial filtering of the fundamental and the generation of a near-Gaussian second harmonic beam are observed [68] and demonstrate that the interaction of relativistic laser pulses with solid targets may be a route to overcome problems with conventional spatial filters and frequency doubling setups in the high-power laser systems envisioned for the future [103, 154, 155].

In contrast to the first two experimental campaigns conducted with 40 to 50 fs duration laser pulses the third set of experiments presented focuses on the generation of harmonics using the novel 8 fs LWS10 laser system [123]. The development of such laser systems and their subsequent use for harmonic generation is an integral step towards the efficient generation of single as-pulses as it allows to confine the harmonic generation to a few and ultimately a single oscillation of the electric field. The experiments demonstrate the generation of harmonics up to the CWE-cutoff and also allow interesting insight into the harmonic generation process itself. The individual harmonics are found to be significantly distorted and fluctuate strongly in shape from shot to shot. Model calculations show that this effect can be well explained by the expected unequal spacing of the harmonic emission (also observed in the coherence measurement) and shot-to-shot variations of the carrier-envelope phase [62].

While all of these results in themselves advance our understanding of the physical processes underlying the high harmonic generation from solid-density plasmas the integral next step towards a single as-pulse source will be to combine all the aspects addressed in this thesis in one experiment: The generation of a diffraction limited beam of relativistic harmonics with a sub-10-fs driver laser system and its subsequent temporal characterization. To achieve this goal several improvements have to be implemented in the currently available system and some new technologies need to be developed.

The first step to be taken is the demonstration of the generation of relativistic harmonics using a few-cycle driver laser. The experiments with the ASTRA system presented in this thesis have illustrated the absolute necessity of a very good contrast in the driving pulse to achieve this goal. For this reason the improvement of the contrast of the existing laser systems at MPQ is currently pursued. To achieve this a new high-contrast front-end will be installed on ATLAS and the LWS system will be equipped with an XPW [131–133] in the laser chain to enhance the contrast of its front-end. In addition the implementation of a plasma mirror [77, 79, 160] is planned on both systems. With all these measures in place the generation of relativistic harmonics will likely be possible with both systems.

While this in itself will produce a wealth of new results a key concern, especially when a plasma mirror is used, is the number of shots that can be taken on one single target as this limits the scope of possible applications. Currently any measurement has to be terminated when the available target is used up as the vacuum chamber needs to be vented for target exchange resulting in the loss of the alignment of the experiment. To overcome this problem the investigation of alternative targets needs to be pursued. While tape targets will possibly be used in the near future the ultimate goal would be the development of a liquid-jet suitable for application both as target and as plasma mirror. despite the fact that this is technologically challenging it may well be possible and would allow the accumulation of unlimited numbers of shots alleviating one of the most severe limitations of a SHHG as-pulse source. In addition the implementation of special pre-dented targets may lead to an increase in intensity in the harmonic focus after the target [66] and may even allow specialized experiments approaching the Schwinger limit [32]. Experiments with ultra-thin targets can also point the way towards novel generation mechanisms for single as-pulses [171].

Finally a lot of improvement over the current setup is also possible in the XUV-beamline system transporting the generated XUV radiation to an envisioned experimental site. Especially the implementation of grazing incidence optics an specialized high-reflectivity coatings will allow focused intensities orders of magnitudes higher than those currently achieved in future applications [70]. On the short scale this is absolutely necessary to explore, for example, alternate two photon transitions for the XUV-autocorrelation of shorter XUV pulses and for the implementation of the attosecond streak-camera. On a longer run concepts developed in the near future are expected to form the backbone of the envisioned as-beamlines at the ELI facility [154].

All in all the investigation of high harmonic generation has taken a big step forward over the past 5 years and has opened the door towards a new an extremely powerful tool for experiments with attosecond resolution. Especially the high conversion efficiency and the absence of a limitation in applicable laser intensity will allow the reproducible generation of as-pulses with unprecedented energies in the near future. While a series of technological challenges are still to be overcome I am confident that these will not stop SHHG from becoming a very powerful tool for *Attoscience* experiments in the years to come.

Appendix A

The Plasma Mirror

For the generation of high harmonics from the interaction of high intensity laser pulses with solid density targets it is of utmost importance that the main laser pulse interacts with a steep plasma gradient and not a long low-density pre-plasma. To achieve this the intensity of any pre-pulses or pedestals has to be suppressed below the plasma formation threshold of the solid target. This restriction becomes all the more stringent the higher the focused intensity of the main pulse on the target gets. Several methods for contrast enhancement of high-power lasers are currently available and in use in state-of-the-art systems. Pockels cells can suppress pre-pulses on the ns-scale and more advanced concepts using saturable absorbers [172, 173] or cross-polarized wave generation (XPW) [131–133] are capable of cleaning pulses up to several tens of picoseconds before the main pulse. However, the only systems capable of cleaning pulses all the way up to the foot of the main pulse and thus enabling real ultra-high contrast interactions are plasma mirrors [77–79, 157–161]. In fact, a plasma mirror is the key component without which all the results presented in chapter 5 of this thesis would have been impossible to achieve. For this reason the concept and the working principle of a plasma mirror (PM) shall be introduced in some detail in this appendix.

To understand the operating principle of a PM it is important to look at the features of a typical fs-laser pulse first. The main pulse usually has some wings on a picosecond time-scale owing to imperfect compression of the amplified spectrum and sits on a long, ns-scale pedestal the origin of which is amplified spontaneous emission (ASE) or parametric superfluorescence depending on whether laser- or optical parametric amplification is used. Furthermore the main pulse is usually accompanied by a series of pre- and post-pulses originating, for example, from leakage from regenerative amplifiers and internal reflections in optics. A schematic of such a typical laser pulse is shown in figure A.1. While post-pulses and the part of the pedestal after the main pulse are generally of little concern in a high-intensity laser–solid interaction the components in front of the main pulse are

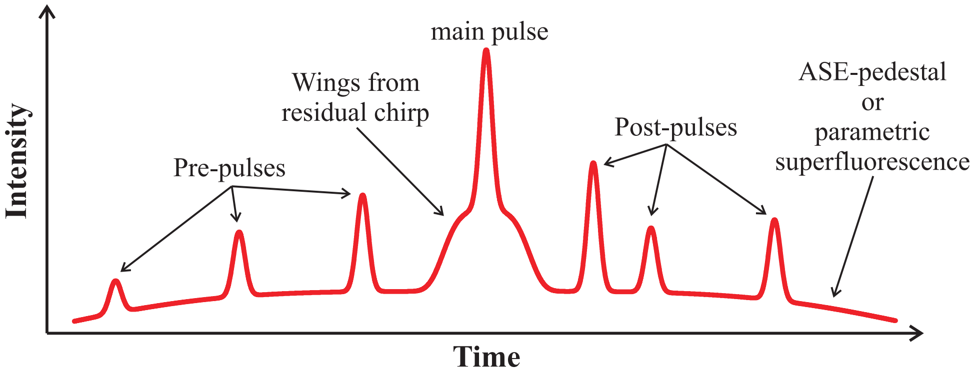

Figure A.1: Schematic drawing showing the typical features of a femtosecond high-power laser pulse. The main pulse sits on top of a long pedestal and is accompanied by a series of pre- and post-pulses. Imperfect compression of the pulse results in wings close to the main peak. Typical contrast rations are 1:10^6-10^8 for the pedestal, 1:10^2-10^6 for the pre- and post-pulses and 1:10^4-10^6 for the wings.

the ones that need to be suppressed. The wings owing to imperfect compression pose a special problem here since they are only present after the final compression of the pulse where none of the other methods for contrast enhancement (Pockels cells, XPW, etc.) can be applied owing to damage issues in the optical components.

The operating principle of a plasma mirror is actually quite simple. The laser pulse is incident onto a transparent target with a peak focused intensity such that the pedestal and the pre-pulses are transmitted through the target while the leading edge of the main pulse rapidly ionizes the solid target forming a reflecting surface off which the main pulse is reflected (see figure A.2). The feasibility of this approach was first demonstrated by Kapteyn et al. [160]. The contrast enhancement CE achievable from a plasma mirror can be calculated using the formula

$$CE = \frac{R_{\text{Plasma}}}{R_{\text{C}}} \tag{A.1}$$

where $R_{\text{Plasma}}$and R_{C} are the reflectivity of the plasma and the cold, i.e. unionized, substrate respectively. Thus, using anti-reflection coated substrates or an angle of incidence close to Brewsters angle, contrast enhancements on the order of 100 are possible and have been demonstrated [77] from a single PM.

However, while the concept of the PM is rather simple, it will only operate properly when the plasma mirror surface is still steep allowing a high-quality specular reflection when the peak of the pulse interacts with it. The ionization must therefore occur as late as possible to prevent plasma expansion and the formation of a long scale-length pre-plasma. B. Dromey et al. give a condition which has to be fulfilled to allow specular reflection

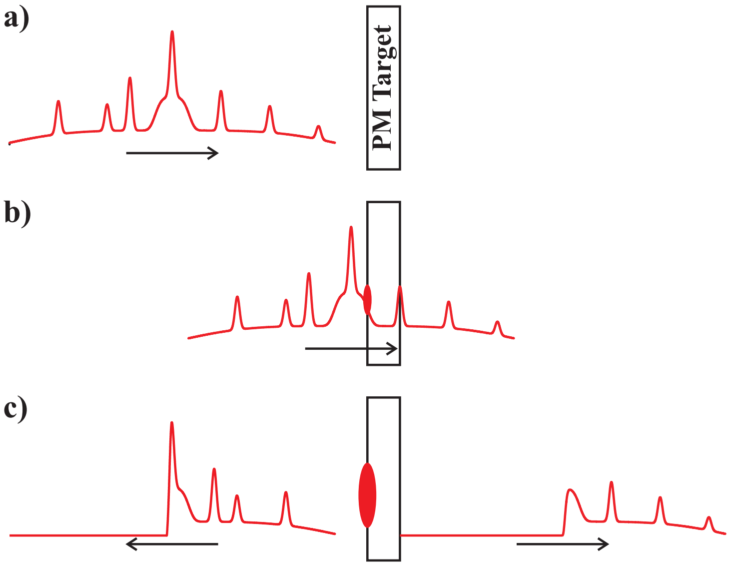

Figure A.2: Illustration of the operating principle of a plasma mirror. (a) The laser pulse is incident onto the plasma mirror from the left. (b) The pedestal and the pre-pulses are transmitted through the target before the main pulse rapidly ionizes the surface on its rising edge. (c) The main pulse is reflected off the plasma resulting in a pulse with improved contrast.

from the PM [77]:

$$c_s \Delta t < \lambda_L. \tag{A.2}$$

Here c_s is the sound speed of the expanding plasma surface and Δt is the time between the ionization of the target and the arrival of the main pulse. For typical expansion velocities of a few times 10^7 $cm\ s^{-1}$ derived from the blue-shift of the laser spectrum reflected off the PM [77] Δt will be on the order of a few picoseconds. In practice this means that the intensity of the pulse on the PM must not be higher than a few times 10^{16} $W\ cm^{-2}$ for propper operation [77–79] and should not be much smaller than 10^{15} $W\ cm^{-2}$ to ensure high reflectivity. For current high-power laser systems this means that the plasma mirror cannot be operated in the focus of the laser beam, which would be beneficial because the PM acts like a spatial filter under these conditions [79, 159], as this would require focusing optics with focal lengths on the order of 10 m. Instead it has to be placed in the near-field of the focusing (or expanding) beam which may result in a distortion of the wave-front of the reflected pulse as a result of the inhomogeneous intensity distribution in the beam. Fortunately B. Dromey et al. [77] have shown that the beam profile of the pulse is only slightly distorted and that the beam is still nicely focusable after reflection off the PM despite these distortions. Nevertheless it is important to monitor the reflected near- and far-field of the PM closely under these delicate operating conditions.

It remains to be said that the concept of the PM is not limited to a single reflection or pulses of tens of femtoseconds in duration. A double-PM setup has recently been studied in detail by T. Wittmann et al. [158] and was successfully applied in a series of experiments [57, 58, 61] for an even bigger contrast enhancement. Y. Nomura et al. have shown that the concept of the PM can also be applied to sub-10-fs pulses at kHz repetition rates with efficiencies larger than 50 percent [79].

Last but not least it should also be pointed out that the experiments presented in section 5.2 of this thesis do not only apply a conventional PM to generate high harmonics but also constitute the first experiments on extending the concept of the PM to relativistic intensities by studying the reflected fundamental of the laser beam in this regime.

Appendix B

XUV Spectrometers

Four different XUV-spectrometers have been used for the measurements presented in this thesis. Each one of these instruments has unique properties making it more or less suitable for certain measurements. The Acton VM-502 is a compact and easy to align normal incidence spectrometer wit a large numerical aperture but limited capabilities at short wavelength, the McPherson 248/310G is more difficult to align but has the highest spectral resolution and can be adjusted between 12 nm and 300 nm without breaking the vacuum, The RAL flat-field spectrometer is a very versatile tool owing to its large-area grating and versatile camera mounting system which is ideal for measurements of the harmonic divergence (see Chapter 5) and finally the transmission spectrometer is very easy to align and ideal when a non-imaging spectrometer is needed like for the temporal coherence measurements in Chapter 4.

This appendix will give an overview over the properties of each one of the four spectrometers and also give some technical details to assist future users of these instruments.

B.1 The Acton VM-502

The Acton Research VM-502 is a compact 20 cm focal-length normal-incidence vacuum spectrometer designed for measurements ranging from the UV down to the XUV spectral range. Figure B.1 shows some photographs of the instrument with labels pointing out the most important components. Owing to its normal incidence geometry it has a large numerical aperture (f/4.5) and is relatively easy to align. Furthermore the large aperture allows the use of a short focal-length collection mirror to maximize the signal in the spectrometer. For this reason the instrument was used for the first harmonic measurements on both the ATLAS as well as the LWS10 laser system. The disadvantage of the normal incidence geometry is the low reflectivity of the grating for wavelength below 50 nm effectively limiting the detectable harmonic range to orders below 16. For shorter wavelength

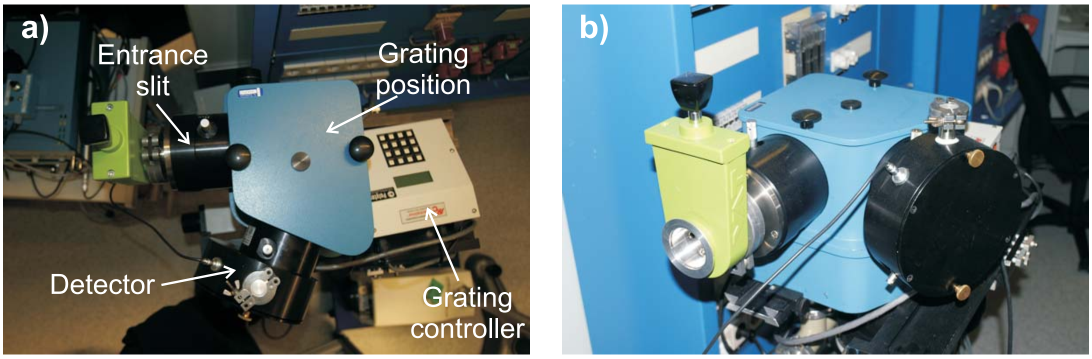

Figure B.1: Top- (a) and side-view (b) of the Acton Research VM-502 normal-incidence XUV spectrometer. The most important components are labeled in (a). Note that the spectrometer is shown with exit-slit and photomultiplier as a detector and not with the MCP+CCD array used for the measurements in this thesis.

a grazing-incidence instrument has to be used.

Figure B.2 shows a schematic drawing of the instruments setup. The concave iridium-coated 1200 L/mm grating images the entrance slit onto the position of the exit-slit on the Rowland circle [99] in a Seya-Namioka geometry [174] (the thin black lines mark the path from the entrance to the exit slit). The wavelength on the exit-slit can be adjusted by rotating the grating inside the spectrometer using an external wavelength-calibrated controller. Other wavelengths are imaged to different positions on the Rowland circle.

Two different detector setups are available for the Acton spectrometer. The conventional exit-slit assembly for scanning measurements shown in figure B.1 or a home-made large area Multi-Channel-Plate (MCP) detector for single shot detection of a whole spectral range. While the scanning setup allows measurements with the highest possible spectral resolution over a large wavelength range it is not very useful for the characterization of surface harmonics because many shots are necessary to acquire a single spectrum. For this reason a special large area detector was designed for the Acton spectrometer. It consists of a large area (25 mm diameter) Cesium-Iodine (CsI) coated MCP the output of which is accelerated onto a fluorescent phosphor screen. The screen is then imaged using a fiber taper and a one mega-pixel 16-bit CCD-camera (Photometrics CH350). With this setup spectra spanning a range of 50 nm can be acquired in a single shot. This comes at the expense of the spectral resolution though since, while the MCP is flat, the different wavelength are imaged by the grating onto a circle with a diameter of 20 cm. Furthermore rotating the grating shifts the Rowland circle which in turn also shifts the focal positions of the different wavelengths. Nevertheless the spectral resolution of the setup is still sufficient to obtain high quality spectra resolving even sub-structures of the individual harmonics like the ones observed with the LWS10 laser system (see chapter 6).

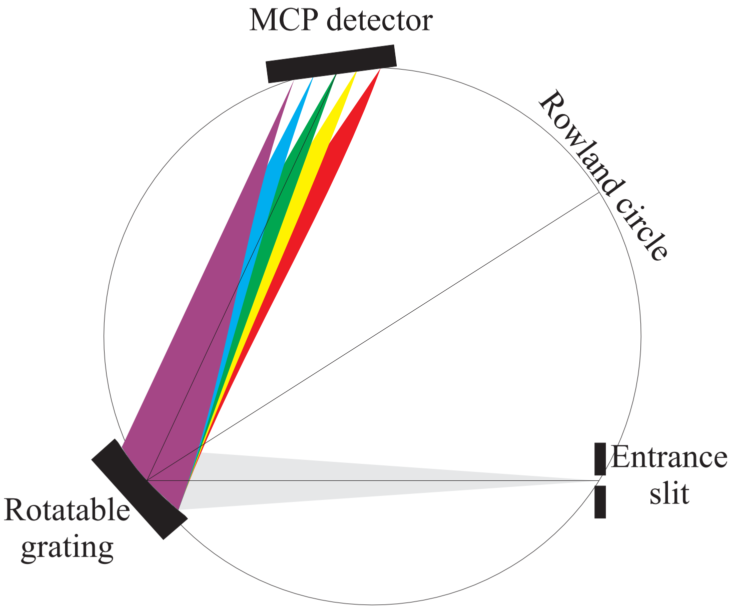

Figure B.2: Schematic drawing of the Acton Research VM-502 spectrometer. The entrance slit is imaged onto the Rowland circle by the iridium-coated grating. The spectrum is detected using MCP+CCD camera array mounted in a fixed position. The wavelength on the detector can be adjusted by rotating the grating.

It is important to note that the CsI-coated MCP requires good vacuum smaller than 10^{-5} mbar for safe operation. In practice this does not pose a large problem though since the spectrometer is equipped with its own pump and, at least in the solid harmonic experiments, no large gas-loads are present in the target chamber. In turn the MCP is more sensitive than an X-ray CCD in the spectral range between 50 nm and 120 nm and is solar blind, i.e. the quantum efficiency for IR-photons is extremely low reducing problems with signal from stray light and allowing, even with the ATLAS laser, measurements without an additional filter in front of the spectrometer.

B.2 The McPherson 248/100G

For measurements with higher spectral resolution and especially down to much shorter wavelength than those achievable with the Acton spectrometer a McPherson 248/310G 1 m focal length grazing-incidence spectrometer is available at the MPQ. Figure B.3 shows some photographs of the instrument. The spectrometer is designed to cover the wavelength range from 1 nm to 300 nm using a set of gold-coated spherical gratings with different line spacing. The instrument is set up for an angle of incidence of 87° to allow for maximum reflectivity of the grating at short wavelengths (see figure B.4 for a schematic

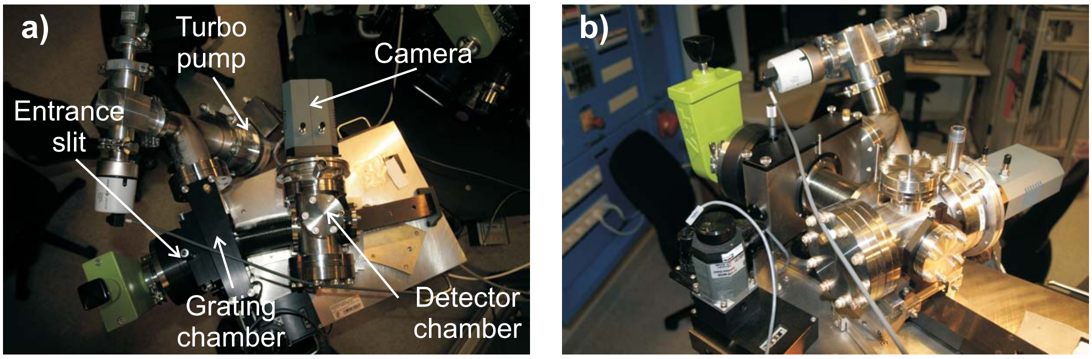

Figure B.3: Top- (a) and side-view (b) of the McPherson 248/100G grazing-incidence XUV spectrometer. The most important components are labeled in (a).

drawing), the drawback of this being a small aperture (f/45) which makes the instrument difficult to align and limits the amount of light that can be collected. This is an issue especially when the XUV radiation is emitted into a rather large cone.

Just like the Acton spectrometer the McPherson can be operated with two different detector setups, an exit-slit with a photomultiplier or a CsI-coated MCP-detector with phosphor screen and CCD-camera (Model DH420, Andor) mounted tangentially to the Rowland circle. Unlike in the other instrument, however, the detected wavelength is adjusted by scanning the detector along the focal plain of the grating rather than by rotating the grating itself. Together with the relatively long focal length of the grating this helps to keep the large-area planar MCP very close to the focus of the grating for all wavelength maximizing the resolution of the spectrometer. Table B.1 gives an overview over the wavelength ranges accessible with the different available gratings and the corresponding spectral resolution. Note that the low wavelength limit on the spectral range is not determined by the reflectivity of the grating but rather by the fact that the chamber with the MCP is relatively big and cannot be brought closer to the grating. For this reason gratings with larger dispersion can measure down to lower wavelength.

The position of the detector can be adjusted either using a LabView^{TM} program or

Grating (L/mm)	Range (nm)	Resolution (nm)	Dispersion (nm/mm)
133.6	13–300	0.16	0.4–1.6
600	3–75	0.036	0.08–0.34
2400	1–18	0.009	0.03–0.15

Table B.1: Overview over the properties of the gratings available for the McPherson 248/100G spectrometer at MPQ. The wavelength range is given for the case that the MCP detector is used.

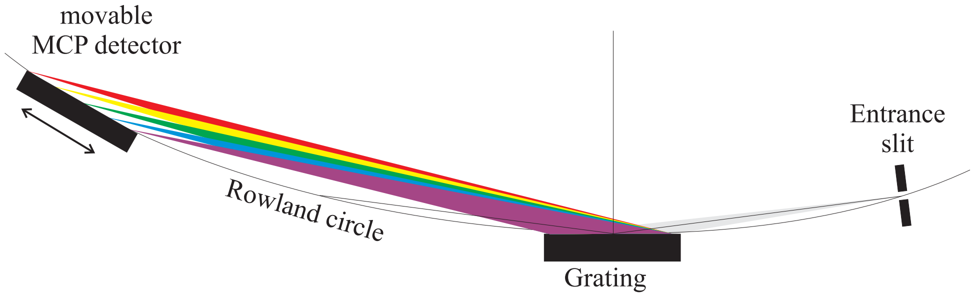

Figure B.4: Schematic drawing of the McPherson 248/310G spectrometer. The entrance slit is imaged onto a MCP detector mounted tangentially to the Rowland circle. The detector can be moved along the circle to position it at the desired wavelength range. The angle of incidence shown in this schematic is slightly smaller than in the real instrument (83° instead of 87°).

manually using the included motor controller directly. The detector position can be read from a dial on the spectrometer itself. It is given in terms of the cord length, i.e. the distance between the center of the grating and the center of the detector, in inches. The cord length L is related to the diffraction angle and thus the wavelength of the radiation via

$$L = d_{\mathrm{R}} \cos \Theta_{\mathrm{Out}}, \tag{B.1}$$

where d_{R} is the diameter of the Rowland circle and Θ_{Out} denotes the diffraction angle under which radiation with the corresponding wavelength is emitted. Θ_{Out} can be calculated easily from the grating equation

$$\Theta_{\mathrm{Out}} = -\arcsin(G\lambda - \sin \Theta_{\mathrm{In}}), \tag{B.2}$$

in which G is the groove density of the grating and Θ_{In} is the angle of incidence. Since $\Theta_{\mathrm{In}} = 87°$ and $d_{\mathrm{R}} = 1\ m$ are fixed and the groove densities of the various gratings are known one can directly calculate the corresponding wavelength from the cord length by inserting equation B.2 into equation B.1.

Beyond this it is also possible to calculate the wavelength range detectable in a single shot with the MCP detector. The distance D between the focal positions of different wavelengths corresponding to the diffraction angles $\Theta_{\mathrm{Out,1}}$ and $\Theta_{\mathrm{Out,2}}$ can be derived from geometrical considerations and is given by

$$D = d_{\mathrm{R}} \sqrt{\cos^2 \Theta_{\mathrm{Out,1}} + \cos^2 \Theta_{\mathrm{Out,2}} - \cos \Theta_{\mathrm{Out,1}}\ \cos \Theta_{\mathrm{Out,2}}\ \cos(\Theta_{\mathrm{Out,2}} - \Theta_{\mathrm{Out,1}})}. \tag{B.3}$$

Setting D to ±25 mm (half the width of the MCP) one can now calculate the highest and

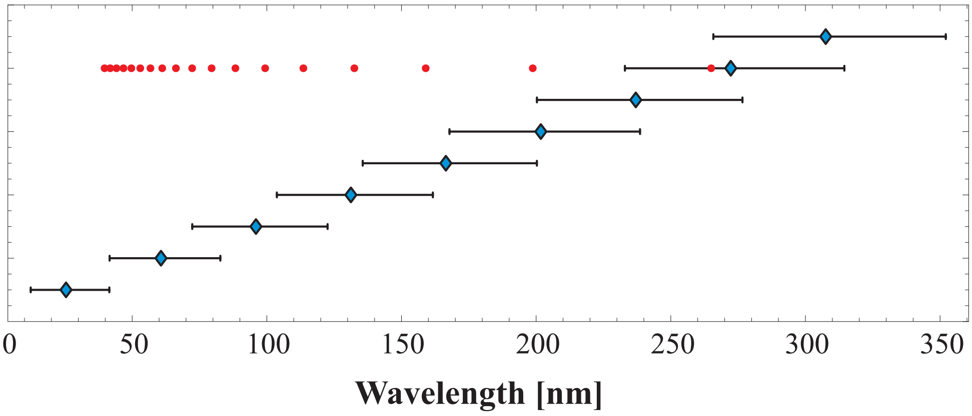

Figure B.5: Wavelength ranges detectable with a single shot using the McPherson spectrometer and the 133.6 L/mm grating for various central wavelengths (blue squares). The red dots mark the positions of harmonics 3 to 20 for reference.

lowest wavelength detectable for a certain central wavelength. Figure B.5 illustrates this by showing the detectable wavelength ranges as error bars for different central wavelength (blue squares) for the 133.6 lines mm^{-1} grating. The red dots show the positions of harmonics 3 through 20 as a reference.

The combination of the large spectral range detectable in a single shot, the capability to measure down to very short wavelength and the versatility as a result of the easily exchangeable gratings makes this spectrometer a very versatile tool for single shot measurements in the XUV range and the spectrometer of choice for most measurements conducted at the MPQ (presented in Chapters 4 and 6).

B.3 The RAL Flat Field Spectrometer

For the measurements conducted at the Rutherford-Appleton-Laboratory a grazing incidence flat-field spectrometer designed and constructed at RAL was used [175]. The instrument is based on a large area (30 mm×50 mm) Hitachi Part No. 001-0437 varied-line-space grating and a 256×1024 pixel Andor x-ray CCD camera in a housing specially designed at RAL. Photographs of the spectrometer are shown in figure B.6. Owing to the large grating size the spectrometer can be used to record multiple spectra simultaneously when suitable collection optics and/or slits are used (see for example figure 5.8 and [175]). At the same time the instrument is very compact.

The key to the compactness of the spectrometer is the concave varied-line-space grating which images the individual spectral components onto a flat surface rather than a Rowland circle [176–178]. The advantage of this is twofold: first the focal plane matches the

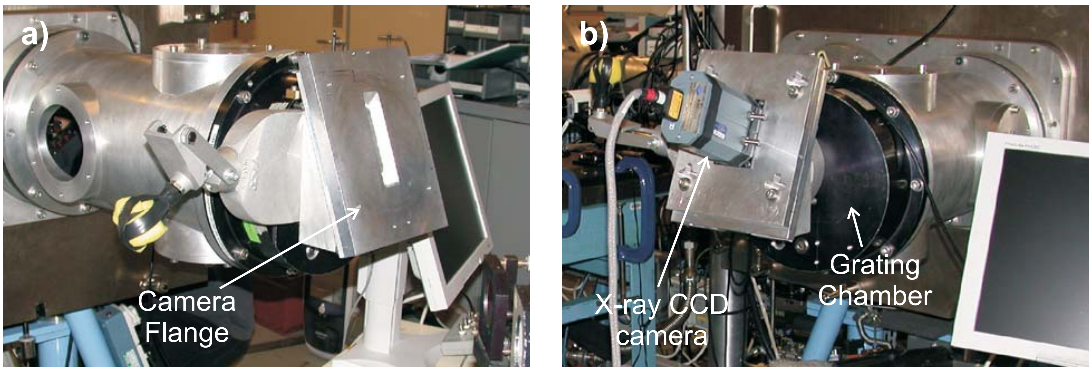

Figure B.6: Side-views of the RAL flat-field XUV spectrometer with labels pointing to the most important components are labeled in (a).

naturally flat surface of the CCD camera so that all colors are directly in focus on the detector and second the focal plane is oriented perpendicular to the direction of the 0^{th} order reflection off the grating. Figure B.7 shows a schematic drawing of this setup. The result of this is a setup much smaller than the one of the McPherson spectrometer with the conventional concave grating (figure B.4) while using the same angle of incidence onto the grating albeit with a smaller spectral resolution of approximately 0.1 nm.

The camera mounting flange is designed such that the camera can be moved along the focal plane of the grating such that different wavelength ranges can be observed. In addition this mounting system in combination with the large-area grating allows mounting the camera with its long side perpendicular to the dispersion direction for additional angular resolution at the expense of a smaller detectable wavelength range. The configuration with increased angular resolution was used for the work presented in this thesis to determine the divergence of the individual ROM harmonics (section 5.3.2 and especially figure 5.9). The trade-off between the observed spectral and angular range could be overcome in the future by using a quadratic, i.e. 1024×1024 pixel CCD camera, though.

In principle the spectrometer could also be equipped with an MCP detector for an even larger field of view (MCPs with diameters of 50 mm or more are readily available). However, while an MCP has the advantage of being solar blind, i.e. being insensitive to IR-radiation, it needs very good vacuum better than 10^{-5} mbar for safe operation requiring either a separate pump for differential pumping of the spectrometer or very long pumping times between chamber letups making this impractical for experiments that require frequent exchange of targets.

Another important feature of the RAL flat-field spectrometer is that it has been absolutely calibrated. For this purpose the reflectivity of the grating and various collection mirrors have been measured at the Daresbury synchrotron facility [175]. Together with the sensitivity data for the CCD provided by the manufacturer and information on the

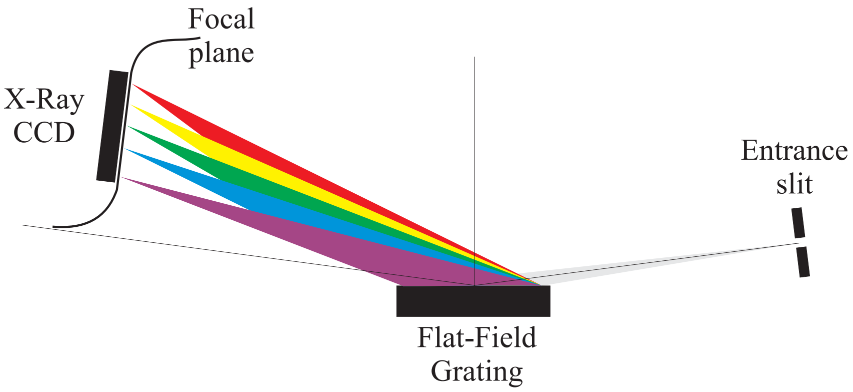

Figure B.7: Schematic drawing of the flat-field spectrometer used in the experiments at RAL (Chapter 5). Unlike the McPherson spectrometer the varied-line-space flat-field Hitachi grating images the entrance slit of the spectrometer onto a plane surface. Thus all wavelengths are in focus on the plane surface of the x-ray CCD used for recording the spectra. The angle of incidence shown in this schematic is slightly smaller than in the real instrument (83° instead of 87°).

throughput of the filters used to block residual IR-radiation the absolute efficiency of the spectrometer can be deduced. The transmission curve obtained using these values in the range between 15 nm and 40 nm is shown in figure 5.7 and in is discussed in more detail in the context of the experimental results presented in chapter 5.3.1 of this thesis.

B.4 The Transmission Spectrometer

The transmission spectrometer used for the experiments discussed in chapter 4 is different from the other instruments presented here in several respects. Especially, owing to the transmission geometry, it is the only spectrometer that does not image the entrance aperture in the dispersion direction. While this slightly reduces the spectral resolution of the device it offers the unique possibility to analyze, for example, the beam profile of the individual harmonics in two dimensions.

A schematic drawing of the spectrometer is shown in figure B.8. The detected wavelength can be adjusted over a large range by rotating the detector around the position of the grating. To vary the resolution (within certain limits) pipes of different length can be placed between the grating and the detector. For the measurements presented in this thesis a free-standing 2000 lines mm^{-1} grating and a CsI-coated MCP+CCD array (the same detector as the one used on the Acton VM-502) where used to record the XUV spectra. The distance from the grating to the detector was set to be 60 cm. It is important to point out though, that the spectrometer is not limited to this configuration. In principle

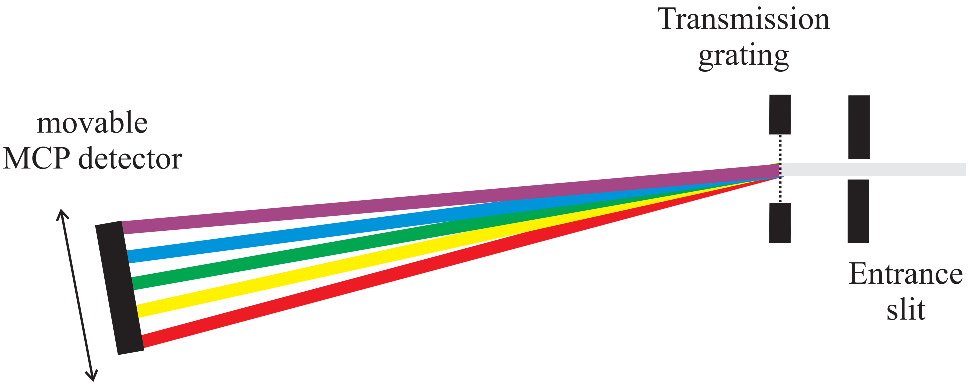

Figure B.8: Schematic drawing of the non-imaging transmission spectrometer designed and constructed by the University of Düsseldorf. In the measurements presented in Chapter 4 this thesis the spectrometer was equipped with a 2000 lines mm^{-1} grating and the MCP+CCD detector of the Acton VM-502 spectrometer (see Appendix B.1).

any transmission grating and for example an x-ray CCD camera could be used.

Owing to the special properties of the spectrometer it can be used as more than just a simple device for measuring XUV spectra. By placing a suitable aperture in front of the grating it is, for example, possible to convert the spectrometer into an XUV-interferometer [142]. The principle of this setup is shown in figure B.9. Instead of an entrance slit a pair of pinholes is placed in front of the transmission grating. Owing to the fact that the spectrometer does not image the entrance aperture the beams diffracting from the two pinholes interfere on the detector if the sizes of the pinholes and their separation are chosen properly. By rotating the orientation of the pinholes with respect to the grating lines a time delay can be introduced between the two beams in the first diffraction order. By evaluating the fringe visibility on the detector as a function of the delay one can now for example measure the temporal coherence of the individual harmonics (see Chapter 4). The time delay between the two beams of the qth harmonic Δt_q can be calculated from the angle between the axis connecting the pinholes and the grating lines α using the following relation

$$\Delta t_q = \frac{\Delta d}{c_0} = \frac{S \sin\alpha}{c_0} G \lambda_q, \tag{B.4}$$

where Δd is the path-length difference, S denotes the distance between the two pinholes, G is the groove density of the grating and λ_q is the wavelength of the qth harmonic. For the pinhole separation of 100 μm used in the experiments in Chapter 4 this means that the delay can be adjusted between zero and a maximum value of $\Delta t_{q,\mathrm{max}} = 120\lambda_q/c_0$. A typical interferogram for zero delay is shown in the inlay of figure B.9 (a).

The pinholes are produced at the University of Düsseldorf via laser machining of a

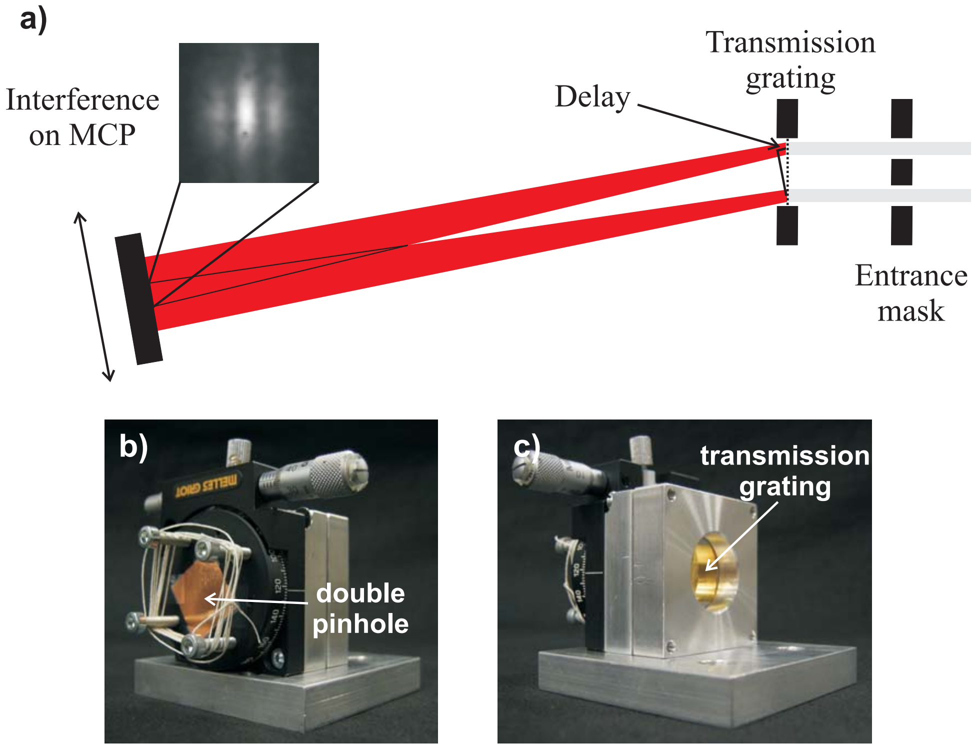

Figure B.9: (a) schematic of the spectrally resolved interferometer setup using the transmission spectrometer. The beams from two pinhole apertures interfere on the MCP detector in the first diffraction order. The delay between the two beams can be adjusted by rotating the two pinholes with respect to the orientation of the grating lines. Alignment of the holes parallel to the grating lines results in zero delay while an orientation perpendicular results in maximum delay. The inlay in (a) shows a typical interferogram obtained for the 14^{th} harmonic and zero delay. (b) and (c) show images of the pinhole and grating array. The double pinhole is mounted on a rotation stage for delay variation. Photographs courtesy of D. Hemmers from the University of Düsseldorf (see also [179]).

copper foil with a kHz laser system. The diameter of the individual pinholes is 60 μm. The copper foil is mounted on a rotation stage that can be accurately adjusted from outside the vacuum chamber using a PTFE-cord connected to a manual feedthrough (see photograph in figure B.9 (b)). The whole rotation mechanism is integrated into the grating assembly of the spectrometer to ensure accurate positioning of the pinholes.

Bibliography

[1] A. L. Schawlow and C. H. Townes. *Infrared and optical masers.* Phys. Rev., **112**(6), 1940–1949 (1958).

[2] S. Sartania, Z. Cheng, M. Lenzner, G. Tempea, C. Spielmann, F. Krausz and K. Ferencz. *Generation of 0.1 TW 5 fs optical pulses at a 1 kHz repetition rate.* Opt. Lett., **22**(20), 1562–1564 (1997).

[3] M. Nisoli, S. Stagira, S. De Silvestri, O. Svelto, S. Sartania, Z. Cheng, M. Lenzner, C. Spielmann and F. Krausz. *A novel high energy pulse compression system: generation of multigigawatt sub-5-fs pulses.* Appl. Phys. B, **65**(2), 189–196 (1997).

[4] A. L. Cavalieri, E. Goulielmakis, B. Horvath, W. Helml, M. Schultze, M. Fieß, V. Pervak, L. Veisz, V. S. Yakovlev, M. Uiberacker, A. Apolonski, F. Krausz, and R. Kienberger. *Intense 1.5-cycle near infrared laser waveforms and their use for the generation of ultra-broadband soft x-ray harmonic continua.* New J. Phys., **9**, 242 (2007).

[5] A. H. Zerwail. *Femtochemistry: Atomic-scale dynamics of the chemical bond.* J. Phys. Chem. A, **104**(24), 5660–5694 (2000).

[6] M. Drescher, M. Hentschel, R. Kienberger, G. Tempea, C. Spielmann, G. A. Reider, P. Corkum and F. Krausz. *X-ray pulses approaching the attosecond frontier.* Science, **291**, 1923–1927 (2001).

[7] P. M. Paul, E. S. Toma, P. Breger, G. Mullot, F. Auge, P. Balcou, H. G. Muller and P. Agostini. *Observation of a train of attosecond pulses from high harmonic generation.* Science, **292**, 1689–1692 (2001).

[8] M. Hentschel, R. Kienberger, C. Spielmann, G. A. Reider, N. Milosevic, T. Brabec, P. Corkum, U. Heinzmann, M. Drescher and F. Krausz. *Attosecond metrology.* Nature, **414**, 509–513 (2001).

[9] P. D. Corkum. *Plasma perspective on strong-field multiphoton ionization.* Phys. Rev. Lett., **71**(13), 1994–1997 (1993).

[10] E. Goulielmakis, M. Uiberacker, R. Kienberger, A. Baltuska, V. Yakovlev, A. Scrinzi, T. Westerwalbesloh, U. Kleineberg, U. Heinzmann, M. Drescher and F. Krausz. *Direct measurement of light waves.* Science, **305**, 1267–1269 (2004).

[11] G. Sansone, E. Benedetti, F. Calegari, C. Vozzi, L. Avaldi, R. Flammini, L. Poletto, P. Villoresi, C. Altucci, R. Velotta, S. Stagira, S. De Silvestri and M. Nisoli. *Isolated single-cycle attosecond pulses.* Science, **314**, 443–446 (2006).

[12] E. Goulielmakis, M. Schultze, M. Hofstetter, V. S. Yakovlev, J. Gagnon, M. Uiberacker, A. L. Aquila, E. M. Gullikson, D. T. Attwood, R. Kienberger, F. Krausz and U. Kleineberg. *Single-Cycle Nonlinear Optics.* Science, **320**, 1614–1617 (2008).

[13] M. Uiberacker, T. Uphues, M. Schultze, A. J. Verhoef, V. S. Yakovlev, M. F. Kling, J. Rauschenberger, M. N. Kabachnik, H. Schröder, M. Lezius, K. L. Kompa, H.-G. Muller, M. J. J. Vrakking, S. Hendel, U. Kleineberg, U. Heinzmann, M. Drescher and F. Krausz. *Attosecond real-time observation of electron tunnelling in atoms.* Nature, **446**, 627–632 (2007).

[14] A. L. Cavalieri, N. Müller, T. Uphues, V. S. Yakovlev, A. Baltuska, B. Horvath, B. Schmidt, L. Blümel, R. Holzwarth, S. Hendel, M. Drescher, U. Kleineberg, P. M. Eschenique, R. Kienberger, F. Krausz and U. Heinzmann. *Attosecond spectroscopy in condensed matter.* Nature, **449**, 1029–1032 (2007).

[15] A. Rundquist, C. G. Durfee III, Z. Chang, C. Herne, S. Backus, M. M. Murnane and H. C. Kapteyn. *Phase-matched generation of coherent soft x-rays.* Science, **280**, 1412–1415 (1998).

[16] Y. Tamaki, J. Itatani, Y. Nagata, M. Obara and K. Midorikawa. *Highly efficient, phase-matched high-harmonic generation by a self-guided laser beam.* Phys. Rev. Lett., **82**(7), 1422–1425 (1999).

[17] E. Constant, D. Garzella, P. Breger, E. Mével, C. Dorrer, C. Le Blanc, F. Salin and P. Agostini. *Optimizing high harmonic generation in absorbing gases: Model and experiment.* Phys. Rev. Lett., **82**(8), 1668–1671 (1999).

[18] L. Roos, E. Constant, E. Mével, P. Balcou, D. Descamps, M. B. Gaarde, A. Valette, R. Haroutunian and A. L'Huillier. *Controlling phase matching of high-order harmonic generation by manipulating the fundamental field.* Phys. Rev. A, **60**(6), 5010–5018 (1999).

[19] E. Foumouo, P. Antoine, H. Bachau and B. Piraux. *Attosecond timescale analysis of the dynamics of two-photon double ionization of helium.* New J. Phys., **10**, 025017 (2008).

[20] T. Morishita, S. Watanabe and C. D. Lin. *Attosecond light pulses for probing two-electron dynamics of helium in the time domain.* Phys. Rev. Lett., **98**(8), 083003 (2007).

[21] J. Feist, S. Nagele, R. Pazourek, E. Persson, B. I. Schneider, L. A. Collins and J. Burgdörfer. *Nonsequential two-photon double ionization of helium.* Phys. Rev. A, **77**(4), 043420 (2008).

[22] S. X. Hu and L. A. Collins. *Attosecond pump probe: Exploring ultrafast electron motion inside an atom.* Phys. Rev. Lett., **96**(7), 073004 (2006).

[23] U. Bovensiepen. *Coherent and incoherent excitations of the Gd(0001) surface on ultrafast timescales.* J. Phys.: Condens. Matter, **19**(8), 1–55 (2007).

[24] M. Bauer. *Femtosecond ultraviolet photoelectron spectroscopy of ultra-fast surface processes.* J. Phys. D: Appl. Phys., **38**(16), R253–R267 (2005).

[25] H. N. Chapman, S. P. Hau-Riege, M. J. Bogan, S. Bajt, A. Barty, S. Boutet, S. Marchesini, M. Frank, B. W. Woods, W. H. Benner, R. A. London, U. Rohner, A. Szoke, E. Spiller, T. Möller, C. Bostedt, D. A. Shapiro, M. Kuhlmann, P. Treusch, E. Plönjes, F. Burmeister, M. Bergh, G. Caleman, C. Huldt, M. M. Seibert and J. Hajdu. *Femtosecond time-delay x-ray holography.* Nature, **448**, 676–679 (2007).

[26] N. Matlis, S. Reed, S. Bulanov, V. Chvykov, G. Kalintchenko, T. Matsuoka, P. Rousseau, V. Yanovsky, A. Maksimchuk, S. Kalmykov, G. Shvets and M. Downer. *Snapshots of laser wakefields.* Nature physics, **2**, 749–753 (2006).

[27] J. Meyer-ter Vehn, J. Honrubia, M. Geissler, S. Karsch, F. Krausz, G. Tsakiris and K. Witte. *On electron transport in fast ignition research and the use of few-cycle PW-range laser pulses.* Plasma Phys. Control. Fusion, **47**, B807–B813 (2005).

[28] J. J. Honrubia and J. Meyer-ter Vehn. *Three-dimensional fast electron transport for ignition-scale inertial fusion capsules.* Nucl. Fusion, **46**, L25–L28 (2006).

[29] T. Brabec and F. Krausz. *Intense few-cycle laser fields: Frontiers of nonlinear optics.* Rev. Mod. Phys., **72**(2), 545–591 (2000).

[30] T. Baeva, S. Gordienko and A. Pukhov. *Theory of high-order harmonic generation in relativistic laser interaction with overdense plasma.* Phys. Rev. E, **74**(4), 046404 (2006).

[31] W. Ackermann et al. *Operation of a free-electron laser from the extreme ultraviolet to the water window.* Nature Photonics, **1**(6), 336–342 (2007).

[32] S. Gordienko, A. Pukhov, O. Shorokhov and T. Baeva. *Coherent focusing of high harmonics: A new way towards the extreme intensities.* Phys. Rev. Lett., **94**(10), 103903 (2005).

[33] J. Schwinger. *On gauge invariance and vacuum polarization.* Phys. Rev., **82**(5), 664–679 (1951).

[34] F. Quéré, C. Thaury, P. Monot, S. Dobosz, P. Martin, J.-P. Geindre and P. Audebert. *Coherent wake emission of high-order harmonics from overdense plasmas.* Phys. Rev. Lett., **96**(12), 125004 (2006).

[35] F. Quéré, C. Thaury, J.-P. Geindre, G. Bonnaud, P. Monot and P. Martin. *Phase properties of laser high-order harmonics generated on plasma mirrors.* Phys. Rev. Lett., **100**(9), 095004 (2008).

[36] G. D. Tsakiris, K. Eidmann, J. Meyer-ter Vehn and F. Krausz. *Route to intense single attosecond pulses.* New J. Phys., **8**, 19 (2006).

[37] S. Gordienko, A. Pukhov, O. Shorokhov and T. Baeva. *Relativistic Doppler effect: Universal spectra and zeptosecond pulses.* Phys. Rev. Lett., **93**(11), 115002 (2004).

[38] S. Rykovanov, M. Geissler, J. Meyer-ter Vehn and G. D. Tsakiris. *Intense single attosecond pulses from surface harmonics using the polarization gating technique.* New J. Phys., **10**, 025025 (2008).

[39] T. W. Hänsch. *A proposed sub-femtosecond pulse synthesizer using separate phase-locked laser oscillators.* Opt. Comm., **80**(1), 71–75 (1990).

[40] G. Farkas and C. Toth. *Proposal for attosecond light pulse generation using laser induced multiple-harmonic conversion processes in rare gases.* Phys. Lett. A, **168**, 447–450 (1992).

[41] N. H. Burnett, H. A. Baldis, M. C. Richardson and G. D. Enright. *Harmonic generation in CO_2 laser target interaction.* Appl. Phys. Lett., **31**(3), 172 (1977).

[42] R. L. Carman, D. W. Forslund and J. M. Kindel. *Visible harmonic emission as a way of measuring profile steepening.* Phys. Rev. Lett., **46**(1), 29–32 (1981).

[43] R. L. Carman, C. K. Rhodes and R. F. Benjamin. *Observation of harmonics in the visible and ultraviolet created in CO_2-laser-produced plasmas.* Phys. Rev. A, **24**(5), 2649–2663 (1981).

[44] B. Bezzerides, R. D. Jones and D. W. Forslund. *Plasma mechanism for ultraviolet harmonic radiation due to intense CO_2 light.* Phys. Rev. Lett., **49**(3), 202–205 (1982).

[45] S. V. Bulanov, N. M. Naumova and F. Pegoraro. *Interaction of an ultrashort, relativistically strong laser pulse with an overdense plasma.* Phys. Plasmas, **1**(3), 745–757 (1994).

[46] P. Gibbon. *Harmonic generation by femtosecond laser-solid interaction: A coherent water-window light source?* Phys. Rev. Lett., **76**(1), 50–53 (1996).

[47] R. Lichters, J. Meyer-ter Vehn and A. Pukhov. *Short-pulse laser harmonics from oscillating plasma surfaces driven at relativistic intensity.* Phys. Plasmas, **3**(9), 3425–3437 (1996).

[48] R. Lichters and J. Meyer-ter Vehn. *High laser harmonics from plasma surfaces: Intensity and angular dependence, cutoffs and resonance layers at density ramps.* Multiphoton Porcesses 1996 IOP Conference Series, **154**, 221–230 (1997).

[49] S. Kohlweyer, G. D. Tsakiris, C.-G. Wahlström, C. Tillman and I. Mercer. *Harmonic generation from solid-vacuum interface irradiated at high laser intensities.* Opt. Comm., **117**(5-6), 431–438 (1995).

[50] D. von der Linde, T. Engers, G. Jenke, P. Agostini, G. Grillon, E. Nibbering, A. Mysyrowicz and A. Antonetti. *Generation of high-order harmonics from solid surfaces by intense femtosecond laser pulses.* Phys. Rev. A, **52**(1), R25–R27 (1995).

[51] M. Zepf, G. D. Tsakiris, G. Pretzler, I. Watts, D. M. Chambers, P. A. Norreys, U. Andiel, A. E. Dangor, K. Eidmann, C. Gahn, A. Machacek, J. S. Wark and K. Witte. *Role of the plasma scale length in the harmonic generation from solid targets.* Phys. Rev. E, **58**(5), R5253–R5256 (1998).

[52] A. Tarasevitch, A. Orisch, D. von der Linde, P. Balcou, G. Rey, J.-P. Chambaret, U. Teubner, D. Klöpfel and W. Theobald. *Generation of high-order spatially coherent harmonics from solid targets by femtosecond laser pulses.* Phys. Rev. A, **62**(2), 023816 (2000).

[53] U. Teubner, G. Pretzler, T. Schlegel, K. Eidmann, E. Förster and K. Witte. *Anomalies in high-order harmonic generation at relativistic intensities.* Phys. Rev. A, **67**(1), 013816 (2003).

[54] U. Teubner, K. Eidmann, U. Wagner, U. Andiel, F. Pisani, G. D. Tsakiris, K. Witte, J. Meyer-ter Vehn, T. Schlegel and E. Förster. *Harmonic emission from the rear side of thin overdense foils irradiated with intense ultrashort laser pulses.* Phys. Rev. Lett., **92**(18), 185001 (2004).

[55] K. Eidmann, T. Kawachi, A. Marcinkevicius, R. Bartlome, U. Teubner, G. D. Tssakiris and K. Witte. *Fundamental and harmonic emission from the rear side of a thin overdense foil irradiated by an intense ultrashort laser pulse.* Phys. Rev. E, **72**(3), 036413 (2005).

[56] P. A. Norreys, M. Zepf, S. Moustaizis, A. P. Fews, J. Zhang, P. Lee, M. Bakarezos, C. N. Danson, A. Dyson, P. Gibbon, P. Loukakos, D. Neely, F. N. Walsh, J. S. Wark and A. E. Dangor. *Efficient extreme-UV harmonics generated from picosecond laser pulse interactions with solid targets.* Phys. Rev. Lett., **76**(11), 1832–1835 (1996).

[57] C. Thaury, F. Quéré, J.-P. Geindre, A. Levy, T. Ceccotti, P. Monot, M. Bougeard, F. Reau, P. D'Oliveira, P. Audebert, R. Marjoribanks and P. Martin. *Plasma mirrors for ultrahigh-intensity optics.* Nat. Phys., **3**(6), 424–429 (2007).

[58] B. Dromey, S. Kar, C. Bellei, D. C. Carroll, R. J. Clarke, J. S. Green, S. Kneip, K. Markey, S. R. Nagel, P. T. Simpson, L. Willingale, P. McKenna, D. Neely, Z. Najmudin, K. Krushelnick, P. A. Norreys and M. Zepf. *Bright multi-keV harmonic generation from relativistically oscillating plasma surfaces.* Phys. Rev. Lett., **99**(8), 085001 (2007).

[59] A. Tarasevitch, K. Lobov, C. Wuensche and D. von der Linde. *Transition to the relativistic regime in high order harmonic generation.* Phys. Rev. Lett., **98**(10), 103902 (2007).

[60] C. Thaury, H. George, F. Quéré, R. Loch, J.-P. Geindre, P. Monot and P. Martin. *Coherent dynamics of plasma mirrors.* Nat. Phys., **4**(8), 631–634 (2008).

[61] B. Dromey, M. Zepf, A. Gopal, K. Lancaster, M. S. Wei, K. Krushelnick, M. Tatarakis, N. Vakakis, S. Moustaizis, R. Kodama, M. Tampo, C. Stoeckl, R. Clarke, H. Habara, D. Neely, S. Karsch and P. Norreys. *High harmonic generation in the relativistic limit.* Nat. Phys., **2**(7), 456–459 (2006).

[62] R. Hörlein, Y. Nomura, D. Herrmann, M. Stafe, I. Földes, S. Rykovanov, F. Tavella, A. Marcinkevicius, F. Krausz, L. Veisz and G. D. Tsakiris. *Few-cycle emission of high harmonics from solid density plasmas.* In preparation.

[63] Y. Nomura, R. Hörlein, P. Tzallas, B. Dromey, S. Rykovanov, Z. Major, J. Osterhoff, S. Karsch, L. Veisz, M. Zepf, D. Charalambidis, F. Krausz and G. D. Tsakiris. *Attosecond phase-locking of harmonics emitted from laser-produced plasmas.* Nat. Phys., **5**(2), 124–128 (2009).

[64] B. Dromey, D. Adams, R. Hörlein, Y. Nomura, S. G. Rykovanov, D. C. Caroll, P. S. Foster, S. Kar, K. Markey, P. McKenna, D. Neely, M. Geissler, G. D. Tsakiris and M. Zepf. *Diffraction limited performance and focusing of high harmonics from relativistic plasmas.* Nat. Phys., **5**(2), 146–152 (2009).

[65] D. An der Brügge and A. Pukhov. *Propagation of relativistic surface harmonics radiation in free space.* Phys. Plasmas, **14**(9), 093104 (2007).

[66] R. Hörlein, S. Rykovanov, B. Dromey, Y. Nomura, D. Adams, M. Geissler, M. Zepf, F. Krausz and G. D. Tsakiris. *Controlling the divergence of high harmonics from solid targets: A route toward coherent harmonic focusing.* Submitted.

[67] M. Behmke, R. Hörlein, Y. Nomura, J. Keyling, J. Osterhoff, Z. Major, S. Karsch, F. Krausz, D. Hemmers, G. D. Tsakiris and G. Pretzler. *Temporal characteristics of coherent wake field laser harmonics generated at solid surfaces.* In preparation.

[68] R. Hörlein, B. Dromey, D. Adams, Y. Nomura, S. Kar, K. Markey, P. S. Foster, D. Neely, F. Krausz, G. D. Tsakiris and M. Zepf. *High contrast plasma mirror: Spatial filtering and second harmonic generation at* $10^{19} W cm^{-2}$. New J. Phys., **10**, 083002 (2008).

[69] Y. Nomura. *Temporal characterization of harmonic radiation generated by intense laser-plasma interaction.* Ph.D. thesis, Ludwig-Maximilians-Universität München (2008).

[70] R. Hörlein, Y. Nomura, J. Osterhoff, Z. Major, S. Karsch, F. Krausz and G. D. Tsakiris. *High harmonics from solid surfaces as a source of ultra-bright XUV radiation for experiments.* Plasma Phys. Control. Fusion, **50**, 124002 (2008).

[71] P. Gibbon. *Short Pulse Laser Interaction with Matter.* Imperial College Press, London (2005).

[72] J. D. Jackson. *Classical Electrodynamics.* Wiley, 3rd edition (1998).

[73] W. L. Kruer. *The Physics of Laser Plasma Interactions.* Addison-Wesley, Redwood City, CA (1988).

[74] W. Zinth and H.-J. Körner. *Physik III: Optik, Quantenphänomene und Aufbau der Atome.* Oldenbourg, München, 3rd edition (1998).

[75] L. V. Keldysh. *Ionization in the field of a strong electromagnetic wave.* Sov. Phys. JETP, **20**, 1307 (1965).

[76] B. C. Stuart, M. D. Feit, S. Herman, A. M. Rubenchik, B. W. Shore and M. D. Perry. *Nanosecond to femtosecond laser-induced breakdown in dielectrics.* Phys. Rev. B, **53**(4), 1749–1761 (1996).

[77] B. Dromey, S. Kar, M. Zepf and P. Foster. *The plasma mirror - A subpicosecond optical switch for ultrahigh power lasers.* Rev. Sci. Inst., **75**, 645 (2004).

[78] G. Doumy, F. Quéré, O. Gobert, M. Perdrix, P. Martin, P. Audebert, J. C. Gauthier, J.-P. Geindre and T. Wittmann. *Complete characterization of a plasma mirror for the production of high-contrast ultraintense laser pulses.* Phys. Rev. E, **69**(2), 026402 (2004).

[79] Y. Nomura, L. Veisz, K. Schmid, T. Wittmann, J. Wild and F. Krausz. *Time-resolved reflectivity measurements on a plasma mirror with few-cycle laser pulses.* New J. Phys., **9**, 9 (2007).

[80] V. L. Ginzburg. *The Propagation of Electromagnetic Waves in Plasmas.* Pergamon, New York (1964).

[81] F. Brunel. *Not-so-resonant, resonant absorption.* Phys. Rev. Lett., **59**(1), 52 (1987).

[82] A. Einstein. *Zur Elektrodynamik bewegter Körper.* Annalen der Physik (Leipzig), **322**(10), 891 (1905).

[83] T. Baeva, S. Gordienko and A. Pukhov. *Relativistic plasma control for single attosecond x-ray burst generation.* Phys. Rev. E, **74**(6), 065401 (2006).

[84] T. Baeva, S. Gordienko and A. Pukhov. *Relativistic plasma control for single attosecond pulse generation: Theory, simulations, and structure of the pulse.* Laser and Particle Beams, **25**(3), 339–346 (2007).

[85] A. Pukhov. *Relativistic plasmas - X-rays in a flash.* Nat. Phys., **2**(7), 439–440 (2006).

[86] N. M. Naumova, J. A. Nees, I. V. Sokolov, B. Hou and G. A. Mourou. *Relativistic generation of isolated attosecond pulses in a* λ^3 *focal volume.* Phys. Rev. Lett., **92**(6), 063902 (2004).

[87] N. M. Naumova, C. P. Hauri, J. A. Nees, I. V. Sokolov, V. Lopez-Martens and G. A. Mourou. *Towards efficient generation of attosecond pulses from overdense plasma targets.* New J. Phys., **10**, 025022 (2008).

[88] M. Geissler, S. Rykovanov, J. Schreiber, J. Meyer-ter Vehn and G. D. Tsakiris. *3D simulations of surface harmonic generation with few-cycle laser pulses.* New J. Phys., **9**, 218 (2007).

[89] J. Meyer-ter Vehn, A. Pukhov and Z. Sheng. *Relativistic laser plasma interaction.* In D. Batani, C. J. Joachain, S. Martellucci and A. N. Chester (editors), *Atoms, Solids, and Plasmas in Super-Intense Laser Fields*, volume 93, p. 167. Kluwer, New York (2001).

[90] Z.-M. Sheng, K. Mima, J. Zhang and H. Sanuki. *Emission of electromagnetic pulses from laser wakefields through linear mode conversion.* Phys. Rev. Lett., **94**(9), 095003 (2005).

[91] B. Dromey, S. Rykovanov, D. Adams, R. Hörlein, Y. Nomura, P. S. Foster, S. Kar, K. Markey, D. Neely, M. Geissler, G. D. Tsakiris and M. Zepf. *Tuneable enhancement of high harmonic emission from laser–solid interactions.* Submitted.

[92] E. M. Gullikson. *X-ray interaction with matter, `http://www-cxro.lbl.gov/optical_constants`.* Currently available on the World Wide Web.

[93] B. L. Henke, E. M. Gullikson and J. C. Davis. *X-ray interactions: photoabsorption, scattering, transmission, and reflection at E=50-30000 eV, Z=1-92.* Atomic Data and Nuclear Data Tables, **54**(2), 181–342 (1993).

[94] S. G. Rykovanov. Private communications.

[95] A. J. Langley, E. J. Divall, C. H. Hooker, M. H. R. Hutchinson, A. J.-M. P. Lecot, D. Marshall, M. E. Payne and P. F. Taday. *Central Laser Facility annual report 2000 (RAL-TR-2000-036 p. 196).* Technical Report, Rutherford Appleton Laboratory (2000).

[96] D. Strickland and G. Mourou. *Compression of amplified chirped optical pulses.* Opt. Commun., **56**(3), 219–221 (1985).

[97] W. Koechner. *Solid-State Laser Engineering.* Springer, Berlin, New York, 6th edition (2006).

[98] A. E. Siegmann. *Lasers.* University Science Books, Sausalito, CA (1986).

[99] M. Born and E. Wolf. *Principles of optics.* Cambridge University Press, 7th edition (1999).

[100] C. P. J. Barty, T. Guo, C. Le Blanc, F. Raksi, C. Rose-Petruck, J. Squier, K. R. Wilson, V. V. Yakovlev and K. Yamakawa. *Generation of 18-fs, multiterawatt pulses by regenerative pulse shaping and chirped-pulse amplification.* Opt. Lett., **21**(9), 668–670 (1996).

[101] V. G. Dimitriev, G. G. Gurzadyan and D. N. Nikogosyan. *Handbook of Nonlinear Optical Crystals.* Springer, Berlin (1991).

[102] R. Boyd. *Nonlinear Optics.* Academic Press, London, 2nd edition (2003).

[103] *www.attoworld.de/research/PFS.html.*

[104] H. Baumhacker, A. Böswald, H. Haas, M. Fischer, W. Fölsner, G. Keller, U. Andiel, X. Dong, M. Dreher, K. Eidmann, E. Fill, M. Hegelich, M. Kaluza, S. Karsch, G. Pretzler, G. D. Tsakiris and K. J. Witte. *Advanced Titanium Sapphire Laser ATLAS MPQ-Report 272.* Technical Report, Max-Planck-Institut für Quantenoptik (2001).

[105] J. Fülöp, Z. Major, A. Henig, S. Kruber, R. Weingartner, T. Clausnitzer, E.-B. Kley, A. Tünnermann, V. Pervak, A. Apolonki, J. Osterhoff, R. Hörlein, F. Krausz and S. Karsch. *Short-pulse optical parametric chirped-pulse amplification for the generation of high-power few-cycle pulses.* New J. Phys., **9**, 438 (2007).

[106] S. Karsch, J. Osterhoff, A. Popp, T. P. Rowlands-Rees, Z. Major, M. Fuchs, B. Marx, R. Hörlein, K. Schmid, L. Veisz, S. Becker, U. Schramm, B. Hidding, G. Pretzler, D. Habs, F. Grüner, F. Krausz and S. M. Hooker. *GeV-scale electron acceleration in a gas-filled capillary discharge waveguide.* New J. Phys., **9**, 415 (2007).

[107] J. Osterhoff, A. Popp, Z. Major, B. Marx, T. P. Rowlands-Rees, M. Fuchs, M. Geissler, R. Hörlein, B. Hidding, S. Becker, E. A. Peralta, U. Schramm, F. Grüner, D. Habs, F. Krausz, S. M. Hooker and S. Karsch. *Generation of stable, low-divergence electron beams by laser wakefield acceleration in a steady-state-flow gas cell.* Phys. Rev. Lett., **101**(8), 085002 (2008).

[108] A. Popp, J. Osterhoff, Z. Major, R. Hörlein, M. Fuchs, R. Weingartner, J. Viera, M. Marti, R. A. Fonseca, L. O. Silva, S. M. Hooker, F. Krausz and S. Karsch. *Steering laser-wakefield-accelerated electrons by controlling the laser pulse front tilt.* In preparation.

[109] A. Henig, D. Kiefer, M. Geissler, S. G. Rykovanov, R. Ramis, R. Hörlein, J. Osterhoff, Z. Major, S. Karsch, F. Krausz, D. Habs and J. Schreiber. *Laser driven shock acceleration of ion beams from spherical mass-limited targets.* Phys. Rev. Lett. accepted.

[110] T. Fuji, A. Unterhuber, V. S. Yakovlev, G. Tempea, A. Stingl, F. Krausz and W. Drexler. *Generation of smooth, ultra-broadband spectra directly from a prism-less Ti:Sapphire laser.* Appl. Phys. B, **77**(1), 125–128 (2003).

[111] J. E. Murray and W. H. Lowdermilk. *Nd:YAG regenerative amplifier.* J. Appl. Phys., **51**, 3548 (1980).

[112] Spawr-Industries. *Segmented integrating mirrors* (1971). US-PAT. No. 4,195,913.

[113] H. Baumhacker, G. Pretzler, K. J. Witte, M. Hegelich, M. Kaluza, S. Karsch, A. Kudryashov, V. Samarkin and A. Roukossouev. *Correction of strong phase and amplitude modulations by two deformable mirrors in a multi-staged Ti:Sapphire laser.* Opt. Lett., **27**(17), 1570–1572 (2002).

[114] M. Pessot, P. Maine and G. Mourou. *1000 times expansion/compression of optical pulses for chirped pulse amplification.* Opt. Commun., **62**(6), 419–421 (1987).

[115] F. Verluise, V. Laude, Z. Cheng, C. Spielmann and P. Tournois. *Amplitude and phase control of ultrashort pulses by use of an acousto-optic programmable dispersive filter: Pulse compression and shaping.* Opt. Lett., **25**(8), 575–577 (2000).

[116] R. Trebino. *Frequency-resolved Optical Gating: The Measurement of Ultrashort Light Pulses.* Kluwer Academic Press, Boston, Dordrecht, London (2000).

[117] S. Karsch. Private communications.

[118] F. Tavella, K. Schmid, N. Ishii, A. Marcinkevicius, L. Veisz and F. Krausz. *High-dynamic range pulse-contrast measurements of a broadband optical parametric chirped-pulse amplifier.* Appl. Phys. B, **51**(6), 753–756 (2005).

[119] K. Schmid. *Characterization of ultrashort laser pulses by third order autocorrelation* (2004). Diploma Thesis.

[120] K. Schmid. Private communications.

[121] F. Tavella, A. Marcinkevicius and F. Krausz. *Investigation of the superfluorescence and signal amplification in an ultrabroadband multiterawatt optical parametric chirped pulse amplifier system.* New J. Phys., **8**, 219 (2006).

[122] F. Tavella, A. Marcinkevicius and F. Krausz. *90 mJ parametric chirped pulse amplification of 10 fs pulses.* Opt. Express, **14**(26), 12822–12827 (2006).

[123] F. Tavella, Y. Nomura, L. Veisz, V. Pervak, A. Marcinkevicius and F. Krausz. *Dispersion management for a sub-10-fs, 10 TW optical parametric chirped-pulse amplifier.* Opt. Lett., **32**(15), 2227–2229 (2007).

[124] F. Tavella. *Multiterawatt few-cycle pulse OPCPA for applications in high-field physics.* Ph.D. thesis, Ludwig-Maximilians-Universität München (2007).

[125] K. Schmid, L. Veisz, F. Tavella, S. Benavides, R. Tautz, D. Herrmann, A. Buck, B. Hidding, A. Marcinkevicius, U. Schramm, M. Geissler, J. Meyer-ter Vehn, D. Habs and F. Krausz. *Few-cycle-laser-driven electron acceleration.* Submitted.

[126] A. Dubietis, G. Jonusauskas and A. Piskarskas. *Powerful femtosecond pulse generation by chirped and stretched pulse parametric amplification in BBO crystal.* Opt. Commun., **88**(4), 437–440 (1992).

[127] www.femtolasers.com.

[128] S. Kane and J. Squier. *Grism-pair stretcher–compressor system for simultaneous second- and third-order dispersion compensation in chirped-pulse amplification.* J. Opt. Soc. Am. B, **14**(3), 661–665 (1997).

[129] C. Teisset, N. Ishii, T. Fuji, T. Metzger, S. Köhler, R. Holzwarth, A. Baltuška, A. Zheltikov and F. Krausz. *Soliton-based pump–seed synchronization for few-cycle OPCPA.* Opt. Express, **13**(17), 6550–6557 (2005).

[130] P. Russel. *Photonic crystal fibers.* Science, **299**, 358–362 (2003).

[131] N. Minkovski, G. I. Petrov, S. M. Saltiel, O. Albert and J. Etchepare. *Nonlinear polarization rotation and orthogonal polarization generation experienced in a single-beam configuration.* J. Opt. Soc. Am. B, **21**(9), 1659–1664 (2004).

[132] A. Jullien, O. Albert, F. Burgy, G. Hamoniaux, J.-P. Rousseau, J.-P. Chambaret, F. Augé-Rochereau, G. Chériaux, J. Etchepare, N. Minkovski and S. M. Saltiel. *10^{-10} temporal contrast for femtosecond ultraintense lasers by cross-polarized wave generation.* Opt. Lett., **30**(8), 920–922 (2005).

[133] A. Jullien, O. Albert, G. Chériaux, J. Etchepare, S. Kourtev, N. Minkovski and S. M. Saltiel. *A two crystal arrangement to fight efficiency saturation in cross-polarized wave generation.* Opt. Express, **14**(7), 2760–2769 (2006).

[134] R. Tautz. *Single-shot characterization of sub-10-fs laser pulses* (2008). Diploma Thesis.

[135] C. Iaconis, V. Wong and I. A. Walmsley. *Direct interferometric techniques for characterizing ultrashort optical pulses.* IEE J. Sel. Top. Quantum Electron., **4**(2), 285–294 (1998).

[136] C. Iaconis and I. A. Walmsley. *Spectral phase interferometry for direct electric-field reconstruction of ultrashort optical pulses.* Opt. Lett., **23**(10), 792–794 (1998).

[137] L. Veisz. Private communications.

[138] H. Daido. *Review of soft x-ray laser researches and developments.* Rep. Prog. Phys., **65**, 1513–1567 (2002).

[139] C. H. Skinner. *Review of soft x-ray lasers and their applications.* Phys. Fluids B, **3**, 2320–2330 (1991).

[140] M. Kando, Y. Fukuda, A. S. Pirozhkov, J. Ma, I. Daito, L.-M. Chen, T. Z. Esirkepov, K. Ogura, T. Homma, Y. Hayashi, H. Kotaki, A. Sagisaka, M. Mori, J. K. Koga, H. Daido, S. V. Bulanov, T. Kimura, Y. Kato and T. Tajima. *Demonstration of laser-fFrequency upshift by electron-density modulations in a plasma wakefield.* Phys. Rev. Lett., **99**(13), 135001 (2007).

[141] S. V. Bulanov, T. Esirkepov, and T. Tajima. *Light intensification towards the Schwinger limit.* Phys. Rev. Lett., **91**(8), 085001 (2003).

[142] D. Hemmers and G. Pretzler. *Multi-color XUV interferometry using high-order harmonics.* Submitted.

[143] P. Tzallas, D. Charalambidis, N. A. Papadogiannis, K. Witte and G. D. Tsakiris. *Direct observation of attosecond light bunching.* Nature, **426**, 267–270 (2003).

[144] Y. Nabekawa, T. Shimizu, T. Okino, K. Furusawa, H. Hasegawa, K. Yamanouchi and K. Midorikawa. *Conclusive evidence of an attosecond pulse train observed with the mode-resolved autocorrelation technique.* Phys. Rev. Lett., **96**(8), 083901 (2006).

[145] N. A. Papadogiannis, L. A. A. Nikolopoulos, D. Charalambidis, G. D. Tsakiris, P. Tzallas and K. Witte. *Two-photon ionization of He through a superposition of higher harmonics.* Phys. Rev. Lett., **90**(13), 133902 (2003).

[146] E. J. Takahashi, H. Hasegawa, Y. Nabekawa and K. Midorikawa. *High-throughput, high-damage-threshold broadband beam splitter for high-order harmonics in the extreme-ultraviolet region.* Opt. Lett., **29**, 507–509 (2004).

[147] D. R. Lidle (editor). *CRC Handbook of Chemistry and Physics.* CRC Press, 85th edition (2004).

[148] P. Tzallas, D. Charalambidis, N. A. Papadogiannis, K. Witte and G. D. Tsakiris. *Second-order autocorrelation measurements of attosecond XUV pulse trains.* J. Mod. Opt., **53**, 321–340 (2005).

[149] E. P. Benis, D. Charalambidis, T. N. Kitsopoulos, G. D. Tsakiris and P. Tzallas. *Two-photon double ionization of rare gases by a superposition of harmonics.* Phys. Rev. A, **74**(5), 051402 (2006).

[150] Y. Nabekawa, H. Hasegawa, E. J. Takahashi and K. Midorikawa. *Production of doubly charged helium ions by two-photon absorption of an intense sub-10-fs soft x-ray pulse at 42 eV photon energy.* Phys. Rev. Lett., **94**(4), 043001 (2005).

[151] R. Kienberger, M. Hentschel, M. Uiberacker, C. Spielmann, M. Kitzler, A. Scrinzi, M. Wieland, T. Westerwalbesloh, U. Kleineberg, U. Heinzmann, M. Drescher and F. Krausz. *Steering attosecond electron wave packets with light.* Science, **297**, 1144–1148 (2002).

[152] J. Gagnon, E. Goulielmakis and V. S. Yakovlev. *The accurate FROG characterization of attosecond pulses from streaking measurements.* Appl. Phys. B, **92**(1), 25–32 (2008).

[153] B. E. A. Saleh and M. C. Teich. *Fundamentals of Photonics.* Wiley, New York, 1st edition (1991).

[154] `www.extreme-light-infrastructure.eu`.

[155] `www.hyper-laser.org`.

[156] `www.clf.rl.ac.uk/Facilities/AstraWeb/AstraGeminiHome.htm`.

[157] C. Ziener, P. S. Foster, E. J. Divall, C. J. Hooker, M. H. R. Hutchinson, A. J. Langley and D. Neely. *Specular reflectivity of plasma mirrors as a function of intensity, pulse duration, and angle of incidence.* J. Appl. Phys., **93**, 768 (2003).

[158] T. Wittmann, J. P. Geindre, P. Audebert, R. S. Marjoribanks, J. P. Rousseau, F. Burgy, D. Douillet, T. Lefrou, K. Ta Phuok and J. P. Chambaret. *Towards*

ultrahigh-contrast ultraintense laser pulses—complete characterization of a double plasma-mirror pulse cleaner. Rev. Sci. Inst., **77**, 083109 (2006).

[159] K. Moncur. *Plasma spatial filter.* Applied Optics, **16**, 1449 (1977).

[160] H. Kapteyn, M. Murnane, A. Szoke and R. Falcone. *Prepulse energy suppression for high-energy ultrashort pulses using self-induced plasma shuttering.* Opt. Lett., **16**, 490 (1991).

[161] D. M. Gold. *Direct measurement of prepulse suppression by use of a plasma shutter.* Opt. Lett., **19**, 2006 (1994).

[162] O. Klimo, J. Psikal, J. Limpouch and V. T. Tikhonchuk. *Monoenergetic ion beams from ultrathin foils irradiated by ultrahigh-contrast circularly polarized laser pulses.* Phys. Rev. ST Accel. Beams, **11**(3), 031301 (2008).

[163] A. P. L. Robinson, M. Zepf, S. Kar, R. G. Evans and C. Bellei. *Radiation pressure acceleration of thin foils with circularly polarized laser pulses.* New J. Phys., **10**, 013021 (2008).

[164] A. Marcinkevicius, R. Tommasini, G. D. Tsakiris, K.-J. Witte, E. Gaizauskas and U. Teubner. *Frequency doubling of multi-terawatt femtosecond pulses.* Appl. Phys. B, **79**(5), 547–554 (2004).

[165] M. Zepf, M. Castro-Colin, D. Chambers, S. G. Preston, J. S. Wark, J. Zhang, C. N. Danson, D. Neely, P. A. Norreys, A. E. Dangor, A. Dyson and P. Lee. *Measurements of the hole boring velocity from Doppler shifted harmonic emission from solid targets.* Phys. Plasmas, **3**(9), 3242–3244 (1996).

[166] J. W. Robinson (editor). *CRC Handbook of Spectroscopy*, volume 1. CRC Press (1974).

[167] S. C. Wilks, W. L. Kruer, M. Tabak and A. B. Langdon. *Absorption of ultra-intense laser pulses.* Phys. Rev. Lett., **69**, 1383 (1992).

[168] P. Tzallas, E. Skantzakis, C. Kalpouzos, E. P. Benis, G. D. Tsakiris and D. Charalambidis. *Generation of intense continuum extreme-ultraviolet radiation by many-cycle laser fields.* Nature Phys., **3**, 846–850 (2007).

[169] I. N. Bronstein, K. A. Semendjajew, G. Musiol and H. Mühlig. *Taschenbuch der Mathematik.* Verlag Harri Deutsch, Frankfurt am Main, 4th edition (1999).

[170] T. Wittmann, B. Horvath, W. Helml, M. G. Schätzel, X. Gu, A. L. Cavalieri, G. G. Paulus and R. Kienberger. *Single-shot carrier-envelope phase measurement of intense few-cycle laser pulses.* In preparation.

[171] Y. M. Mikhailova, V. T. Platonenko and S. Rykovanov. *Generation of an attosecond x-ray pulse in a thin film irradiated by an ultrashort ultrarelativistic laser pulse.* JETP Letters, **81**, 703–707 (2006).

[172] M. Nantel, J. Itatani, A.-C. Tien, J. Faure, D. Kaplan, M. Bauvier, T. Buma, P. van Rompay, J. Nee, P. Pronko, D. Umstadter and G. Mourou. *Temporal contrast in Ti:Sapphire lasers, characterization and control.* Selected Topics in Quantum Electronics, IEEE Journal of, **4**(2), 449–458 (1998).

[173] J. Itatani, J. Faure, M. Nantel, G. Mourou and S. Watanabe. *Suppression of the amplified spontaneous emission in chirped-pulse-amplification lasers by clean high-energy seed-pulse injection.* Optics Communications, **148**, 70–74 (1998).

[174] T. Namioka. *Theory of the concave grating. III. Seya-Namioka monochromator.* J. Opt. Soc. Am., **49**(10), 951–962 (1959).

[175] D. Neely, D. Chambers, C. Danson, P. Norreys, S. Preston, F. Quinn, M. Roper, J. Wark and M. Zepf. *A multi-channel soft x-ray flat-field spectrometer.* AIP Conf. Proc., **426**(1), 479–484 (1998).

[176] T. Kita, T. Harada, N. Nakano and H. Kuroda. *Mechanically ruled aberration-corrected concave gratings for a flat-field grazing-incidence spectrograph.* Appl. Opt., **22**(4), 512–513 (1983).

[177] N. Nakano, H. Kuroda, T. Kita and T. Harada. *Development of a flat-field grazing-incidence XUV spectrometer and its application in picosecond XUV spectroscopy.* Appl. Opt., **23**(14), 2386–2392 (1984).

[178] T. Harada, K. Takahashi, H. Sakuma and A. Osyczka. *Optimum Design of a grazing-incidence flat-field spectrograph with a spherical varied-line-space grating.* Appl. Opt., **38**(13), 2743–2748 (1999).

[179] J. Keyling. *Erzeugung und Charakterisierung Hoher Harmonischer im weichen Röntgenbereich* (2008). Diploma Thesis.

Publications

2009

- Y. Nomura, **R. Hörlein**, P. Tzallas, B. Dromey, S. G. Rykovanov, Zs. Major, J. Osterhoff, S. Karsch, L. Veisz, M. Zepf, D. Charalambidis, F. Krausz and G. D. Tsakiris.
  Attosecond phase locking of harmonics emitted from laser-produced plasmas.
  Nature Phys., **5**(2), 124–128 (2009).

- B. Dromey, D. Adams, **R. Hörlein**, Y. Nomura, S. G. Rykovanov, D. C. Caroll, P. S. Foster, S. Kar, K. Markey, P. McKenna, D. Neely, M. Geissler, G. D. Tsakiris and M. Zepf.
  Diffraction limited performance and focusing of high harmonics from relativistic plasmas.
  Nature Phys., **5**(2), 146–152 (2009).

2008

- **R. Hörlein**, B. Dromey, D. Adams, Y. Nomura, S. Kar, K. Markey, P. S. Foster, D. Neely, F. Krausz, G. D. Tsakiris and M. Zepf.
  High contrast plasma mirror: spatial filtering and second harmonic generation at $10^{19}\,Wcm^{-2}$*.*
  New J. Phys., **10**, 083002 (2008).

- **R. Hörlein**, Y. Nomura, J. Osterhoff, Zs. Major, S. Karsch, F. Krausz and G. D. Tsakiris.
  High harmonics from solid surfaces as a source of ultra-bright XUV radiation for experiments.
  Plasma Phys. Control. Fusion, **50**, 124002 (2008).

- J. Osterhoff, A. Popp, Zs. Major, B. Marx, T. P. Rowlands-Rees, M. Fuchs, M. Geissler, **R. Hörlein**, B. Hidding, S. Becker, E. A. Peralta, U. Schramm, F. Grüner, D. Habs, F. Krausz, S. M. Hooker and S. Karsch.

Generation of stable, low-divergence electron beams by laser wakefield acceleration in a steady-state-flow gas cell.
Phys. Rev. Lett., **101**(8), 085002 (2008).

2007

- S. Karsch, J. Osterhoff, A. Popp, T. P. Rowlands-Rees, Zs. Major, M. Fuchs, B. Marx, **R. Hörlein**, K. Schmid, L. Veisz, S. Becker, U. Schramm, B. Hidding, G. Pretzler, D. Habs, F. Grüner, F. Krausz and S. M. Hooker.
  GeV-scale electron acceleration in a gas-filled capillary discharge waveguide.
  New J. Phys., **9**, 415 (2007).

- J. Fülöp, Zs. Major, A. Henig, S. Kruber, R. Weingartner, T. Clausnitzer, E.-B. Kley, A. Tünnermann, V. Pervak, A. Apolonki, J. Osterhoff, **R. Hörlein**, F. Krausz and S. Karsch.
  Short-pulse optical parametric chirped-pulse amplification for the generation of high-power few-cycle pulses.
  New J. Phys., **9**, 438 (2007).

Accepted Papers

- A. Henig, D. Kiefer, M. Geissler, S. G. Rykovanov, R. Ramis, **R. Hörlein**, J. Osterhoff, Zs. Major, S. Karsch, F. Krausz, D. Habs and J. Schreiber.
  Laser driven shock acceleration of ion beams from spherical mass-limited targets.
  Phys. Rev. Lett. *accepted.*

Submitted

- **R. Hörlein**, S. Rykovanov, B. Dromey, Y. Nomura, D. Adams, M. Geissler, M. Zepf, F. Krausz and G. D. Tsakiris.
  Controlling the divergence of high harmonics from solid targets: A route toward coherent harmonic focusing.
  Submitted to Eur. Phys. J. D.

- B. Dromey, S. Rykovanov, D. Adams, **R. Hörlein**, Y. Nomura, P. S. Foster, S. Kar, K. Markey, D. Neely, M. Geissler, G. D. Tsakiris and M. Zepf.
  Tuneable enhancement of high harmonic emission from laser-solid interactions.
  Submitted to Phys. Rev. Lett..

- M. Zepf, B. Dromey, M. Geissler, **R. Hörlein**, Y. Nomura, S. Rykovanov and G. D. Tsakiris.
  Ultrabright attosecond sources from relativistically oscillating mirrors.
  Submitted to J. Phys. B: At. Mol. Opt. Phys..

- Zs. Major, S. Trushin, I. Ahmad, M. Siebold, C. Wandt, S. Klingebiel, T.-J. Wang, J. A. Fülöp, A. Henig, S. Kruber, R. Weingartner, A. Popp, J. Osterhoff, **R. Hörlein**, J. Hein, V. Pervak, A. Apolonski, F. Krausz, S. Karsch.
  Basic concepts and current status of the Petawatt Field Synthesizer - a new approach to ultrahigh field generation.
  Submitted to Rev. Laser Eng..

In Preparation

- **R. Hörlein**, Y. Nomura, D. Herrmann, M. Stafe, I. Földes, S. Rykovanov, F. Tavella, A. Marcinkevicius, F. Krausz, L. Veisz and G. D. Tsakiris.
  Few-cycle emission of high harmonics from solid density plasmas.
  In preparation.

- M. Behmke, **R. Hörlein**, Y. Nomura, J. Keyling, J. Osterhoff, Zs. Major, S. Karsch, F. Krausz, D. Hemmers, G. D. Tsakiris and G. Pretzler.
  Temporal characteristics of coherent wake field laser harmonics generated at solid surfaces.
  In preparation.

- A. Popp, J. Osterhoff, Zs. Major, **R. Hörlein**, M. Fuchs, R. Weingartner, J. Viera, M. Marti, R. A. Fonseca, L. O. Silva, S. M. Hooker, F. Krausz and S. Karsch.
  Steering laser-wakefield-accelerated electrons by controlling the laser pulse front tilt.
  In preparation.

- M. Fuchs, R. Weingartner, A. Popp, Zs. Major, S. Becker, J. Osterhoff, **R. Hörlein**, G. D. Tsakiris, U. Schramm, B. Hidding, T. P. Rowlands-Rees, S. M. Hooker, D. Habs, F. Krausz, S. Karsch and F. Grüner.
  Table-top laser-driven ultrafast undulator radiation in the soft x-ray range.
  In preparation.

Acknowledgements

At this point I would like to take the opportunity to thank all the people that supported me during my four years as a Ph.D. student at MPQ and helped to successfully complete the experiments presented in this thesis.

First I would like to thank Prof. Ferenc Krausz for giving me the opportunity to pursue my Ph.D. in his group at MPQ and for creating a great working environment for experiments at the forefront of ultrafast science.

My special thanks goes to Dr. George Tsakiris for supervising this thesis and guiding the work in the right direction with his experience. He always found the right mix between directing the project toward its main goal and leaving a lot of freedom to pursue own ideas.

I am also indebted to Prof. Dietrich Habs for agreeing to be the second referee for my thesis, managing the funding of my Ph.D. position and especially for many interesting and visionary scientific discussions.

Of course I did not perform all the work in this thesis alone and, in fact, a lot of it would not have been possible without the support of many other people. First I would like to mention Yutaka Nomura with whom I performed all the experiments presented in this thesis and thank him for the excellent cooperation. Special thanks also goes to Sergey Rykovanov for the strong support of our experiments with his simulations and for many interesting discussions.

The work presented in this thesis has also greatly benefited from a whole series of national and international collaborations. Here I would like to thank Dr. Brendan Dromey, Prof. Matt Zepf and the whole team from Queens University Belfast for giving me the opportunity to participate in the experiments at RAL and for supporting the autocorrelation experiment in Garching, Dr. Pareskevas Tzallas and Prof. Dimitris Charalambidis from IESL in Crete for contributing their expertise on the volume autocorrelation technique especially also during the frustrating first attempts, Dr. Istvan Földes from Budapest and Dr. Michai Stafe from Sofia for the help during the LWS10 experiments and the colleagues from Düsseldorf, Michael Behmke, Jan Keyling, Dr. Dirk Hemmers and Prof. Georg Pretzler for the joint experiment on harmonic coherence.

My experiments would not have been possible without the excellent laser systems in Garching and at the Rutherford-Appleton-Laboratory and the people operating the systems. Therefore I would like to thank the ATLAS team, especially Stefan Karsch, Zsuzsanna Major and Jens Osterhoff for the excellent cooperation and the LWS10 team, Daniel Herrmann, Franz Tavella, Laszlo Veisz and Andrius Marcinkevicius for providing a unique laser system for high-intensity laser–solid interaction experiments. In addition I would like to acknowledge the great work of the ASTRA laser-crew at RAL.

I would also like to express my gratitude to the technical staff at MPQ, especially Manfred Fischer, Alois Böswald, Harald Haas and Hans-Peter Schönauer for their valuable support and thank the mechanical workshop for their work and specifically for their willingness to produce parts on very short time-scales when necessary.

At this point I would also like to thank all my fellow Ph.D. and Diploma students, especially Jens Osterhoff who has been a companion since the very beginning of my physics studies, Yutaka Nomura, Sergey Rykovanov, Antonia Popp, Andreas Henig, Daniel Kiefer, Daniel Jung, Matthias Fuchs, Raphael Weingärtner, my successor Patrick Heißler and all the others for their help, the fun time and all the discussions especially those not related to physics! Special thanks also goes to the various coffee machines in MPQ and especially Petra for always keeping me awake even late at night.

Last, but not least, I would like to thank Conny for her continuous support despite all the late nights I spent in the lab and the long absences for external experiments or conferences and my family for supporting my decision to study physics and their constant encouragement.